FH Aachen
University of Applied Sciences

Faculty of Aerospace Technology
Aircraft Engineering

FH AACHEN
UNIVERSITY OF APPLIED SCIENCES

Master's Thesis

Aerodynamic Investigation of Propeller-Wing Interaction for Simple Motions and Complex Modes

Shreyas Ashwin Sunder
Mat. No.: 3293672

Supervisor: Prof. Dr.-Ing. Carsten Braun

Reviewer: Nils Böhnisch M.Sc.

September 2024

I. Bibliographic Data

Author:	Shreyas Ashwin Sunder
Date of Birth:	03.02.1998 in Bhopal, India
Mat. No.:	3293672

Title:	Aerodynamic Investigation of Propeller-Wing Interaction for Simple Motions and Complex Modes
Document type:	Master’s Thesis
Study Course:	Aerospace Engineering
(ggf.) Kooperation:	FH Aachen Fachbereich 6, Luft- und Raumfahrttechnik Lehrgebiet Luftfahrzeugtechnik
Submission Date:	26.09.2024
Key Words:	Aerodynamic Interaction, Propeller-Wing Interaction, Unsteady Aerodynamics, Partitioned Coupling, Fluid-Motion Interaction (FMI), Pitching Motion, Plunging Motion, Theodorsen’s Theory, Goland Wing, Natural Frequencies, Bending Wing Modes, Torsion Wing Modes, Rigidly Attached Propeller, Flexibly Attached Propeller

II. Abstract

Abstract

Current research on propeller-wing interaction predominantly examines stationary wing scenarios, avoiding the complexities of wing and propeller motion. This thesis explores the aerodynamic interaction of a propeller-wing system in various motion scenarios using a novel simulation framework called Fluid-Motion Interaction (FMI). The FMI framework couples a mid-fidelity aero solver, DUST, with an FMI solver developed in MATLAB, validated against theoretical data for pitching and plunging wings and natural modes of the Goland wing, as well as existing research on propeller-wing interaction. Simulations of pitching and plunging wings with a rigidly attached propeller revealed a specific reduced frequency at which aerodynamic performance is maximised. Introducing relative motion between the propeller and wing showed that the aerodynamic response scales with the amplitude ratio of the propeller to the wing and varies linearly with the phase shift of the propeller. Finally, integrating a propeller on the Goland wing at various spanwise positions in the first natural wing modes resulted in a significant lift increase, particularly for the tip-mounted propeller in the first bending mode.

Kurzreferat

Die aktuelle Forschung zur Propeller-Flügel-Interaktion untersucht hauptsächlich stationäre Flügelszenarien und vermeidet die Komplexität von Flügel- und Propellerbewegungen. Diese Arbeit untersucht die aerodynamische Interaktion eines Propeller-Flügel-Systems in verschiedenen Bewegungsszenarien mit Hilfe eines neuen Simulationsrahmens namens Fluid-Motion Interaction (FMI). Der FMI-Rahmen koppelt einen Aerodynamik-Solver mittlerer Genauigkeit, DUST, mit einem in MATLAB entwickelten FMI-Solver, der mit theoretischen Daten für nickende und schlagende Flügel sowie den natürlichen Moden des Goland-Flügels und bestehender Forschung zur Propeller-Flügel-Interaktion validiert wurde. Simulationen von nickenden und schlagenden Flügeln mit starr montiertem Propeller ergaben eine spezifische reduzierte Frequenz, bei der die aerodynamische Leistung maximiert wird. Die Einführung einer relativen Bewegung zwischen Propeller und Flügel zeigte, dass die aerodynamische Reaktion mit dem Amplitudenverhältnis zwischen Propeller und Flügel skaliert und linear mit der Phasenverschiebung des Propellers variiert. Schließlich führte die Integration eines Propellers in den Goland-Flügel an verschiedenen Spannweitenpositionen in den ersten natürlichen Flügelmoden zu einer signifikanten Auftriebserhöhung, insbesondere für den an der Flügelspitze montierten Propeller in der ersten Biegemodus.

III. Declaration of Originality

I hereby declare that this thesis is entirely my own work and that any additional sources of information have been duly cited.

I have clearly referenced all sources (either from a printed source, internet, or any other source) used in the work.

This work has not been previously published and was not presented to a different examination authority.

Aachen, 09.2024

Shreyas Ashwin Sunder

IV. Contents

V. List of Figures

VI. List of Tables

VII. List of Abbreviations

Abbreviation	Description
CFD	Computational Fluid Dynamics
DBS	Downgoing Blade Side
DFT	Discrete Fourier Transform
DoF	Degree of Freedom
DSV	Dynamic Stall Vortex
eVTOL	electric Vertical Take-Off and Landing
FT	Fourier Transform
FFT	Fast Fourier Transform
FMI	Fluid-Motion Interaction
FSI	Fluid-Structure Interaction
HT	High Thrust
IU	Inboard Up
LE	Leading Edge
LEV	Leading Edge Vortex
LL	Lifting Line
LT	Low Thrust
LTI	Linear Time Invariant
MDoF	Multiple Degree of Freedom
MPI	Multi-Point Interface
OTW	Over-The-Wing
OU	Outboard Up
RANS	Reynolds-Averaged Navier-Stokes
SP	Surface Panel
TE	Trailing Edge
UBS	Upgoing Blade Side
VLM	Vortex Lattice Method
XML	Extensible Markup Language

1 Introduction

Propeller-wing interaction has recently become more important due to the increased interest in eVTOLs, air taxis, etc. The use of jet engine propulsion systems for these applications is not feasible and an ideal alternative is electric propulsion systems as they are lighter, quieter, easier to maintain and are more environment friendly over the long term. Plenty of research has been done over the years regarding electric propulsion systems with the major focus being the aerodynamic and structural performance of distributed propulsion systems and wingtip propellers.

In their paper, de Vries and Vos [1] showed a 45% increase in the local sectional lift-to-drag ratio of the wing, at the expense of a 12% reduction in propeller efficiency for an over-the-wing distributed-propulsion system. According to Vecchia and Malgieri [2], maximum achievable lift coefficient could be increased of about 20-30% in clean configuration, and more than 50% in flapped configuration for a distributed-propulsion system. They also state that induced drag can be reduced by about 2-3% at a low cruise lift coefficient and up to 8-10% at a relative high cruise lift coefficient for a tip-mounted distributed-propulsion system. Sinnige and van Arnhem [3] compared a wingtip-mounted propeller configuration with a conventional propeller-wing layout. According to their findings, the wingtip-mounted configuration showed a drag reduction of around 15% at a lift coefficient of 0.5 and a thrust coefficient of 0.12. Their reasoning for this result was wingtip-mounted propellers installed in a tractor configuration can decrease the wing induced drag by attenuating the wingtip vortex by the propeller slipstream.

Most research on propeller-wing interaction has focused on stationary wing configurations relative to the direction of freestream velocity. The key parameters affecting the wing performance by the propeller are a) slipstream contraction due to increased dynamic pressure behind the propeller b) local increase/decrease in relative angle of attack due to propeller blades moving up/down and c) increase/decrease in local lift due to propeller swirl [4–6]. Veldhuis, in his thesis, considers several factors such as propeller advance ratio and propeller position and orientation relative to the wing. According to his thesis, all these effects have an impact on wing performance [4]. This will be further verified during this thesis. This could be due to the greater complexities involved, and the difficulty in extrapolating observations and providing reasons for the results obtained. Therefore, the goal of this thesis is to perform simulations for a propeller-wing configuration with the wing and propeller being subjected to simple motions such as change in wing pitch and change in wing plunge, with a change in pitching amplitude and phase angle between wing and propeller. In addition, simulations

have been performed with a flexible wing undergoing its 1st natural bending mode shape and 1st natural torsional mode shape, and the results are presented.

To perform this study, a partitioned fluid-motion interaction (FMI) method was defined and a framework for this method has been developed. This method uses two different solvers: one aerodynamic solver (DUST) and another in-house motion solver and information is passed between each solver for each time step using a coupling library (preCICE). At the time of authoring this thesis, most structural solvers do not have the capability to provide models prescribed values of desired motions and obtaining a response to these motions while keeping computational resources low. Therefore, a solver was developed using MATLAB that could compute prescribed values of positions and velocities of different points in a user-defined model and assign various motions to the model such as pitch, plunge, eigenmotions and user-defined functions. The resulting positions and velocities are sent to the aerodynamic solver and the output forces and moments from the aerodynamic solver are analysed. The workflow followed in this thesis was:

1. Present fundamentals and summarise existing research on:
   - Simple wing motions and complex wing modes,
   - Unsteady aerodynamics of wings in motion and
   - Propeller-wing interaction for a stationary wing and propeller.
2. Develop a new framework for partitioned Fluid-Motion Interaction (FMI) simulations as well as introduce an aerodynamic solver (DUST) and a coupling library (preCICE).
3. Develop a solver in MATLAB based on the new framework, while using existing coupled black-box solvers as references.
4. Validate the newly developed solver, existing research and models used in this thesis by performing validation studies.
5. Investigate the aerodynamic performance of a wing model undergoing simple motions such as pure pitching and pure plunging combined with a:
   - Rigidly attached propeller and
   - Flexibly attached propeller.
6. Present the results obtained from simulations performed on a flexible wing with a rigidly attached propeller undergoing its 1st natural bending mode and 1st natural torsional mode.

2 Fundamentals

2.1 Wing Motions Description

2.1.1 Simple Wing Motions

Simple wing motions include pure pitching and pure plunging motions. Pitching motion of an airfoil can be defined as the simple spanwise rotation of the wing about a point located on its chord. Plunging motion of an airfoil can be defined as the simple vertical translational motion of a wing without any rotation about any of its axes. Figure 2-1 shows a basic description of pure pitching and plunging motions of an airfoil.

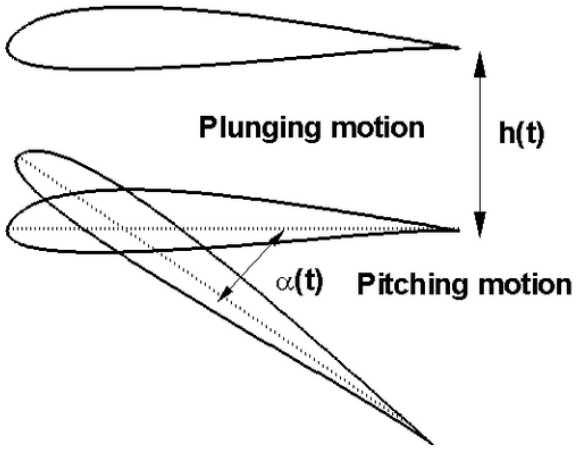

Figure 2-1: Pure pitching and plunging motions of an airfoil [7]

There are certain standard dimensionless variables used in unsteady aerodynamics. These are the reduced frequency (k), which is used to denote period of oscillations (shown in equation 2.1), normalised plunge amplitude (h), which is used to denote amplitude of plunging motions (shown in equation 2.2) and the Strouhal number (St), which is used in oscillating flow mechanisms (shown in equation 2.3).

$$k = \frac{\pi \mathrm{fc}}{u_\infty} = \frac{\omega c}{2u_\infty} = \frac{\omega b}{u_\infty} \tag{2.1}$$

$$h = \frac{h_{Max}}{c} \tag{2.2}$$

$$\mathrm{St} = \frac{2kh}{\pi} \tag{2.3}$$

Here, f is the pitching/plunging frequency, ω is the pitching/plunging circular frequency ($\omega = 2\pi f$), c is the characteristic length of the structure (for a wing, c is typically the chord length), b is the semi-chord length ($b = c/2$), u_∞ is the freestream velocity and h_{Max} is the maximum plunging amplitude.

Reduced frequency (k) defines the unsteadiness of the wing motion. For a pure oscillating motion, the equation for geometric pitching angle of attack (α) and plunge height (h) of the wing at any given point of time are shown in equations 2.4 and 2.5 respectively. Here, α_0 is the initial angle of attack of the wing, α_{Max} is the maximum angle of attack/pitching amplitude of the wing and φ is the initial phase offset of the wing motion.

$$\alpha(t) = \alpha_0 + \alpha_{Max} \sin(2\pi f t + \varphi) \quad 2.4$$

$$h(t) = h_{Max} \sin(2\pi f t + \varphi) = hc \sin(\omega t + \varphi) \quad 2.5$$

2.1.2 Complex Wing Modes

Complex wing modes comprise of the eigenmotions of the wing. Eigenmotions describe the intrinsic oscillatory behaviours of a wing, which arise due to the interaction between the wing's elastic structure and the aerodynamic forces acting upon it. These modes are important in the analysis of aeroelasticity, where the wing's flexibility can lead to potentially unstable oscillations, and subsequently cause structural damage (flutter). Unlike simple motions such as pitch and plunge, eigenmotions are more complex, involving coupled deformations and higher-order behaviours that can occur at specific frequencies. These behaviours are mathematically characterized by eigenvalues and eigenvectors, which are fundamental concepts in structural dynamics:

a) **Eigenvalues (λ)**: Eigenvalues represent the natural frequencies at which the system (the wing) vibrates when subjected to external disturbances. Each eigenvalue corresponds to a specific mode of vibration, and its magnitude indicates how quickly oscillations occur in that mode.
b) **Eigenvectors (ϕ)**: Eigenvectors (or mode shapes) describe the pattern of deformation for each corresponding eigenvalue. While the eigenvalue tells you how fast the oscillation occurs, the eigenvector shows the actual shape the wing takes during that vibration mode.

Eigenvalues and eigenvectors are derived by solving the system's dynamic equation of motion, which includes both the stiffness (elastic properties of the wing) and the mass distribution, combined with the aerodynamic forces acting on the wing. The MDoF dynamic motion equation is defined in equation 2.6.

$$M\ddot{q}(t) + C\dot{q}(t) + Kq(t) = F(t) \quad 2.6$$

Here, M is the mass matrix, C is the damping matrix, K is the stiffness matrix, q is the vector of generalised coordinates (describing wing deformation) and F is the external force. The mass, stiffness and damping matrices are unique to the wing's geometry, material properties. It can also be seen that the eigenvalues and eigenvectors are highly dependent on the boundary conditions, and

aerodynamic loading as they influence the external force component (F) [8, 9]. To solve the motion equation, an initial solution is assumed for q. This solution is provided in equation 2.7, with λ and ϕ being the eigenvalues and eigenvectors, respectively.

$$q(t) = \phi e^{\lambda t} \tag{2.7}$$

To capture the natural behaviour of the system, the external force (F) can be equated to 0. This is known as the homogenous solution of the system. Introducing the initial assumed solution into the motion equation (equation 2.6) and upon further simplification, the motion equation can be written as a quadratic eigenvalue problem, as shown in equation 2.8.

$$(M\lambda^2 + C\lambda + K)\phi = 0 \tag{2.8}$$

Solving this equation gives us the eigenvalues and eigenvectors of the homogenous system. The equation can be solved by linearising the problem, which is done by means of state-space representation, as given in equation 2.9.

$$x(t) = \begin{pmatrix} q(t) \\ \dot{q}(t) \end{pmatrix} \tag{2.9}$$

This gives the first order differential equation as shown in equation 2.10.

$$\frac{d}{dt}\begin{pmatrix} q \\ \dot{q} \end{pmatrix} = \begin{pmatrix} 0 & I \\ -M^{-1}K & -M^{-1}C \end{pmatrix}\begin{pmatrix} q \\ \dot{q} \end{pmatrix} = A\begin{pmatrix} q \\ \dot{q} \end{pmatrix} \tag{2.10}$$

The matrix equation 2.10 is of the form shown in equation 2.11.

$$\begin{gathered} \dot{x}(t) = Ax(t), \\ A = \begin{pmatrix} 0 & I \\ -M^{-1}K & -M^{-1}C \end{pmatrix} \end{gathered} \tag{2.11}$$

The eigenvalue problem (equation 2.8) can now be written as shown in equation 2.12.

$$Ax = \lambda x \tag{2.12}$$

Solving this for λ gives the eigenvalues, which will likely be complex due to the damping. The real part of λ corresponds to the damping effect (decay or growth rate), while the imaginary part corresponds to the oscillation frequency. Each eigenvalue (λ_i) has a corresponding eigenvector (ϕ_i), which represents the mode shape for that frequency. Eigenvectors are often normalised to ensure a standardized, unique, and computationally stable representation, making them easier to interpret and work with. This is done by dividing the eigenvector by the Euclidean norm (or 2-norm), which is calculated as the square root of the sum of the squares of the vector's components, as shown in equation 2.13. Here, $\widehat{\phi_i}$ is the normalised eigenvector and $\|\phi\|_2$ is the Euclidean norm of the eigenvector.

$$\widehat{\phi_i} = \frac{\phi_i}{\|\phi_i\|_2}$$
$$\|\phi\|_2 = \sqrt{{\phi_1}^2 + {\phi_2}^2 + \cdots + {\phi_n}^2} \qquad 2.13$$

The primary mode shapes typically observed in wing structures are:

1. **Bending Modes**
   - First Bending Mode: This is the simplest mode, where the wing bends upwards or downwards along its span. The deformation is symmetric about the wing's chord (see Figure 2-2).
   - Higher-Order Bending Modes: These involve more complex bending patterns with additional nodes (points of zero displacement) along the span. For instance, the second bending mode might have an "S" shape.

Figure 2-2: First natural bending mode of a wing

2. **Torsional Modes**
   - First Torsional Mode: In this mode, the wing twists around its longitudinal axis. This mode is crucial as it can couple with aerodynamic forces, leading to phenomena like flutter (see Figure 2-3).
   - Higher-Order Torsional Modes: These involve more complex twisting patterns, often with nodes along the wing's span.

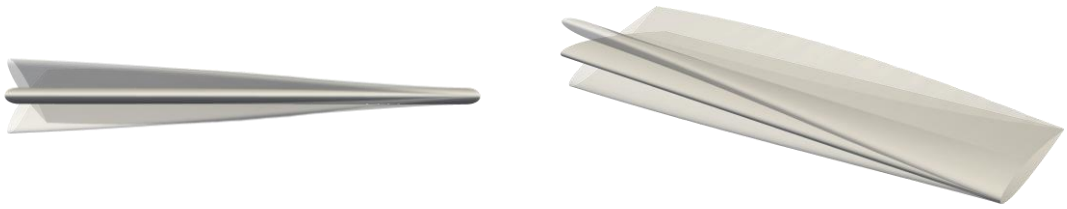

Figure 2-3: First natural torsional mode of a wing

3. **Coupled Bending-Torsion Modes**
   - In real wings, bending and torsion often couple due to the wing's elasticity and aerodynamic loading. These modes involve simultaneous bending and twisting, which can lead to complex vibration patterns.

2.2 Unsteady Aerodynamics of Wings in Motion

The aerodynamic forces of a stationary wing (relative to the free flow direction) can be easily calculated through analytical methods. Realistically, an aircraft and in turn the wings of an aircraft undergo desirable motions to produce lift/thrust and are also subjected to sudden external forces (Ex. Gusts of wind). This creates a non-linear, unsteady state of motion of the wing and simple analytical methods are not sufficient to predict the aerodynamic performance of the wing in these situations. Before studying the effects of a propeller on a transient wing, i.e. a wing-propeller system undergoing pure pitching, pure plunging, complex mode shapes, etc. are studied, the results of the standalone wing undergoing these motions must be observed. In this chapter the analytical methods as well as the necessary equations to predict the performance of pitching and plunging standalone wings are described in detail.

2.2.1 Theodorsen's Unsteady Two-Dimensional Thin Airfoil Theory

Theodorsen's two-dimensional unsteady thin airfoil theory [9, 10] is a foundational concept in aerodynamics that addresses the behaviour of airfoil (wing cross-sections) in unsteady (time-dependent) flow conditions. This theory is particularly important for understanding the dynamics of wings and blades in oscillatory motion, such as those found in flapping flight or rotating machinery. His theory is based on potential flow theory, where the flow is incompressible and irrotational and the complex potential function that describes the flow around an airfoil. He defines a function called Theodorsen's function which relates the unsteady lift of an airfoil to its motion. The function $C(k)$, is a complex-valued function of reduced frequency (k) defined in equation 2.14. where the $K_j(ik)$ ($j = 0, 1, \ldots$) terms are modified Bessel functions of the second kind and $H_n^{(2)}$ are Hankel functions of the second kind. Although an explanation of Bessel and Hankel functions is beyond the scope of this thesis, these functions are included in many software libraries and are easy to compute.

$$C(k) = F(k) + iG(k) = \frac{{H_1}^{(2)}(k)}{{H_1}^{(2)}(k) + i{H_0}^{(2)}(k)} = \frac{K_1(ik)}{K_0(ik) + K_1(ik)} \qquad 2.14$$

Figure 2-4 shows the plot of Theodorsen function for different reduced frequency values. The plots on the left are the values of $F(k)$ (real component) and $G(k)$ (imaginary component).

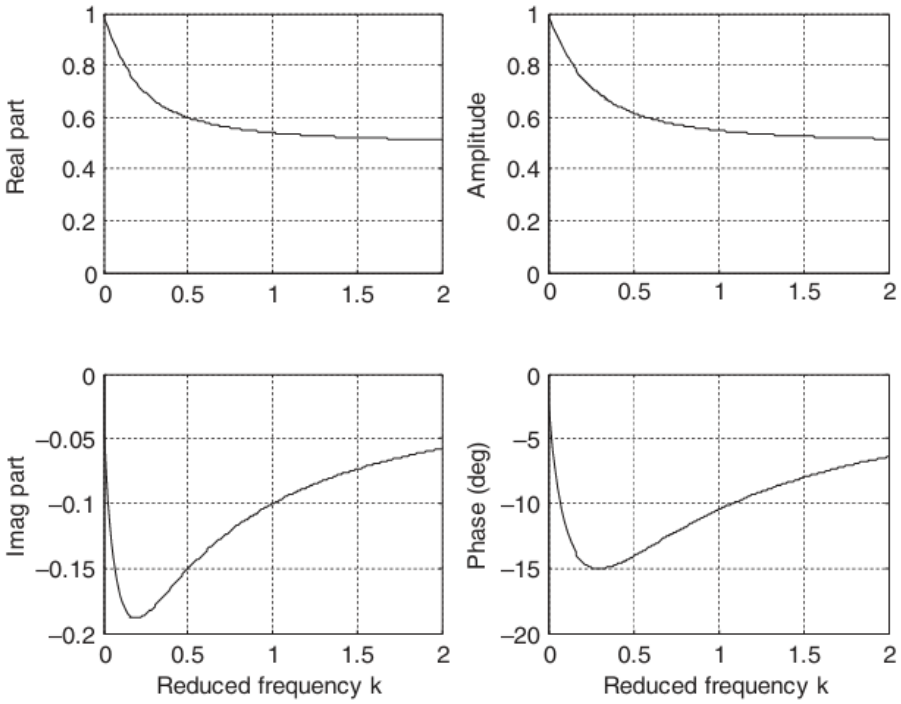

Figure 2-4: Theodorsen function, *C(k)* vs reduced frequency (*k*) [11]

The complex representation of the Theodorsen function for different values of k (shown in Figure 2-5) is the plot of the transfer function, i.e. the representation of the Theodorsen function in the frequency domain. For quasi-steady conditions, $\omega = 0$, i.e. $k = 0$ and hence $F = 1$ and $G = 0$. Although the Theodorsen function has a limit of $k \to \infty$, for a full-sized aircraft k has a maximum value of the order of unity.

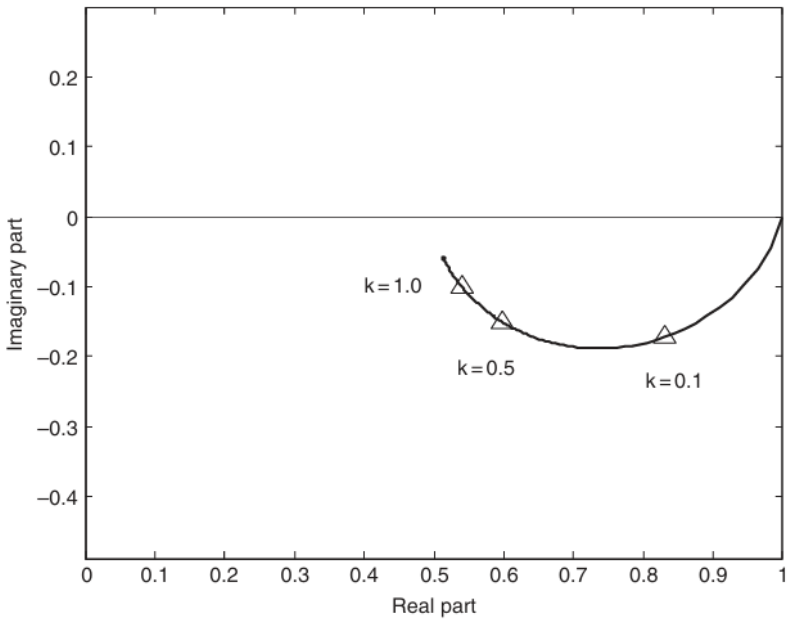

Figure 2-5: Complex plane representation of Theodorsen function, *C(k)* [11]

The lift force per unit span (L') and moment force per unit spam (M') according to Theodorsen's two-dimensional unsteady thin airfoil theory [9, 10] are given in equations 2.15 and 2.16 respectively. Here, b is the semi-chord length ($c_W/2$)* and a is the location of the elastic axis relative to the mid-chord. For a simple 2-D airfoil not undergoing deformation, the pitching axis can be considered as the elastic axis. Since this equation was derived for a flat-plate (thin airfoil), the lift-curve slope is 2π.

$$L' = \pi\rho b^2\left[\ddot{h} + u_\infty\alpha - ba\ddot{\alpha}\right] + 2\pi\rho u_\infty bC(k)\left[\dot{h} + u_\infty\alpha + b\left(\frac{1}{2} - a\right)\dot{\alpha}\right] \quad 2.15$$

$$\begin{aligned} M' = {} & \pi\rho b^2\left[ba\ddot{h} - u_\infty b\left(\frac{1}{2} - a\right)\dot{\alpha} - b^2\left(\frac{1}{8} + a^2\right)\ddot{\alpha}\right] \\ & + 2\pi\rho u_\infty b^2\left(a + \frac{1}{2}\right)C(k)\left[\dot{h} + u_\infty\alpha + b\left(\frac{1}{2} - a\right)\dot{\alpha}\right] \end{aligned} \quad 2.16$$

In both equations 2.15 and 2.16, the first part of each expression (independent of $C(k)$) are the non-circulatory components and the second part of each expression (dependent on $C(k)$) are the circulatory components. Upon further simplification, the maximum lift and moment forces per unit span according to Wright and Cooper [9] are shown in equations 2.17 and 2.18 respectively.

$$L'_{Max} = \rho {u_\infty}^2 b\left[(L'_h + ikL_{\dot{h}})\frac{h_{Max}}{b} + (L'_\alpha + ikL'_{\dot{\alpha}})\alpha_{Max}\right] \quad 2.17$$

$$M'_{Max} = \rho {u_\infty}^2 b^2\left[(M'_h + ikM'_{\dot{h}})\frac{h_{Max}}{b} + (M'_\alpha + ikM'_{\dot{\alpha}})\alpha_{Max}\right] \quad 2.18$$

The coefficients L'_h, $L'_{\dot{h}}$, L'_α, $L'_{\dot{\alpha}}$, M'_h, $M'_{\dot{h}}$, M'_α and $M'_{\dot{\alpha}}$ are the non-dimensional oscillatory aerodynamic derivatives. These derivatives are expressed in terms of normalised displacements and velocities for pitch and plunge. The non-dimensional oscillatory aerodynamic derivatives for the lift force are shown in equation 2.19.

$$\begin{aligned} L'_h &= 2\pi\left(-\frac{k^2}{2} - Gk\right) \\ L'_{\dot{h}} &= 2\pi F \\ L'_\alpha &= 2\pi\left[\frac{k^2 a}{2} + F - Gk\left(\frac{1}{2} - a\right)\right] \\ L'_{\dot{\alpha}} &= 2\pi\left[\frac{1}{2} + F\left(\frac{1}{2} - a\right) + \frac{G}{k}\right] \end{aligned} \quad 2.19$$

* The subscripts W and P will be used throughout this thesis to differentiate between shared properties of the wing and propeller respectively (Ex. Chord length, lift coefficient, phase offset, etc.).

The non-dimensional oscillatory aerodynamic derivatives for the moment force are shown in equation 2.20.

$$
\begin{aligned}
M'_h &= 2\pi\left[-\frac{k^2 a}{2} - Gk\left(\frac{1}{2}+a\right)\right] \\
M'_{\dot{h}} &= 2\pi F\left(\frac{1}{2}+a\right) \\
M'_\alpha &= 2\pi\left[\frac{k^2}{2}\left(\frac{1}{8}+a^2\right) + F\left(\frac{1}{2}+a\right) - Gk\left(\frac{1}{2}+a\right)\left(\frac{1}{2}-a\right)\right] \\
M'_{\dot{\alpha}} &= 2\pi\left[-\frac{1}{2}\left(\frac{1}{2}-a\right) + F\left(\frac{1}{2}+a\right)\left(\frac{1}{2}-a\right) + \frac{G}{k}\left(\frac{1}{2}+a\right)\right]
\end{aligned}
\qquad 2.20
$$

Equations 2.17 and 2.18 can be used to validate and compare the aerodynamic performance of pure pitching and pure plunging airfoil. Since these equations are valid for a flat plate/thin airfoil, a difference is naturally observed when these values are compared to the lift and moment forces of airfoil with thickness.

2.2.2 Analysis of Resulting Wing Forces

For a simple sinusoidal pitching/plunging motion of the wing, the resulting forces on the wing are also sinusoidal, with the same oscillating frequency as the input motion. This can be observed in Figure 2-6 where the input signal (motion) and the output signal (lift force) have been plotted for pitching and plunging motions.

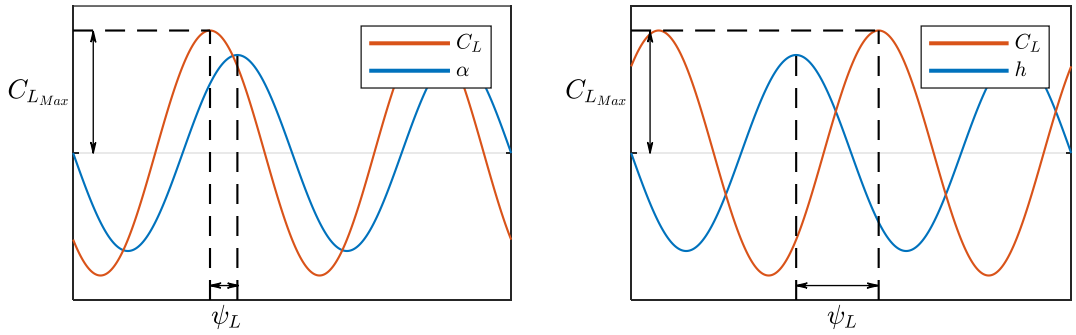

Figure 2-6: Sinusoidal motion input and lift output for pitching (Left) and plunging (Right) wings

It can also be observed that there exists a phase change between the output and input signal. This phase shift is a result of the complex interplay between the wing's aerodynamic forces and its dynamic response:

1. **Dynamic Response of the Wing**: When a wing undergoes pitching or plunging motions, its aerodynamic characteristics change over time. The wing's response to these changes does not occur instantaneously due to inertia and the time it takes for airflow to adjust. This results in a phase shift between the input motion and the resulting aerodynamic forces.

2. **Frequency Response**: The frequency of the input motion affects the phase shift. At different frequencies, the aerodynamic forces react differently. For instance, if the wing is oscillating at a frequency where its natural frequency of vibration is close, the aerodynamic forces can exhibit significant phase shifts due to resonance effects.
3. **Added Mass Effect**: When the wing moves through the air, it essentially "drags" a certain amount of air with it, creating an added mass effect. This effect also introduces a phase shift between the motion of the wing and the resulting aerodynamic forces because the forces are not only dependent on the motion but also on the interaction with the surrounding air mass.

It must be noted that for plunging airfoil, a positive value of h (upwards motion) produces a downward component of flow velocity which is depicted in Figure 2-7. Hence, a large phase lag can be observed in the plunging case in Figure 2-6.
The equations for the resulting lift and moment coefficients for a sinusoidal input motion are given in equation 2.21.

$$C_L(t) = C_{L_{Max}} \sin(\omega t + \psi_L)$$
$$C_M(t) = C_{M_{Max}} \sin(\omega t + \psi_M) \qquad 2.21$$

$C_{L_{Max}}$ and $C_{M_{Max}}$ are the maximum lift and moment coefficients respectively, while ψ_L and ψ_M are the lift and moment phase shifts, respectively.

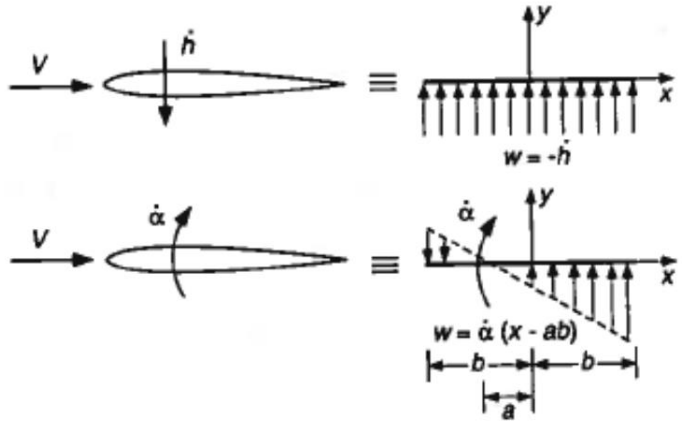

Figure 2-7: Vertical velocity component (*w*) due to pitching and plunging motions according to Thin Airfoil Theory [12]

The phase shifts result in the formation of hysteresis loops in the force vs amplitude plots. These hysteresis loops formed are crucial in studying effects like dynamic stall, vortex shedding, etc. The lift-hysteresis loops are typically centred about the 0° geometric angle of attack static wing lift and are formed clockwise. These loops increase in width for an increase in both reduced frequency and pitching/plunging amplitude. For small values of reduced frequency and pitching/plunging amplitudes, the increase in width occurs equally on opposite

sides of the quasi-steady/steady lift-curve slope (for plunging wings, the lift vs α_{eff} curve is considered) [7, 13–16].

Transfer functions are a way of describing the frequency and phase response of a LTI (linear time invariant) system. The system can be anything with a measurable input and output, e.g. mechanical spring/mass/dampers, electronic RLC circuits, etc [17, 18]. The transfer function for pitching and plunging wings can be plotted to observe the aerodynamic (and structural) response of the wing for different frequencies of pitch/plunge. Plotting the transfer functions can provide us with several observations such as:

1. **Stability Analysis:** The location of the poles in the complex plane (especially the real part) directly indicates the system's stability.
2. **System Behaviour:** The real or the complex plane plot provides a clear visualization of how the system behaves at different frequencies, aiding in a deeper understanding of its dynamic characteristics.
3. **Damping and Stiffness Characteristics:** The real parts of the lift and moment transfer functions are correlated to the aerodynamic stiffness while the imaginary parts are correlated to the aerodynamic damping of the system. These observations are important while studying flutter characteristics of the system.

To calculate the lift and moment transfer functions (H_L, H_M), the ratio of the output to input Fourier transforms (FT) is calculated. Fourier transform is the frequency representation of a time domain signal. The Fourier transforms of the output signal (Y) and the input signal (X) are obtained by using the 'FFT' function (Fast Fourier Transform) in MATLAB. This 'FFT' function computes the Discrete Fourier Transform (DFT) of the signal. The DFT helps in identifying dominant frequencies and understanding the signal's frequency components [19]. An example of the FFT output for a signal with three dominant frequencies is shown in Figure 2-8. While the time history does not provide us with valuable information, the FFT output gives us the discrete signal frequencies and their amplitudes present in the complete signal.

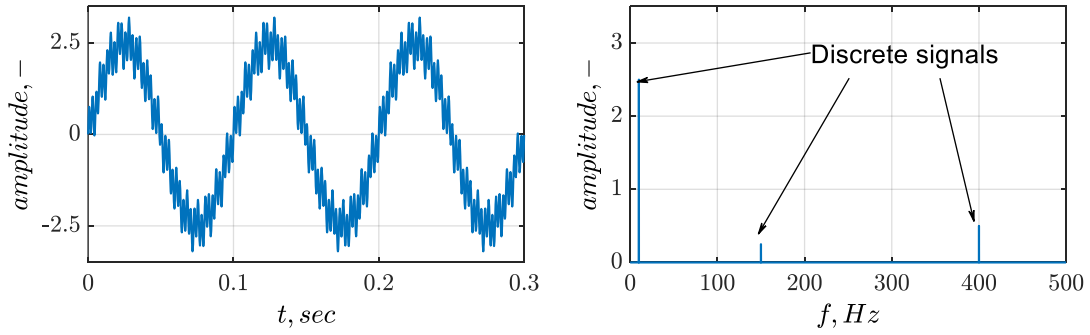

Figure 2-8: Example of a signal with multiple sub-signals in time domain (Left) and its FFT output (Right)

For a complex system such as a wing-propeller model in motion, the wing and propeller outputs can be isolated by means of their oscillating/rotating frequencies and study their individual influences using this method. The transfer functions are unique to the oscillating frequencies. Since the reduced frequency is commonly used in wing pitch/plunge motions, the transfer functions will also be represented as a function of the reduced frequency. The lift and moment transfer functions are given in equation 2.22.

$$H(k) = \frac{Y(k)}{X(k)} \tag{2.22}$$

Here, Y is the Fourier transform of $L(t), M(t)$ and X is the Fourier transform of $\alpha(t), h(t)$. The formulae for the output and input Fourier transforms are given in equation 2.23.

$$\begin{aligned} Y(k) &= FFT\big(L(t), M(t)\big) \\ X(k) &= FFT\big(\alpha(t), h(t)\big) \end{aligned} \tag{2.23}$$

The transfer function is represented on the complex plane, depicted in Figure 2-9.

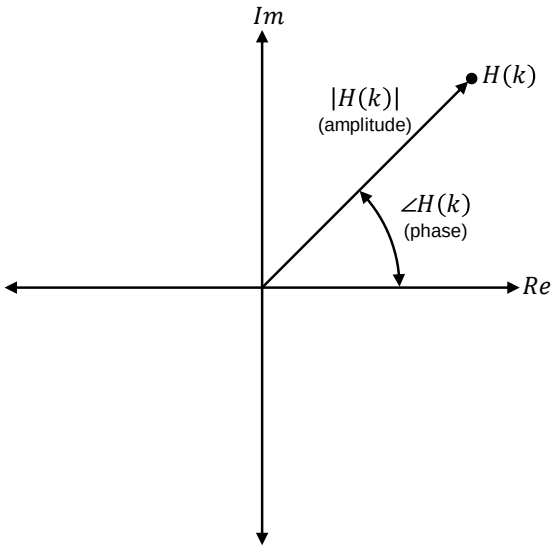

Figure 2-9: Complex plane representation of a transfer function

2.3 Propeller-Wing Interaction: Stationary Wing and Propeller

The addition of propellers to wings is done to increase the overall performance of the wing. Some of the advantages of using propellers are increased wing lift-drag ratio, high lift capabilities, short take-off and landing capabilities, high fuel efficiency at low speeds and reduced flyover noise. There are some disadvantages of using propellers such as needing a higher ground clearance, altitude restrictions, limited speed and aeroelastic disadvantages but overall, the

pros outweigh the cons and wings with propellers are considered more efficient for low and low-to-mid range flights [5, 20–24].

The effects of the propeller on the wing as well as the wing's influence on the propeller have been studied in detail by many for a tractor configuration (i.e. the propeller is ahead of the wing) with the former being the major focus of research. In this chapter, studies which focus on the overall interaction between the wing and the propeller will be reviewed.

There are 3 main parameters that contribute to the increase/decrease of lift and drag over a wing due to the influence of the propeller, specifically the propeller wake. These 3 parameters are:

1. The increase in dynamic pressure (q) behind the propeller by slipstream contraction.
2. The increase/decrease in swirl due to the propeller rotation.
3. The increase/decrease in local angle of attack by the blade rotation direction.

The various parameters and how they affect the wing inflow for a conventional tractor configuration and inboard up rotation (IU) is shown in Figure 2-10.

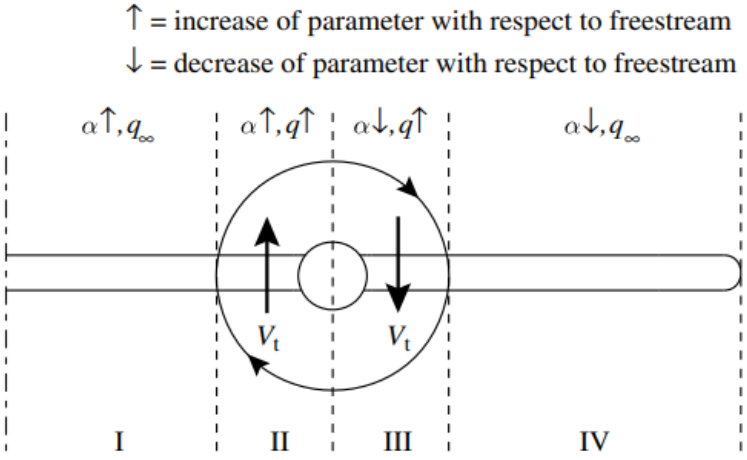

Figure 2-10: Parameter variation for a tractor configuration propeller with inboard up rotation [3]

The wing inflow region can be divided into 4 sections. Sections II and III are the regions of wing inflow directly behind the wing with section II being the region with the propeller blades moving upward and section III being the region with the propeller blades moving downward. In both regions, the local dynamic pressure increases due to an increase in flow velocity behind the propeller. The dynamic pressure distribution downstream of a propeller is shown in Figure 2-11. The maximum dynamic pressure is usually located around 70-90% of the propeller radius and is uniformly distributed around the propeller. This can be observed in Figure 2-11 and Figure 2-12.

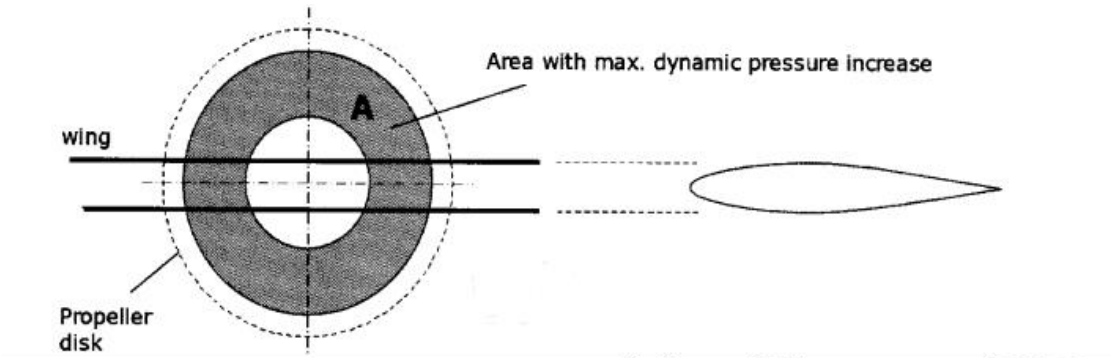

Figure 2-11: Increase in average dynamic pressure over the wing for a propeller in a tractor configuration [4]

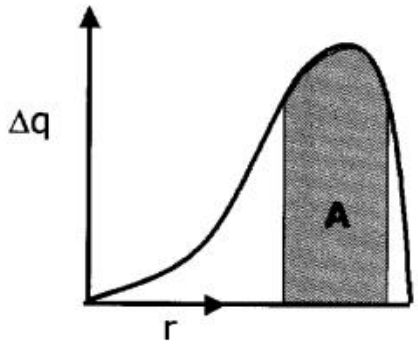

Figure 2-12: Increase in dynamic pressure in the radial direction for a propeller [4]

Due to the blades moving upwards in section *II*, the angle of attack and the tangential velocity in this region increase whereas the downward motion of the blades in section *III* causes the opposite effect and decrease the angle of attack and tangential velocity. Altogether, the local lift force in section *II* increases, in section *III*, the lift force can either increase or decrease based on which parameter is more dominant, i.e. lift force increases if the increase in lift due to dynamic pressure is greater than the decrease in lift due to the decrease in local angle of attack and vice-versa.

The changes in these parameters also affect the surrounding regions i.e. sections *I* and *IV*. Due to an increase in angle of attack and tangential velocity in section *II*, the angle of attack in section *I* (region closest to the fuselage) also increases and hence the lift force in this region increases. Likewise, the decrease in angle of attack and tangential velocity decreases the angle of attack in section *IV* (region closest to the wingtip) and hence decreases the lift in this region. But in most cases, the propeller causes an increase in overall wing lift and induces drag. It has also been observed in most studies that the overall increase in swirl for an inboard up (IU) rotation configuration can counter the effect of the wingtip vortices hence increasing the effective aspect ratio of the wing and therefore the induced drag. This brought about numerous studies studying the benefits of wingtip-mounted inboard up rotating propeller-wing systems. The advantages stated

above are observed in most cases but there is also a reduction in overall wing lift due to the decrease in overall wing area washed by the propeller wake as well as an increase in aeroelastic penalties. Most of the wingtip mounted inboard up rotating systems do show better wing performance but it must be noted that the performance highly depends on the individual models and cannot be conclusively assumed to be better than conventional wing-propeller models. The various propeller parameters and their effects on the wing lift and drag forces for a purely conventional design are given in Table 2-1.

Table 2-1: Propeller effects on wing for a purely conventional configuration [3–6]

Parameter	Effect on Wing Lift (C_L)	Effect on Wing Drag (C_D)
Rotation Direction (IU or OU)	IU rotation increases C_L. OU rotation increases C_L (less than IU rotation).	IU rotation decreases C_D. OU rotation increases C_D.
Advance Ratio (J)	As J increases, C_L decreases.	As J increases, C_D decreases.
Spanwise Position ($y_P/b_W/2$)	As $y_P/b_W/2$ increases, C_L increases.	As $y_P/b_W/2$ increases, C_D decreases.
Propeller Inclination (α_P)	As α_P increases, C_L decreases.	As α_P increases, C_D increases.

The position, orientation and operating conditions of the propeller all play a part in the performance of the wing. As seen from the literature [3–6], the propeller-wing design space is complex and although in most cases, IU rotating wingtip propellers show superior performance, it is highly dependent on the wing design and propeller positioning. There is little to no research available regarding the propeller-wing interaction where the wing is either undergoing simple or complex motions. All research on propeller-wing interaction involves a stationary wing and propeller model (with respect to the freestream). To avoid complexities which cannot be explained due to a lack of available research, the simulations done during this thesis will be for simple rectangular wing planforms with no twist, sweep or dihedral.

3 Development of a Framework for Fluid-Motion Interaction (FMI) Simulations

3.1 Introduction to Partitioned Fluid-Motion Interaction Simulations

Fluid–structure interaction (FSI) is the interaction of some movable or deformable structure with an internal or surrounding fluid flow. Fluid–structure interactions can be stable or oscillatory. In oscillatory interactions, the strain induced in the solid structure causes it to move such that the source of strain is reduced, and the structure returns to its former state only for the process to repeat [25]. In partitioned simulations of fluid-structure interaction, the flow and the displacement of the structure are calculated separately and coupling iterations between the fluid/aerodynamic solver and the structural solver are required to calculate the solution of the coupled problem if the interaction is strong, as opposed to a monolithic FSI simulation where one solver performs both structural and aerodynamic calculations [26]. Example of monolithic FSI solvers is modern CFD solvers such as ANSYS, StarCCM+, etc.

Each solver uses a “black box” approach where each solver does not concern itself with the inner workings of the other solver. A fluid/aerodynamic solver will only calculate the forces and moments during each time step of the simulation but does not use these values to calculate the subsequent positions and velocities that occur because of said forces. To do this, a structural solver is used. Each one of these solvers has their own functions and specific formats in which they output. To ensure timely communication of these forces and displacements between the two software, a coupling software is required. This coupling software does not perform any calculations regarding forces or displacements by itself, i.e. it is not a solver but only a coupling tool.

In regular FSI simulations, the structural solver uses the mass, stiffness, and damping matrices to solve the equation of motion for a multi-degree-of-freedom (MDoF) system. The outputs from the structural solver are the positions and velocities of each DoF for the given time step. To study the system's response to specific motions, these positions and velocities can be calculated using simple equations (harmonic/constant motion equations, linear/rotatory motion equations) without involving the structural characteristics of the system and then directly fed into the fluid solver. Since the response from the fluid solver is to a pre-defined motion and not a response due to the structural characteristics of the system, i.e. a motion response, these types of simulations can be called Fluid-Motion Interaction (FMI) simulations. An in-house motion solver was developed based on this novel framework. This solver will be described in detail in chapter 3.4.

3.2 Introduction to the Coupling Software: preCICE

To translate and synchronise the outputs amongst each solver, another software is required whose sole purpose is managing intercommunication between multiple solvers. The coupling software currently compatible with DUST is preCICE [27–29]. preCICE is a coupling library that is written primarily in C++ but has bindings for numerous other coding software such as Fortran, Python (used by DUST), MATLAB, Julia, and Rust.

preCICE uses an XML file for the settings configuration. As seen in Figure 3-1, preCICE connects two (or more) adapters; one for each solver which convert the output from solver A to a valid format and is sent to the other adapter which converts the formatted output into its desired format and sends it to solver B. Solver B performs its tasks and provides an output to the adapter, which converts it into a similar or different valid format. This output is then sent back via preCICE to Solver A's adapter, where it is converted into Solver A's desired format before being passed to Solver A. This cycle keeps repeating until either the solvers or preCICE reaches its final time step. The connection is made by either sockets or MPI ports.

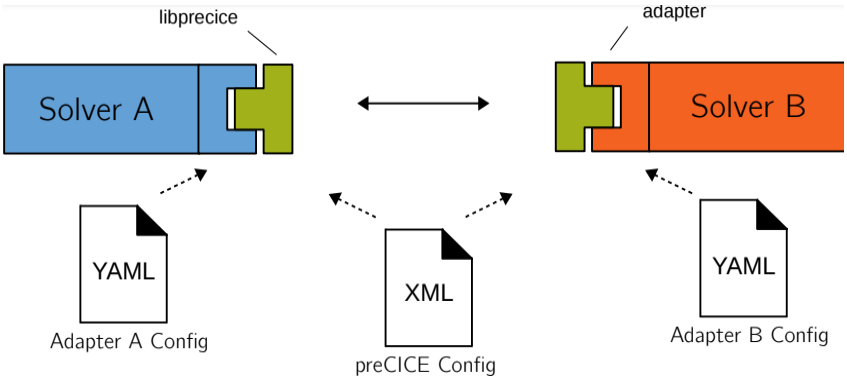

Figure 3-1: preCICE workflow [28]

Data is mapped between two solvers using nodes, with each node representing a point in the solver's mesh. preCICE utilizes these nodes to map the meshes and transmit data at each time step. For simplicity, the number and positions of nodes should be identical in both solvers. If not, various mapping schemes are available to transfer data between the meshes [28]. In this thesis, this complexity was avoided by ensuring that the coupling nodes are identical in both meshes. Figure 3-2 is an example of how communication occurs between DUST and the in-house solver (written in MATLAB). DUST always requires initial values of position and velocity for each node to set up the model and hence, it is considered as the second solver. The solver contains positions, velocities, orientations, and angular velocities for each node and sends this data to preCICE through an in-house preCICE-MATLAB adapter. preCICE maps the data from the MATLAB mesh nodes onto the nodes in the DUST mesh. The DUST adapter (pre-built in

DUST) translates this data to the DUST solver and DUST performs calculations of forces and moments. This data is mapped back onto the DUST mesh nodes by the DUST adapter and is sent to preCICE. preCICE takes these values and maps it onto the MATLAB mesh nodes. The preCICE-MATLAB adapter receives the forces and moments for each node, converts it into the desired format and sends it to the MATLAB solver which performs its functions.
Since the solvers operate one after the other, it is a serial-type coupling scheme. There are two types of coupling systems used by preCICE: a) explicit and b) implicit coupling systems. In an explicit coupling system, each solver is executed only once per time step whereas in an implicit coupling system, the solvers are executed repeatedly in a single time step until convergence occurs. This is done by using several methods such as using an accelerating scheme, adjusting the convergence requirements, etc.

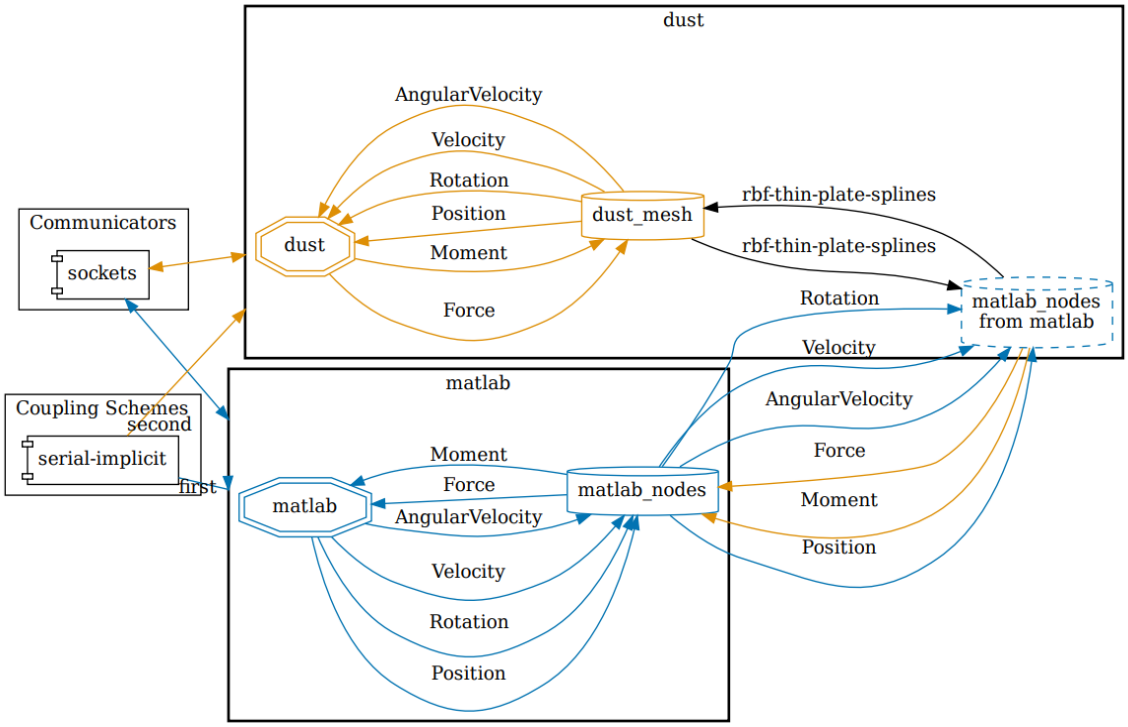

Figure 3-2: DUST-preCICE-motion solver workflow

3.2.1 Workflow for a Partitioned FMI Simulation

The general workflow between DUST, preCICE and the motion solver is shown in Figure 3-3. Here the data transfer between the two solvers and preCICE for a single time step is considered. The colours blue, green, red, and purple signify a variable or a function used by the preCICE-MATLAB adapter, motion solver, preCICE and the DUST adapter, respectively. Boxes with dashed lines indicate the adapters used by the motion solver and DUST.

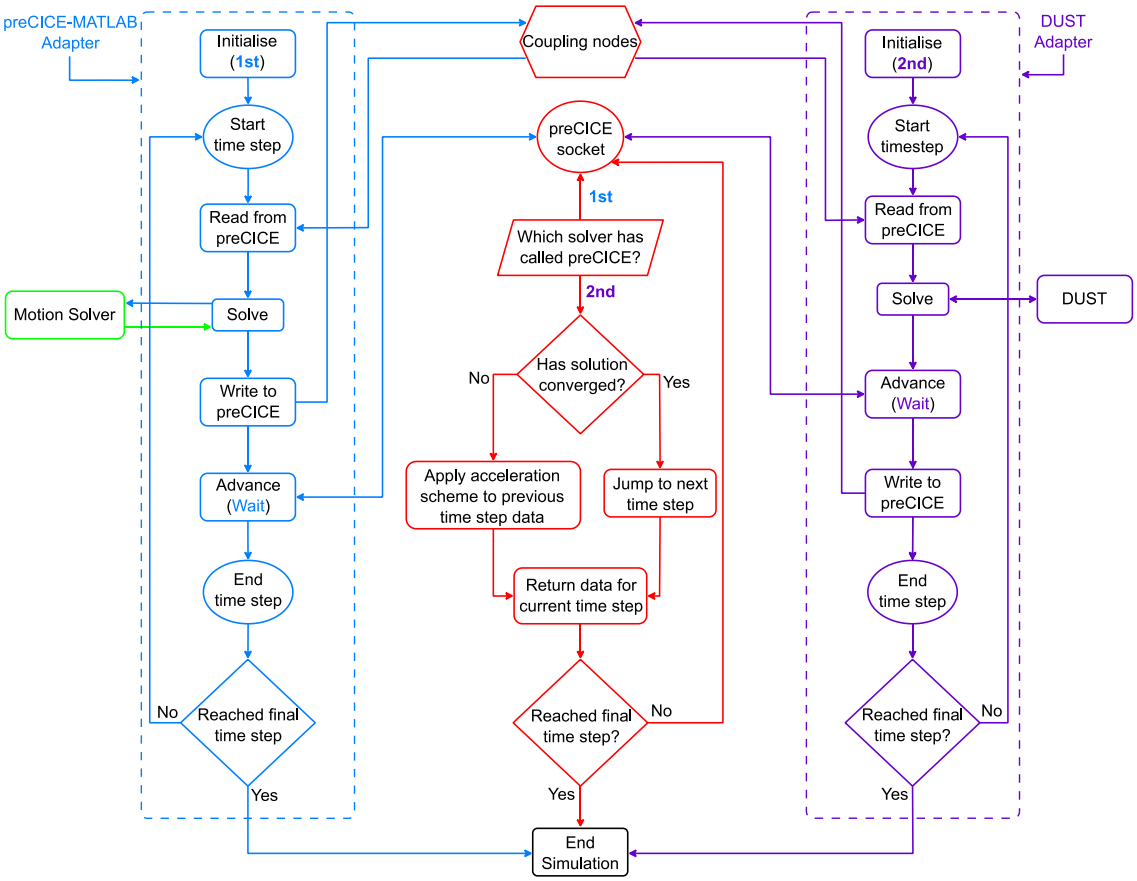

Figure 3-3: Workflow of a coupled simulation between DUST, preCICE and the motion solver

The preCICE-MATLAB adapter was created to link the in-house motion solver with preCICE (version v2.5.0). It receives the data via a simple socket connection created by the adapter which acts as the host and the in-house motion solver acts as a server. The adapter has been written entirely in Python. There are multiple adapters available on the preCICE website, but this adapter uses a framework similar to the MBDyn adapter (MBDyn is a structural solver which is recommended by the DUST developers to perform coupled simulations) which is provided while installing DUST [30, 31]. The workflow of the preCICE-MATLAB adapter (highlighted in blue) and the workflow of the DUST adapter (highlighted in purple) are represented in Figure 3-3. Unlike the adapter in DUST, the preCICE-MATLAB adapter's workflow is much simpler.

The adapter uses the 'pyprecice' library which is the Python bindings for preCICE. The 'pyprecice' library contains functions to send and receive data as well as flag functions such as '$is\_read\_data\_available()$' and '$is\_write\_data\_required()$' which are used to synchronise the timings between preCICE and the adapter. The mesh used by the motion solver and preCICE are just coupling nodes which are provided in a text file by the user before the simulation begins. Each of the coupling nodes needs to be unique and have the same dimensions as the type of simulation: for a d-dimensional simulation with n coupling nodes, the coupling

nodes text file must contain n rows and d columns with each row (usually) being the x, y and z co-ordinates of the coupling nodes.
The adapter contains an interface for the data received from the motion solver which saves different variables provided by the motion solver such as position, velocity, orientation, angular velocity, force and moment in their respective fields along with a tag for each variable stating whether the provided variable must be read by or written to preCICE. The adapter also contains functions that translate the data received from the motion solver into the format required by the DUST adapter and vice-versa: information transmitted by the motion solver is an array of size $[(4 * n * d + 1) \times 1]$ (last element in array is the current time step) and data transmitted by DUST is an array of size $[4 * n \times d]$ where n is the number of coupling nodes and d is the total dimensions of the simulation.
The motion solver is initialised and waits for the data from preCICE. The solver works with displacements and velocities which are always 0 for the first step. preCICE sends a signal to the adapter to send data to the MATLAB solver. The adapter sends an array of zeros to the solver and the solver performs its functions. Once the solver has completed the calculation for the 1st time step, it sends it back to the adapter which converts the data to the desired format and signals to preCICE that it is ready to send data to the other adapter. The adapter then receives a signal from preCICE, and the data is sent. Now it waits for the data from the other adapter to arrive as well as a signal from preCICE to either repeat the current time step or begin the next time step. Since the motion solver is the first solver to run the step, there is no check done by preCICE for convergence. Instead, it should be done by the motion solver itself, but this is yet to be implemented. In all current functions of the motion solver, there has been no need for a convergence check but may be of use for further updates to the solver.
Both solvers, along with their adapters are initialised together (the DUST adapter is simply a set of functions built in the DUST source code). As stated before, the motion solver is regarded as the 1st solver and DUST is regarded as the 2nd solver. Initial values of forces and moments (all are equal to 0 for the 1st time step) are provided by the preCICE-MATLAB adapter to the motion solver and the solver returns the positions and velocities for the 1st time step back to the adapter. The values are formatted and sent to preCICE via coupling nodes and now the preCICE-MATLAB adapter enters an '$Advance()$' function where it sends a signal to preCICE that it has completed the current iteration via the socket created initially and waits for a reply from preCICE as to when it can begin its next step. preCICE now checks which solver has called the '$Advance()$' function. When the 1st solver has called the '$Advance()$' function, it asks the 2nd solver (DUST) to continue with its steps. While the 1st solver (motion solver) has been performing

its steps, the 2nd solver (DUST) has been waiting for the initial data from preCICE to set up its mesh. Once the 2nd adapter receives the signal to continue, it reads the data from the coupling nodes and DUST sets up the mesh. Initially, it assumed a random position of the nodes and now calculates the forces and moments by assuming the model has changed its position from the random assigned position to the position provided by the motion solver. This is obviously an additional time step (with incorrect results) but is necessary for preCICE to make sure the working orders of the two solvers (+ adapters) are maintained. Hence, this 1st time step is considered as the 0th iteration by DUST as it is only required for the initial placement of the model in the flowfield.

These values are now sent back to preCICE and now preCICE checks again which solver has called the '$Advance()$' function. When it is the 2nd solver, an additional step occurs where convergence is checked. For this step, there exists pre-defined criteria to determine whether the solution from DUST has converged or else the time step is repeated. Since the first iteration assumed an initial position, chances of convergence are slim to none. If convergence has not been achieved, an accelerating scheme is applied to the same input provided by the other solver and DUST re-runs the same time step [32]. This keeps occurring until the convergence criteria is satisfied and once it has been reached, the forces and moments from the final iteration of the current time step are sent to the other solver. The pre-defined convergence condition is checked for the data provided by the 2nd solver namely $Forces$ and $Moments$.

Before either of the solvers call the '$Advance()$' function and before preCICE sends the message to the 1st solver, each one of the solvers and preCICE check whether their respective total time steps have been completed. Each one of them is given a simulation ending time (which are typically identical). If either of their final time steps has been reached, the simulation is stopped immediately. Typically, all the time steps provided to the solvers and preCICE are the same.

If the final time step of either of the solvers or preCICE has not been reached, the message is now sent to the 1st solver to begin the current/next time step. The steps are now repeated starting with reading the data for the current time step from the coupling nodes.

As of the time of writing this thesis, there are several adapters available that can link to DUST using preCICE, notably OpenFOAM, FEniCS, CalculiX and a couple others [31]. All these solvers are either high-fidelity CFD solvers or mid-fidelity pure structural or pure thermal solvers. There are currently no solvers that allow for both user-defined motions to models, i.e. Fluid-Motion Interactions (FMI) (for studying the aerodynamic response of the models to said motions) and use minimal resources such as computing time, computing power, etc. This creates an opportunity to develop a new solver which can be used to provide user-defined motions to models provided by the user.

3.3 Introduction to the Aerodynamic Solver: DUST

DUST is a mid-fidelity aerodynamic solver developed by A^3 by Airbus and the Department of Aerospace Science and Technology of Politecnico di Milano [30, 33]. DUST was developed based on incompressible flow theory, but compressibility effects can be considered for steady aerodynamic loads on surfaces by applying a Prandtl-Glauert correction for surface panels and vortex lattice elements, while using Mach-dependent tabulated data for lifting line elements. The inputs to the solver are:

a) the geometry and the mesh of each component,
b) the reference frames and
c) the simulation conditions and the solver parameters.

The solver evolves the simulation in time for the prescribed number of steps and writes the solution to a set of files or displayed on the screen as specified by the user. The general workflow for a simple DUST simulation is shown in Figure 3-4. The pre-processor allows the user to import components from pre-existing mesh files. Alternatively, the user can generate components parametrically by specifying the geometry in the input files. Different aerodynamic models ranging from the one-dimensional lifting lines and actuator disks to zero-thickness lifting surfaces and three-dimensional surface panels, are implemented and available in DUST. Although the mathematical formulation of the solver is limited to rigid bodies and does not allow to simulate flexible components, this is overcome by coupling the outputs from each time step to another solver using a coupling library such as preCICE.

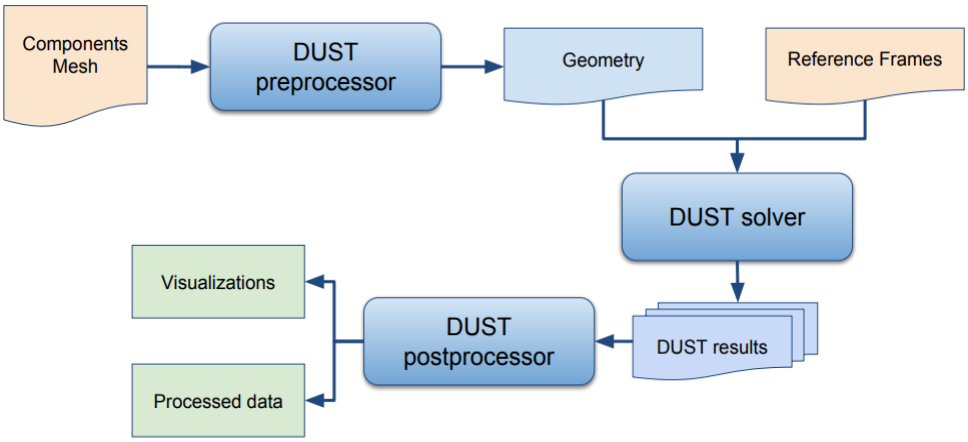

Figure 3-4: DUST workflow [33]

In all the simulations performed during this thesis, surface panel elements (SP) were used for the wing models and lifting line elements (LL) were used for the propeller models. No external meshes were used besides a simple DAT-file containing the surface points for an airfoil. For the simulation settings, only the default settings provided in DUST were used as there was no requirement to change those settings. The only settings that were varied were the mandatory

user-defined settings such as starting time (t_{start}), ending time (t_{end}), air density (ρ_∞) and freestream velocity (u_∞). There is no need for the usage of the reference frames option provided by DUST when it is coupled with another solver. The in-house motion solver has built-in functions to create the reference frames as it is the solver involved in calculating the nodal positions and velocities (this will be explained in chapter 3.4.2).
DUST has a comprehensive set of post-processing tools that provide integral loads, sectional loads, chordwise loads and numerous visualisations. Only the DUST post-processing tools were used for the results generated in this thesis.

3.4 Introduction to the Motion Solver

The in-house motion solver was created primarily to send pre-calculated values of a model's node positions and velocities based on user-defined motions to an aerodynamic solver. An additional function is that it can also be used as a regular structural solver by solving an MDoF motion system, but this function will not be discussed in this thesis. The in-house motion solver overcomes a drawback of other structural solvers in the fact that it can be used to simulate pre-defined motions while maintaining low computational time and resource usage. The motion solver contains a library of functions, each fulfilling a different requirement or set of requirements for the simulation and is coupled to DUST using the preCICE-MATLAB adapter (see Figure 3-3).
The general workflow of structural solvers involves using user-defined mass, stiffness and damping matrices and forces and moments as inputs to solve a set of motion equations. This limits the user from being able to set pre-defined motions to their models and obtain an output for the response to these pre-defined motions. When using DUST uncoupled, it is possible to set pre-defined motions using a file with all the reference frames and their motions. But even these are limited to simple motions such as constant, linear, and harmonic variations in translational and rotational motions. While these pre-defined motions are sufficient to perform the most basic of simulations, they do not provide the user with sufficient flexibility to perform complex or time-dependent motion response simulations.
The in-house motion solver contains various functions that can be run individually such as '$set\_reference\_frames()$', '$set\_motion\_table()$' and '$set\_prescribed\_val()$' that can be used to create parent-child reference frames with each frame defined by an orientation and a set of nodes with their positions, assign simple or complex, time-independent or time-dependent motions to these reference frames and calculate the positions and velocities of each degree-of-freedom (DoF) for each node in the simulation. The advantages of using the in-house motion solver's prescribed motion simulations are:

1. Ability to assign a pre-defined motion to any given model using just a set of coupling nodes and calculate its time-domain response.
2. The user receives more flexibility in their choice of motion definition.
3. Single file used for each simulation (unlike DUST which requires multiple input files).
4. Both the reference frames and user-defined motions are each stored in a single MATLAB table, providing the user with concise information and easy access.
5. Prescribed positions and velocities can be obtained and validated before beginning the coupling with the aerodynamic solver.

The in-house motion solver saves the simulation information including reference frames and prescribed motions in an object at a user-defined location. An example of an object created by the motion solver in MATLAB is shown in Figure 3-5.

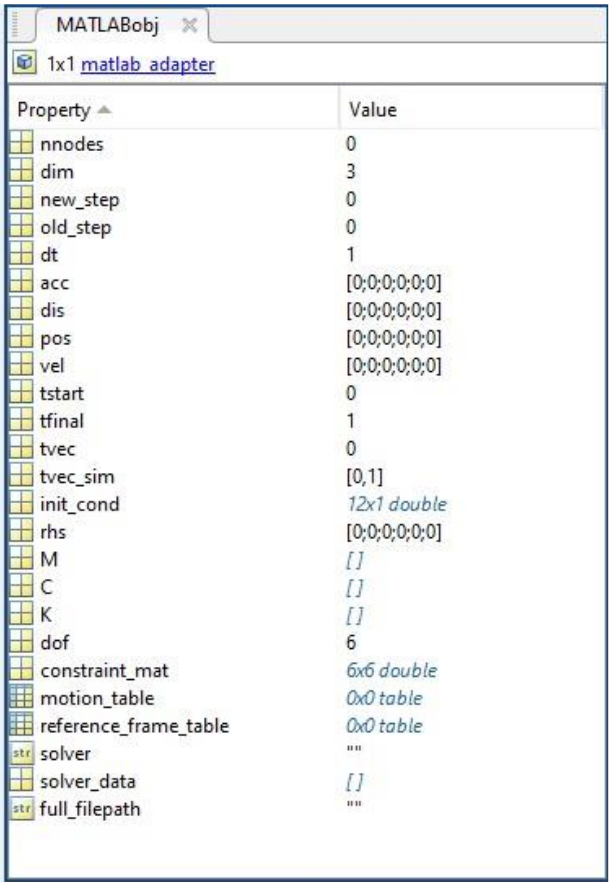

Figure 3-5: Motion solver object

3.4.1 Workflow for a Prescribed Motion Simulation

In chapter 3.2.1, the workflow for the entire coupling was explained with little detail on the actual workings of the motion solver. In this chapter, the focus will be on the workflow of the (in-house) motion solver for a prescribed motion simulation, provided in Figure 3-6.

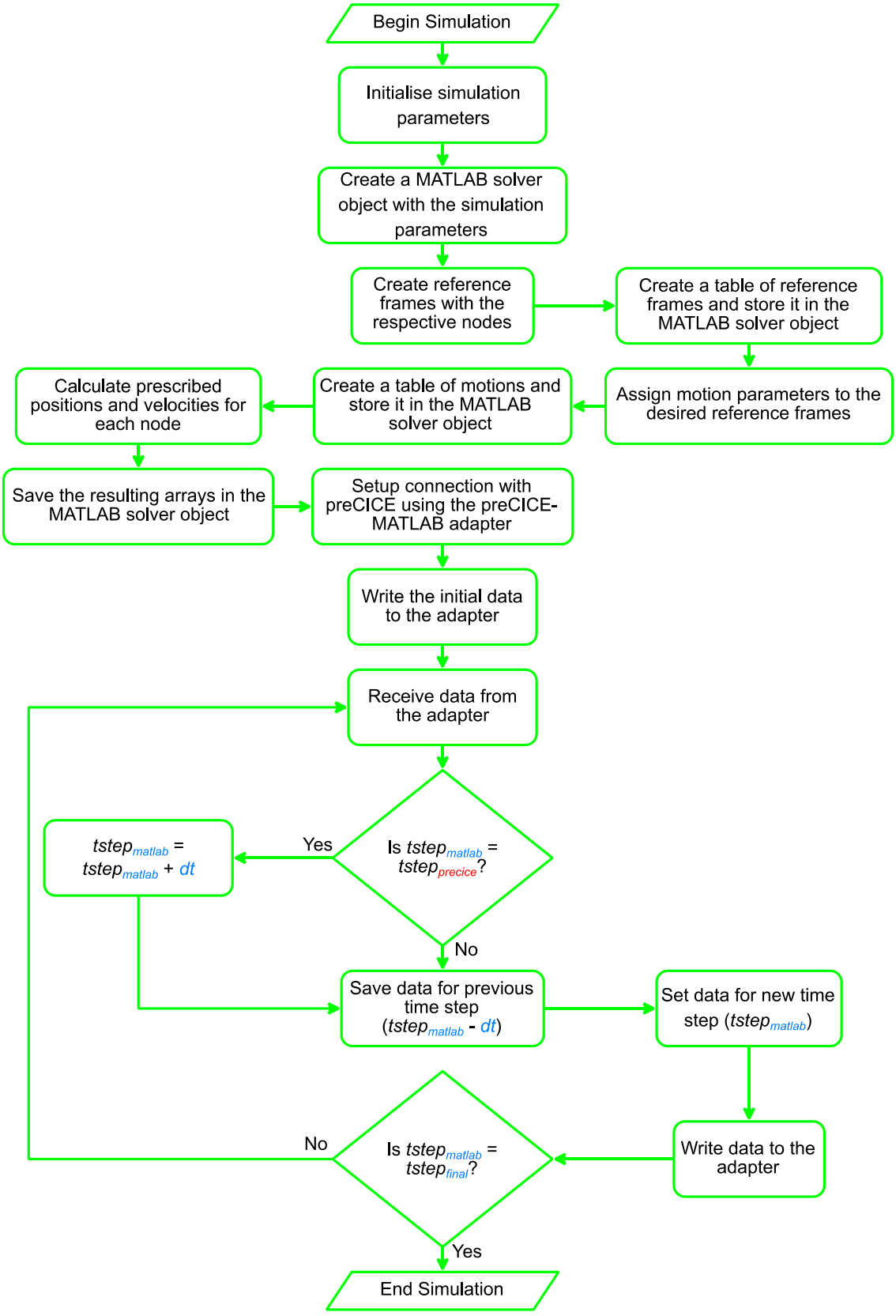

Figure 3-6: Workflow of the motion solver – Prescribed motion simulation

In the MATLAB file used to run the prescribed motion simulation, the simulation parameters are first initialised by saving this data into a structure, which is saved into the motion solver object during its creation. This object will contain all the data regarding the simulation parameters, reference frames, user-defined motion data, prescribed positions and velocities calculated for each node and the output (forces) returned by the preCICE-MATLAB adapter. Once the prescribed values for each node have been calculated and stored in the object, the coupling with preCICE and DUST is initiated. This is done by reading the port number of the socket created during initialization of the preCICE-MATLAB adapter which is saved in a text file. Using this port number, a client connection is set up while the adapter acts as a server. Since DUST requires a step to initialise its mesh, the prescribed data from the 1st time step is initially sent. The initial positions for each node may vary but the velocities in all DoFs for all nodes are 0. The next step does not involve the solver, but the solver waits for the adapter to send the current data to DUST, receive the updated data from DUST and send the data back to the solver. Once the solver receives this data, it moves on to the next step.

The data received from the adapter is a 1-dimensional array of size $[(12 * n * d + 1) \times 1\ ]$ where n is the number of nodes, d is the dimensions of the simulation (2 for 2-D and 3 for 3-D) with the last element of the array being the current time step of preCICE and DUST (dt). In this step, the motion solver checks whether the time step provided by preCICE is the current time step or the next one. For a prescribed motion simulation, the convergence criteria are defined such that every iteration always satisfies convergence as the desired values of positions and velocities are already known. These values are directly fed to the DUST solver, hence there is no expected deviation and therefore no convergence requirement, but it is a mandatory requirement of preCICE to set convergence criteria and hence these criteria are set at extremely high values to ensure convergence satisfaction irrespective of the values provided. This means that every time step in a prescribed motion simulation runs for just one iteration. Therefore, the time step sent back by preCICE is always the next time step. The MATLAB solver now increases its time step and runs two steps:

1) It saves the values of forces for each node DoF for the previous time step ($tstep_{matlab} - dt$; $tstep_{matlab}$ is the time-step defined by the user in the motion solver) as a 1-dimensional array in the solver object provided by preCICE through the adapter.
2) It appends two 1-dimensional arrays – one for the positions and velocities of each node DoF for the current time step ($tstep_{matlab}$) which are the prescribed values calculated before the coupling and the input array containing forces of each node DoF ($tstep_{matlab} - dt$). This acts as the output array that is sent to the adapter.

Before it waits for the input from the adapter for the next time step to begin the loop, it checks whether the final time step provided by the user in the motion solver file ($tstep_{final}$) has been reached, i.e. $tstep_{matlab} = tstep_{final}$. If it has been reached, it terminates the program. To ensure that the simulation is terminated even after DUST and preCICE have reached their final time step and have been terminated, a safety check has also been defined: a user-defined minimum idle time (t_{idle}) is provided to the prescribed motion function which is used while the solver is waiting for a response from the adapter. If in any time step the waiting/idle time of the solver (while it is waiting for a response from the adapter) crosses the user-defined minimum idle time, the simulation is automatically terminated.
For all the simulations performed during this thesis, the maximum time taken for calculation of prescribed values has not exceeded 1 minute and the time taken by the solver and adapter between receiving the data from preCICE to sending the data to preCICE (for one time step iteration) has not been more than 0.2 seconds. These operation times can be considered as extremely fast and display the efficiency of the motion solver.

3.4.2 Reference Frame Definition for Prescribed Motions

A model can be defined in the motion solver for a prescribed motion simulation using a system of reference frames that each contain a set of points. The points defined in all the reference frames together make up the coupling nodes used by preCICE (and DUST). The reference frames are connected to each other using a parent-child hierarchy system. Each reference frame is saved as a MATLAB structure and all these structures are sent to another function that assigns default values to inputs not provided by the user and places them in a MATLAB table in the order of their parent-child hierarchy.
An example of parent-child hierarchy for a wing with two propellers is shown in Figure 3-7. The first level of reference frames in the global default reference frame used by the motion solver. The default reference frame used by the motion solver is depicted in Figure 3-8. As shown in the figure, the solver uses a right-hand co-ordinate system with the X-axis being in the direction of freestream velocity, Y-axis being in the spanwise direction and Z-axis being in the vertical direction such that for any wing, it moves from pressure side to suction side. This reference frame is depicted in the solver as *'0'*. All subsequent reference frames use this reference frame as the basis reference frame since this is the standard frame and will not change under any circumstance.

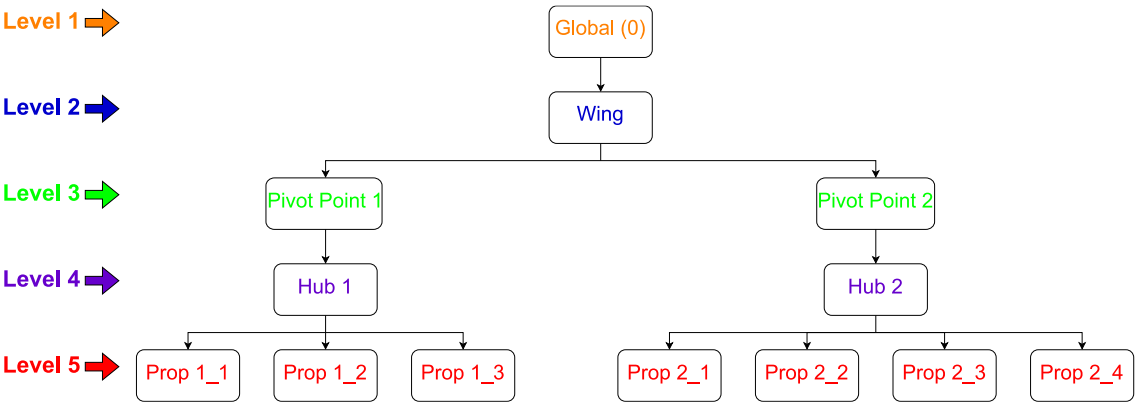

Figure 3-7: Example of parent-child hierarchy for a wing with two propellers

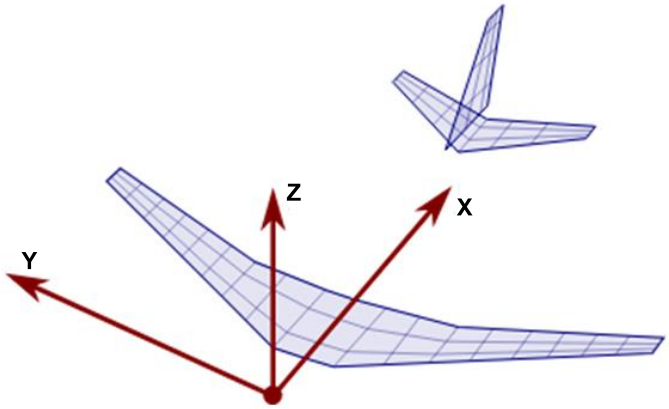

Figure 3-8: Motion solver global co-ordinate system [34, 35]

The next reference frame is the *'Wing'* reference frame. This is considered as the "child" reference frame of the global ('0') reference frame and the global reference frame is considered as the "parent" reference frame of the *'Wing'* reference frame. In the motion solver, each child reference frame is defined w.r.t the parent reference frame. This means that the various positional definitions of the child reference frame such as origin and orientation are all defined with respect to the parent reference frame's origin and orientation. This choice was made while developing the motion solver to avoid ambiguity during reference frame definition and unnecessary difficulties for more complex systems of reference frames. Figure 3-9 shows all parent-child trees generated for the example provided.

The next level of reference frames contains *'Pivot Point 1'* and *'Pivot Point 2'*. Both are the child reference frames of the *'Wing'* parent reference frame. Common logic dictates that a parent reference frame can have multiple child reference frames but not vice-versa. Having multiple parent reference frames would bring up numerous conflicts when motions are defined to one or more than one parent reference frames. Hence it can be clearly in Figure 3-9 that each reference frame has either a single, multiple or zero child reference frame but has just one parent reference frame.

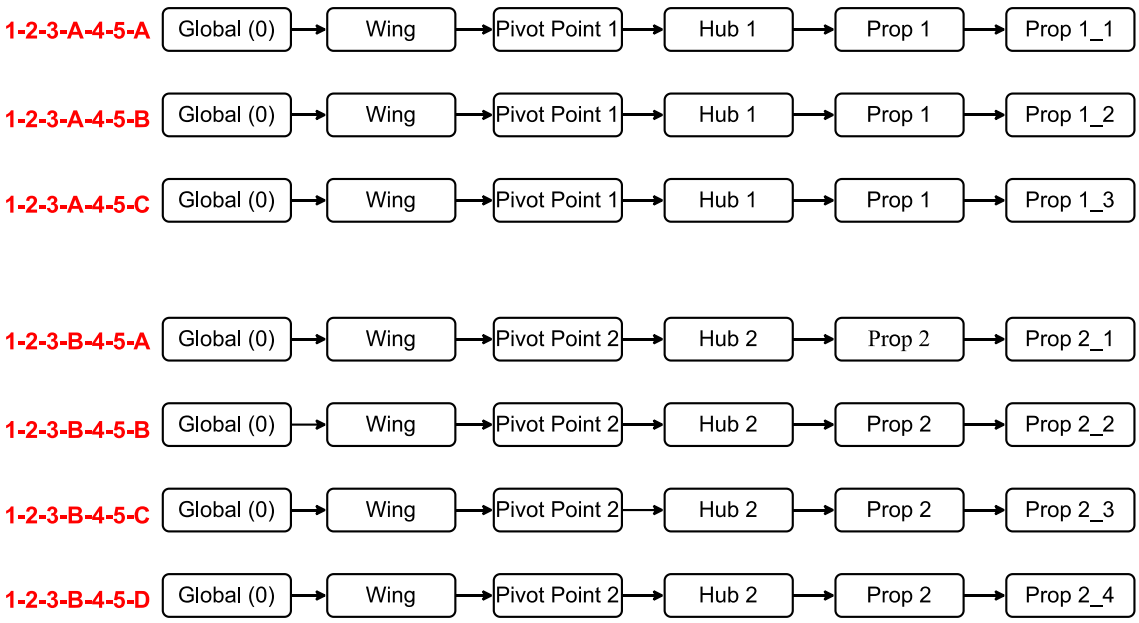

Figure 3-9: Formation of parent-child trees in example depicted in Figure 3-7

The *'Pivot Point 1'* reference frame has one child reference frame called *'Hub 1'*, and the *'Pivot Point 2'* reference frame also has one child reference frame called *'Hub 2'*. Although they are at the same "level" of reference frames, they belong to separate parent-child "trees." Again, common logic dictates that no child reference frame can belong to a different parent-child tree as each reference frame can have only one parent reference frame which would create problems during definition of node positions. More importantly, any reference frame being a part of two different parent-child trees would cause conflicts when one or more trees had any reference frame in a higher level subject to any motion. In the example shown in Figure 3-7, all the reference frames in the first 3 levels, i.e. the *'0'*, *'Wing'*, *'Pivot Point 1'* and *'Pivot Point 2'* reference frames (1-2-3) are initially considered as one parent-child tree. A problem arises when the reference frames from level 4, i.e. *'Hub 1'* and *'Hub 2'* need to be added to a parent tree, as this will create conflicts if they are both defined as part of a single big tree. A motion defined for a reference frame in one level of a parent-child tree is dependent on the motions defined for the reference frames at higher levels in the same tree. Here, if a motion for the *'Pivot Point 1'* reference frame is defined, a relative motion of the reference frame *'Hub 1'* and its child reference frames can be expected, but not for the *'Hub 2'* reference frame as *'Hub 2'* is dependent on any motion defined for *'Pivot Point 2'* (and reference frames in higher levels of its tree, i.e. *'Wing'*). To avoid this conflict, an assumption is made that when any reference frame has more than one child reference frame, each child reference frame (with their parent reference frame and the parent reference frame's parent reference frame and so on) is recognised as an individual tree for subsequent child reference frames. In the example chosen, not only will *'0'*, *'Wing'*, *'Pivot Point 1'*

and *'Pivot Point 2'* be considered as one parent-child tree (1-2-3) but also be recognised as two individual parent-child trees, i.e. *'0'*, *'Wing'* and *'Pivot Point 1'* (1-2-3-A) and *'0'*, *'Wing'* and *'Pivot Point 2'* (1-2-3-B) and the two level 4 reference frames *'Hub 1'* (1-2-3-A-4) and *'Hub 2'* (1-2-3-B-4) are each added to their respective individual trees.

The *'Hub 1'* and *'Hub 2'* reference frames are parent reference frames to two propeller reference frames with 3 and 4 blades, respectively. Each blade is considered to have its own reference frame. Definition of a reference frame for each blade is time-consuming and is often complex. To simplify this process, any rotational reference frame with multiple parts (Ex. Propellers) are defined using a single "pseudo-parent" reference frame. In this reference frame, a fixed reference frame name (default: *'Prop'* + propeller number) is provided along with a flag variable 'is_prop' and another numerical variable 'num_blades'.

The 'is_prop' flag is used by the motion solver to use a different protocol while creating the reference frame. If the 'is_prop' variable is True, the motion solver takes the 'num_blades' variable to determine the number of additional reference frames to be created. It then creates the additional reference frames, each with a unique name: pseudo-parent reference frame's $reference\ tag + 'blade\ number'$. Each one of these reference frames are uniformly distributed around the pseudo-parent reference frame's origin, i.e. each blade reference frame has the same origin but a different orientation such that the 1st blade reference frame's orientation is assigned with its Z-axis being in the opposite direction of the X-axis of the pseudo-parent reference frame's orientation and its Y-axis being in the opposite direction of the pseudo-parent reference frame's Z-axis. The subsequent blades are rotated by $[(n-1)*(360/num\_blades)]°$ in the pseudo-parent reference frame's X-axis (or the 1st blade's Z-axis) where n is the blade number. For the propeller connected to *'Hub 2'*, i.e. *'Prop 2'*, the reference frames of the blades are:

Prop 2:

$$
\begin{aligned}
is\_prop &= TRUE \\
num\_blades &= 4 \\
reference\_tag &= \text{'}Prop\ 2\text{'} \\
origin &= [x, y, z] \\
orientation &= R
\end{aligned}
$$

Blade 1:

$$
\begin{aligned}
reference\_tag &= \text{'}Prop\ 2\_1\text{'} \\
origin &= [x, y, z] \\
orientation &= R \times R_{Rot} \times R_1
\end{aligned}
$$

Blade 2:

$$reference\_tag = \text{'}Prop\ 2\_2\text{'}$$
$$origin = [x, y, z]$$
$$orientation = R \times R_{Rot} \times R_2$$

Blade 3:

$$reference\_tag = \text{'}Prop\ 2\_3\text{'}$$
$$origin = [x, y, z]$$
$$orientation = R \times R_{Rot} \times R_3$$

Blade 4:

$$reference\_tag = \text{'}Prop\ 2\_4\text{'}$$
$$origin = [x, y, z]$$
$$orientation = R \times R_{Rot} \times R_4$$

All blades of the propeller *'Prop 2'* have the same origin while the orientation is varied by using a rotation matrix unique to each blade:

$$R = \begin{bmatrix} r_{11} & r_{12} & r_{13} \\ r_{21} & r_{22} & r_{23} \\ r_{31} & r_{32} & r_{33} \end{bmatrix}$$ (3 x 3 orientation matrix of 'Prop 1' w.r.t 'Hub 1')

$$R_{Rot} = \begin{bmatrix} 0 & 0 & 1 \\ -1 & 0 & 0 \\ 0 & -1 & 0 \end{bmatrix}$$ (3 x 3 rotation matrix used to rotate the blades from propeller reference frame's orientation to the desired 1st blade's orientation; constant matrix)

$$R_1 = \begin{bmatrix} 1 & 0 & 0 \\ 0 & 1 & 0 \\ 0 & 0 & 1 \end{bmatrix}$$ (3 x 3 rotation matrix used to rotate 1st blade; identity matrix (I) for 1st blade)

$$R_2 = \begin{bmatrix} 0 & -1 & 0 \\ 1 & 0 & 0 \\ 0 & 0 & 1 \end{bmatrix}$$ (3 x 3 rotation matrix used to rotate 2nd blade; $R_1 \times Z_{axis}\ rotation\ [= (2-1) * (360/4) = 90°]$)

$$R_3 = \begin{bmatrix} -1 & 0 & 0 \\ 0 & -1 & 0 \\ 0 & 0 & 1 \end{bmatrix}$$ (3 x 3 rotation matrix used to rotate 3rd blade; $R_1 \times Z_{axis}\ rotation\ [= (3-1) * (360/4) = 180°]$)

$$R_4 = \begin{bmatrix} 0 & 1 & 0 \\ -1 & 0 & 0 \\ 0 & 0 & 1 \end{bmatrix}$$ (3 x 3 rotation matrix used to rotate 4th blade; $R_1 \times Z_{axis}\ rotation\ [= (4-1) * (360/4) = 270°]$)

The parent-child trees used by the motion solver were designed in such a way that there will be no conflicts while assigning motions to the reference frames as well as calculating time-dependent positions and velocities of nodes of any child reference frame.

An additional feature of the motion solver while defining reference frames is the ability to use nodes as parent reference frames. In these cases, a node already defined in a previous reference frame can be used as the parent reference frame and calculate the origin with respect to the position of this node. In the above example, the *'Pivot Point 1'* and *'Pivot Point 2'* reference frames can have nodes defined in the *'Wing'* reference frame as parents. All nodes in a reference frame are considered to have the same orientation as the reference frame's orientation. Hence, the orientation of reference frames with a node as a parent are calculated with respect to the orientation of the reference frame in which the parent node is defined. This feature is very helpful as it reduces the number of reference frames to be defined by the user as well as allows for simulations where nodes in a single reference frame are not fixed with respect to one another or the reference frame itself (Ex. Wing deformations due to aerodynamic, structural or inertial forces). In addition to the user inputs for origin and orientations for each reference frame, the motion solver also calculates the origin and orientation of all reference frames with respect to the default reference frame ($origin_{global}$ and $orientation_{global}$ respectively). This can be helpful to the user for further verification.

3.4.3 Prescribed Motion Functions in the Motion Solver

As mentioned before, one of the advantages of the motion solver is the flexibility for users to assign motions to their desired models. Each motion is defined for a single reference frame and the user must provide the motion mode, motion type, motion axis (axis of the current reference frame to which the motion is applied), starting time and ending time for the given motion. Based on the motion modes and types, additional inputs need to be provided. Multiple motions can be defined to a single reference frame, but the order of assignment will be based on the order of definition by the user.

There are multiple types of prescribed motions that can be defined using the solver:

1. **Constant** Motion: Fixed amplitude motions (with an optional decay rate). This is one of the basic motions defined using equations 3.1 and 3.2. Here, A is the fixed amplitude and λ is the decay rate.

$$x(t) = \lambda A t \tag{3.1}$$

$$\dot{x}(t) = \lambda A \tag{3.2}$$

2. **Harmonic** Motion: Oscillating amplitude motions (with an optional decay rate). This is another basic motion defined using equations 3.3 and 3.4. Here, A is the fixed amplitude, B is the fixed initial offset, ω is the circular frequency, φ is the initial phase offset and λ is the decay rate.

$$x(t) = \lambda(A\sin(\omega t + \varphi) + B) \quad 3.3$$

$$\dot{x}(t) = \lambda A\omega\cos(\omega t + \varphi) \quad 3.4$$

3. **Custom Function** Motion: User-defined function, $f(t)$, used by the motion solver to calculate the position and velocity for a single DoF as given in equations 3.5 and 3.6. This allows for complex motion implementation:

$$x(t) = f(t) \quad 3.5$$

$$\dot{x}(t) = \dot{f}(t) \quad 3.6$$

4. **User-Defined** Motion: User-defined values ($x(0), x(1), \cdots, x(tstep_{final})$), used by the motion solver as the position, displacement or velocity (also an input from the user) values for any single DoF or a reference frame ($origin$). This allows the user to directly enter the values for a reference frame and allows the motion solver to combine these motions with other motions currently available.

In addition to these motion types, these motions can be assigned to a certain set of DoFs. These are called motion modes. Each motion is defined as a combination of a motion type and a motion mode. The list of available motion modes in the motion solver are:

1. **Linear** Mode: The motion type defined by the user is applied only to the translatory DoFs for each node in the reference frame.
2. **Rotation** Mode: The motion type defined by the user is applied only to the rotatory DoFs for each node in the reference frame.
3. **Custom Function** Mode: Works like the ‘Custom Function’ motion type but is now applied to multiple DoFs. This allows for more complex motions defined by the user.
4. **User-Defined** Mode: Works like the ‘User-Defined’ motion type but is now an input from the user for multiple DoFs. This allows for the user to calculate the position or velocity values of some or all the nodes of a model and use these values as the input to the other solver, giving them added flexibility.
5. **Eigenmotion** Mode: A unique feature of the motion solver which allows the user to provide the eigenvalues, eigenvectors, and the sampling frequency for a set of nodes. This feature is not available for any of the structural solvers currently available and is one of the primary reasons for developing the motion solver.

4 Validation Studies with the Motion Solver

4.1 Simple Wing Motions

To validate simple prescribed motion simulations, such as wing pitch and wing plunge using the in-house motion solver, two simple rectangular planform wing models were chosen: The 1st model (*Veldhuis Wing*) had 3 different configurations: NACA 0004, NACA 64_2-a015 and NACA 0024 airfoil, with each configuration using a single airfoil for the complete wing, and the 2nd model (*Gopalan Wing*) used an SD 7003 airfoil. The *Veldhuis Wing* model was used to validate the aerodynamic performance of pitching and plunging wings by comparing the results with theoretical values obtained from Theodorsen's Unsteady Thin Airfoil Theory [10] (see chapter 4.1.1), while the *Gopalan Wing* model was used to compare results obtained from performing FMI simulations for pitching and plunging motions to the results obtained from Gopalan's thesis [7] (see chapter 4.1.2).

4.1.1 Validation Against Theoretical Values: *Veldhuis Wing*

4.1.1.1 Model Description

For the pitching and plunging motion validation studies performed on the *Veldhuis Wing*, three different configurations were chosen, where the airfoil for the entire wing was varied while the planform and simulation settings remained fixed. For subsequent simulations performed using the *Veldhuis Wing*, only the NACA 64_2-a015 was used. The main objective in varying the airfoil used was to compare the effects of varying airfoil thickness on the aerodynamic performance as Theodorsen's theory is valid for tow-dimensional thin airfoil [10]. The detailed descriptions of the Veldhuis Wing model for the validation studies are given in Table 4-1.

Table 4-1: *Veldhuis Wing* – Model description: Pitching and plunging motions validation study

Parameter	Value
Airfoil	NACA 0004, NACA 64_2-a015, NACA 0024
Planform	Rectangular
Wingspan (b_W, m)	1.28
Wing chord (c_W, m)	0.24
Wing sweep (θ_W, deg)	0
Wing twist (λ_W, deg)	0
Wing dihedral (γ_W, deg)	0

4.1.1.2 Simulation Settings

Veldhuis Wing was subjected to uniformly oscillating pitching and plunging motions. For the simple wing motions validation study, the various parameters that were varied were the maximum pitching/plunging amplitudes ($\alpha_{W_{Max}}, h$) and the reduced frequency (k). The pitching axis (x_{pitch}/c_W) was set at the quarter-chord point. The fixed and varying parameters and their ranges are provided in Table 4-2. In both the pitching and plunging motion validation studies, the pitching and plunging amplitudes as well as the reduced frequency range were kept small enough to capture the unsteady aerodynamic phenomenon while ensuring linear to mildly non-linear aerodynamic behaviour ($1° \leq \alpha_{W_{Max}} \leq 4°,\ 0.025 \leq h \leq 0.1,\ 0.05 \leq k \leq 1.005$).

Table 4-2: *Veldhuis Wing* (Standalone wing) – Simulation settings: Pitching and plunging motion validation studies

Parameter (Fixed)	Value
Freestream velocity (u_∞, ms^{-1})	50.0
Freestream density (ρ_∞, kgm^{-3})	1.2
Wing initial angle of attack (α_{W_0}, deg)	0
Pitching axis X location ($x_{pitch}/c_W\ , -$)	0.25
Wing phase offset (φ_W, deg)	0
Parameter (Varying)	**Range**
Wing pitch amplitude ($\alpha_{W_{Max}}, deg$)	1, 2, 4
Normalised plunge amplitude ($h, -$)	0.025, 0.05, 0.1
Reduced frequency ($k, -$)	0.101, …., 1.005

4.1.1.3 Results and Discussion

For a wing undergoing pitching and plunging motions, the C_L and C_M vs normalised time (t/τ) plots must have different phase shifts and amplitudes at different amp_{Max} and k, while the C_L and C_M vs pitching/plunging amplitude (amp; α_W, h_W) plots must depict the formation of hysteresis loops. To verify these results, FMI simulations have been performed using DUST and the motion solver, and the results for two sets of simulation cases: a) fixed amp_{Max}, varying k and b) fixed k, varying amp_{Max} , were plotted. The simulation parameters are provided in Table 4-2. These plots have been provided for the pitching cases in Appendix A and plunging cases in Appendix B, and the results are in complete agreement with the observations from other papers [7, 13–16, 36].

Next, FMI simulations were performed for the 3 different configurations of the *Veldhuis Wing*, for pitching and plunging motions at different amp_{Max} and k. The simulation parameters are provided in Table 4-2. The time histories of the lift and

moment forces (L and M respectively) were taken and the transfer functions (H_L and H_M respectively) were calculated (as shown in equation 2.22). The transfer functions for the different configurations were compared to the results obtained from Theodorsen's Unsteady Thin Airfoil Theory (provided in equations 2.17 and 2.18) to better understand the behaviour of the systems (see chapter 2.2.2).
The transfer functions can be visualised either in the complex plane (as seen in Figure 2-9) or represented in terms of their magnitude and phase. Both representations provide the same information, but the different visualizations can be helpful in different scenarios. In Figure 4-1 and Figure 4-2, the transfer functions for the 3 different configurations of the *Veldhuis Wing* and the theoretical transfer functions have been plotted in the complex plane. In Figure 4-3 and Figure 4-4, the magnitude and the phase of the same transfer functions were plotted against k. Figure 4-1 and Figure 4-3 are plots for the pitching motion cases, while Figure 4-2 and Figure 4-4 are plots for the plunging motion cases. Each line represents a fixed amp_{Max} and varying k and each marker represents a different amp_{Max}. The blue, orange and yellow lines and markers indicate the transfer functions of the NACA 0004, NACA 64$_2$-a015 and NACA 0024 airfoil configurations of the *Veldhuis Wing* respectively, while the purple lines and markers indicate the theoretical transfer functions.

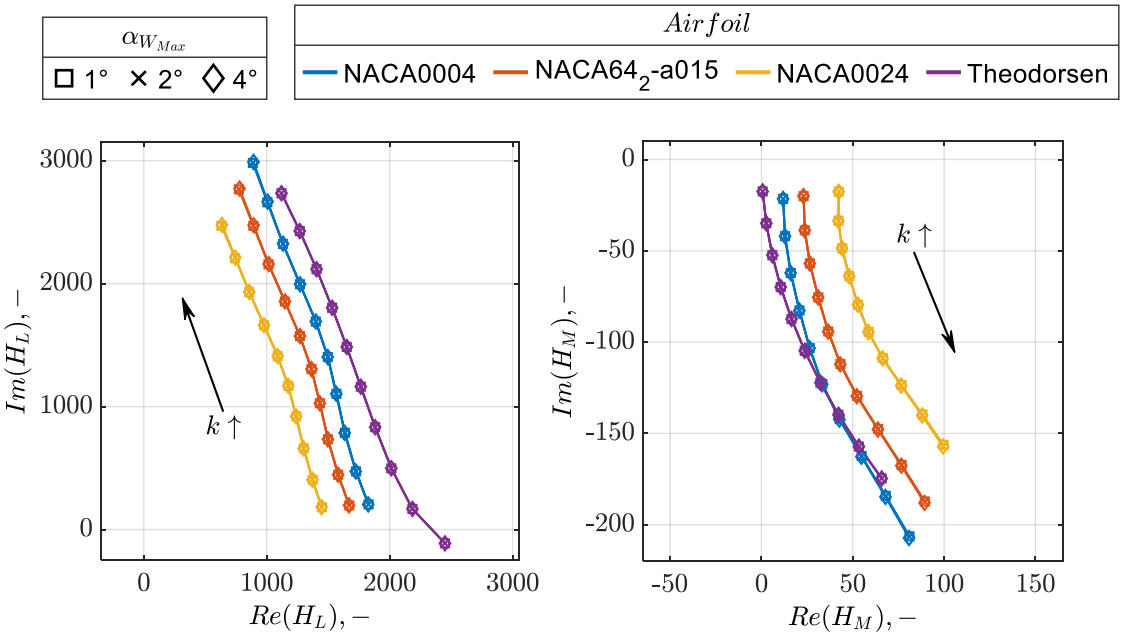

Figure 4-1: *Veldhuis Wing* (Standalone Wing, Pitching motion) – H_L, H_M: Complex plane representation

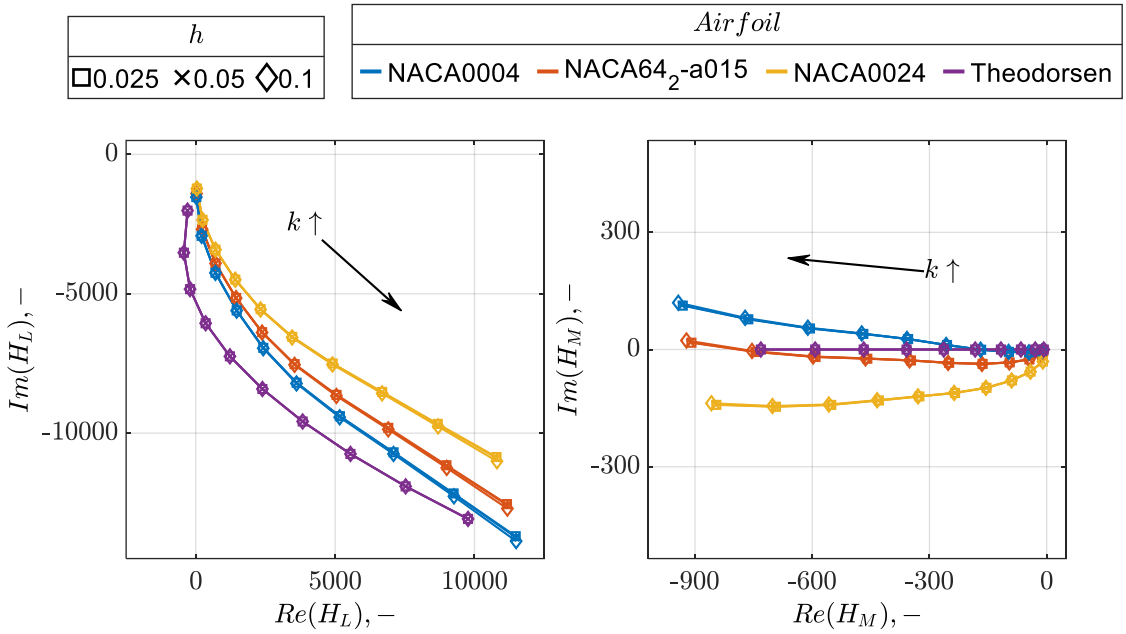

Figure 4-2: *Veldhuis Wing* (Standalone Wing, Plunging motion) – H_L, H_M: Complex plane representation

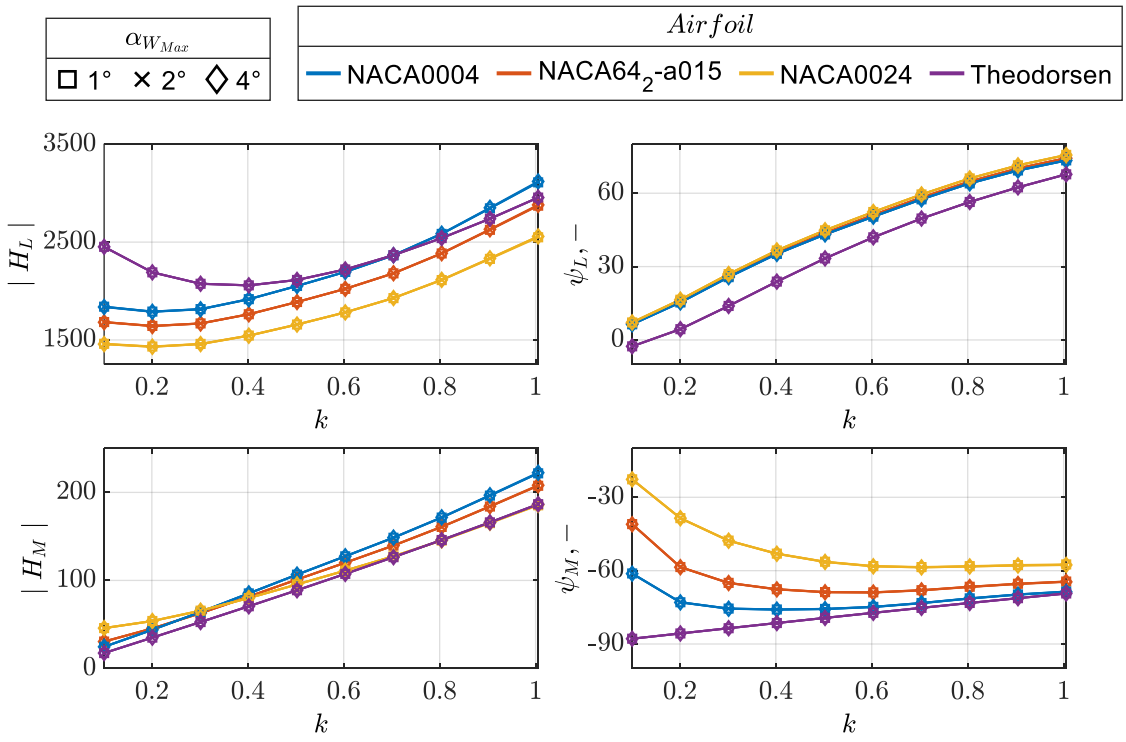

Figure 4-3: *Veldhuis Wing* (Standalone Wing, Pitching motion) – H_L, H_M: Magnitude and phase representation

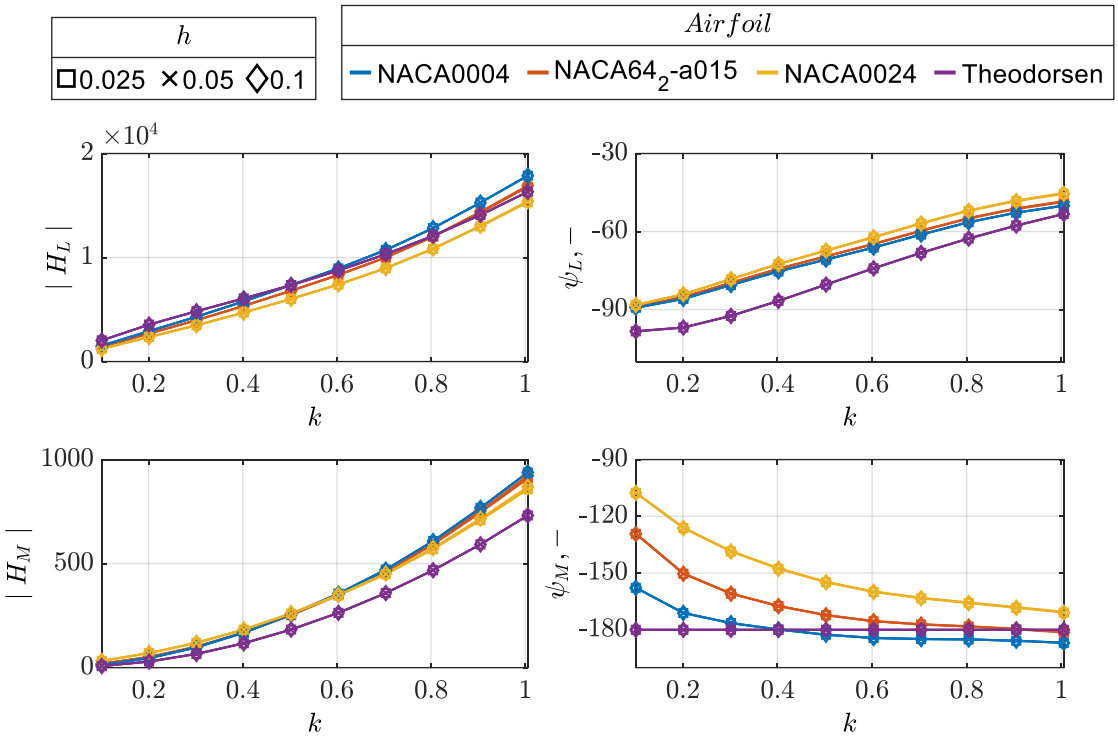

Figure 4-4: *Veldhuis Wing* (Standalone Wing, Plunging motion) – H_L, H_M: Magnitude and phase representation

In the complex plane representations as well as the magnitude and phase representations, the lines and markers of the same colour overlapped with little to no deviation, indicating that the behaviour of the system is independent of the magnitude of amp_{Max} (for small values of amp_{Max}). In the complex plane representations, the curves of the different airfoil configurations had similar trends with only a variation in magnitude. These curves deviated from the theoretical curves but did observe a slightly similar shape. An explanation for this deviation could be due to the 3-dimensional effects of the wing model. The deviation from the theoretical curves increased for an increase in airfoil thickness which is expected as the airfoil section shape deviates further from a flat plate shape. This could also be seen in the magnitude and phase representations. As expected, an increase in k led to an increase in the magnitudes of the lift and moment transfer functions as larger frequencies induce a larger vertical component of velocity on the wing, resulting in a larger increase in the lift and moment forces (see chapter 2.2.2). These results showed that the motion solver coupled with DUST can be used to perform simulations of pitching and plunging wings with high accuracy.

4.1.2 Validation Against Simulated Data: *Gopalan Wing*

4.1.2.1 Model Description

The SD 7003 Wing model (*Gopalan Wing*) was used to compare the aerodynamic performance of a wing undergoing pure-pitching and pure-plunging motions by

performing FMI simulations to the results obtained in Gopalan's thesis with the same simulation settings as provided in his thesis [7]. The detailed model description is given in Table 4-3. It must be noted that the simulations performed by Gopalan were on an airfoil. Hence, a random wing aspect ratio was assumed for the FMI simulation model. This would obviously give rise to variations in the results obtained, but the primary goal in this chapter was to capture the overall trends.

Table 4-3: *Gopalan Wing* – Model description: Pitching and plunging motion validation studies

Parameter	Value
Airfoil	SD 7003
Planform	Rectangular
Wingspan (b_W, m)	3.0
Wing chord (c_W, m)	1.0
Wing sweep (θ_W, deg)	0
Wing twist (λ_W, deg)	0
Wing dihedral (γ_W, deg)	0

4.1.2.2 Simulation Settings

The *Gopalan Wing* model was subjected to uniformly oscillating pitching and plunging motions. The freestream Mach number (Ma_∞) was fixed at 0.1. Here, the various parameters that were varied were the maximum pitching amplitude ($\alpha_{W_{Max}}$), normalised plunge amplitude (h), and the reduced frequency (k). The fixed and varying parameters and their ranges for pure pitching and pure plunging motions are provided in Table 4-4.

Table 4-4: *Gopalan Wing* – Simulation settings: Pitching and plunging motion validation studies

Parameter (Fixed)	Value
Wing initial angle of attack (α_{W_0}, deg)	0
Pitching axis X location ($x_{pitch}/c_W, -$)	0.25
Wing phase offset (φ_W, deg)	0
Freestream Mach number ($Ma_\infty, -$)	0.1
Freestream density (ρ_∞, kgm^{-3})	1.225
Parameter (Varying)	**Range**
Wing pitch amplitude ($\alpha_{W_{Max}}, deg$)	1.5, 3, 6, 12
Normalised plunge amplitude ($h, -$)	0.025, …., 0.1
Reduced frequency ($k, -$)	1.9625, 3.925, 7.85

4.1.2.3 Results and Discussion

C_L has been plotted against t/τ for the pitching motion and plunging motion cases in Figure 4-5:

a) with k fixed at 3.925 and varying $\alpha_{W_{Max}}$,

b) with both k and $\alpha_{W_{Max}}$ varying but constant $k\alpha_{W_{Max}}$,

c) with k fixed at 3.925 and varying h and

d) with both k and h varying but constant St.

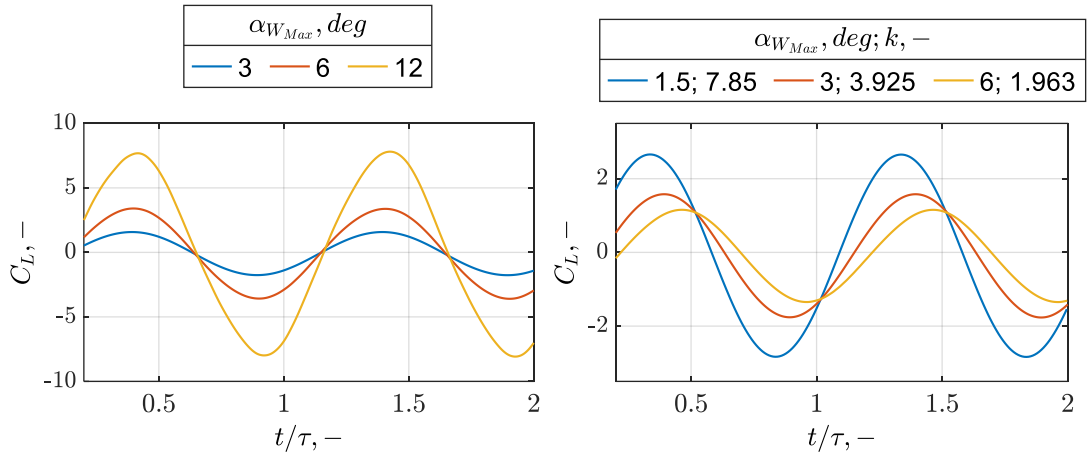

a. Pitching motion; *k* = 3.925 **b. Pitching motion; $k\alpha_{WMax}$ = 0.2055**

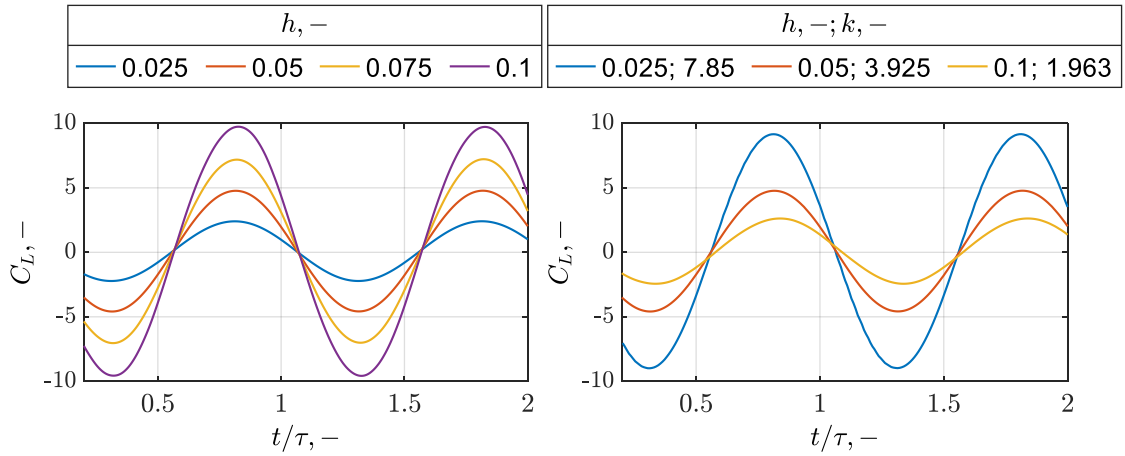

c. Plunging motion; *k* = 3.925 **d. Plunging motion; *St* = 0.125**

Figure 4-5: *Gopalan Wing* (Standalone Wing) – C_L vs t/τ

In Figure 6-5, it could be observed that for a fixed value of k, as $\alpha_{W_{Max}}$ and h increased, the maximum value of C_L also increased. It could also be observed that for a fixed value of $k\alpha_{W_{Max}}$ and St, the maximum value of C_L increased for an increase in k. These results were in complete agreement with the results obtained by Gopalan [7] and Baik and Rausch [37].

Additionally, in all cases a negative phase shift, i.e. a phase lag was observed. For the plunging motion cases, an upward plunging motion (positive velocity in Z-

axis) corresponded to negative values of C_L, resulting in larger phase lags. This was explained in Figure 2-7 where the upward plunging velocity of the wing induced a downwash, therefore creating negative lift force. Therefore, it could be concluded that the plunging motion of a wing lags the pitching motion (about the quarter chord point) for the same φ_W. For a fixed k, as the pitching/plunging amplitudes increased, the phase shift decreased. This phase shift was most likely due to the large pitching/plunging amplitudes and reduced frequency chosen, resulting in non-linear effects. For a fixed $k\alpha_{W_{Max}}$ and St, the phase shift variation was much larger (especially in the pitching motion cases due to the exceptionally large pitching amplitudes chosen). As the pitching/plunging amplitudes increased, the phase shift decreased.

In both pitching and plunging cases, similar patterns were observed for constant k and constant $k\alpha_{W_{Max}}/St$ cases (negative phase shift (phase lag), decrease in phase shift for increasing pitching/plunging amplitudes and increasing $C_{L_{Max}}$ for increasing k). To compare the two motions, a pure pitching case ($k = 3.925$ and $\alpha_{W_{Max}} = 6°$) with $\varphi_W = 180°$ (upwards pitching motion about the quarter-chord point generates positive lift whereas upwards plunging motion generates negative lift, hence pitching motion leads plunging motion by 180°) was chosen and compared to a set of pure plunging cases for the same k. The C_L for these cases has been plotted against t/τ in Figure 4-6.

It could be observed that the equivalent plunging amplitude for the chosen pitching case is approximately 0.038. This is slightly different as compared to the result obtained by Gopalan [14] where he observed an equivalent plunging amplitude of 0.034, with this difference most likely due to 3-dimensional effects.

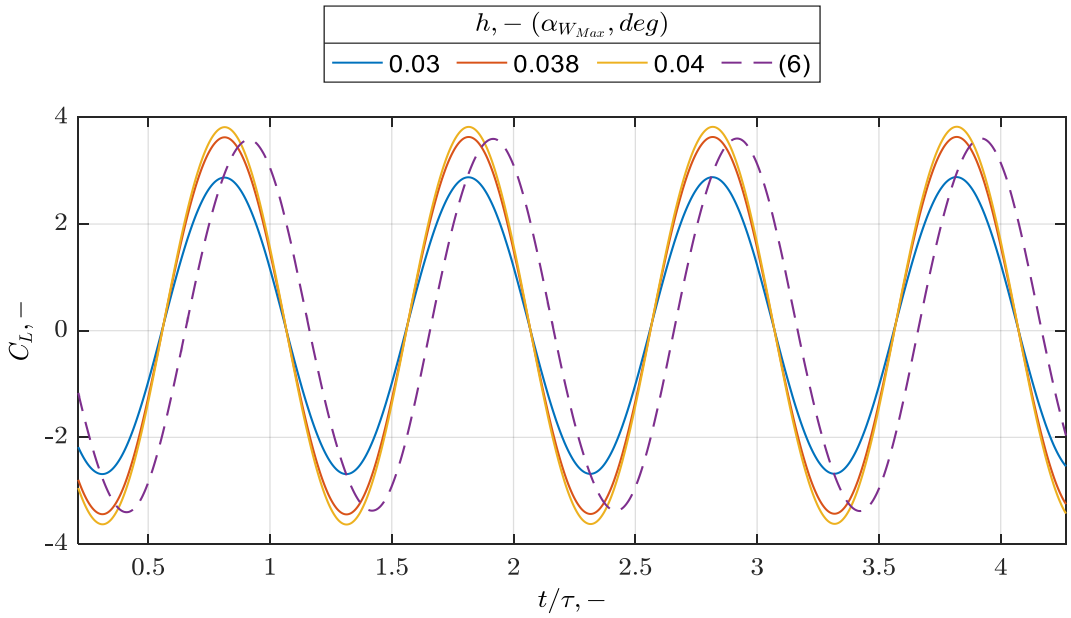

Figure 4-6: *Gopalan Wing* (Standalone wing) – C_L vs t/τ to compare pitching and plunging motions; k = 3.925

4.2 Complex Wing Modes

4.2.1 Model Description

The *Goland wing* is a benchmark wing model used in aeroelastic studies for flutter calculations [38]. Hence, there is a lot of information available regarding the mode shapes and the natural frequencies of the *Goland wing* and therefore was used in the wing mode shape validation studies.

The *Goland wing* model was used to validate the "eigenmotion" (e) motion type function in the motion solver. The eigenvalues and eigenvectors were calculated and used as the input to the MATLAB solver. Description of the *Goland wing* model used is shown in Table 4-5.

Table 4-5: *Goland Wing* (Standalone Wing) – Model description [38]*: Motion solver validation study

Parameter	Value
Wingspan (b_W, m)	6.096
Wing chord (c_W, m)	1.8288
Torsional stiffness (GJ, Nm^2)	9.88 * 10^5
Y-axis bending stiffness (EI_y, Nm^2)	9.77 * 10^7
X-axis bending stiffness (EI_z, Nm^2)	9.77 * 10^6
Centre of gravity offset ($cg_z, \%c_W$)	0.2
Aeroelastic axis Z location ($ea_z, \%b_W$)	0.33
Mass per unit length ($m/L\,, kgm^{-1}$)	35.72

Here, GJ is the torsional stiffness, EI_y is the bending stiffness about the Y-axis, EI_z is the bending stiffness about the Z-axis, cg_z is the offset of the centre of gravity in percent of c_W, ea_z is the non-dimensional distance of the aeroelastic axis in percent of b_W and m/L is the mass per unit length. These values were solely used to create the mass, stiffness and damping matrices used in calculating the eigenvalues and eigenvectors of the *Goland Wing* model. These calculations were done by another in-house tool and lies outside the scope of this thesis. Only the wingspan (b_W) and wing chord (c_W) were subsequently used in the FMI simulations performed on the model.

* The coordinate system used for representing the Goland wing is as follows:
X-axis: Runs along the wing's span, from the root towards the wingtip.
Y-axis: Points upward, perpendicular to the wing's surface.
Z-axis: Runs along the chord of the wing, from the leading edge towards the trailing edge.
The values provided in Table 4-5 are in the general Goland wing coordinate system. The Goland wing coordinate system was only used by the in-house tool and not for subsequent FMI simulations.

4.2.2 Results and Discussion

The first 4 mode shapes were considered, and the resulting natural frequencies (f_{Nat}) were obtained and are shown in Table 4-6. All the frequencies were calculated using an in-house tool that uses MATLAB's '$polyeig$' and '$eigs$' functions. These values are in close agreement with the results obtained in multiple papers [30, 39, 40].

Using the same in-house tool, visualizations for the wing mode shapes were created and depicted in Figure 4-7, along with the co-ordinate axis used by the motion solver (X-axis: Red, Y-axis: Green, Z-axis: Blue).

Table 4-6: *Goland Wing* – First 4 natural mode frequencies

Mode Shape	Durmuş [39]	Bennamia and Baderredine [40]	Savino and Cocco [30]	Current Model
1	49.58	49.24	48.13	**48.07**
2	97.28	99.19	95.57	**95.56**
3	248.58	246.53	242.15	**242.69**
4	356.32	-	344.26	**344.91**

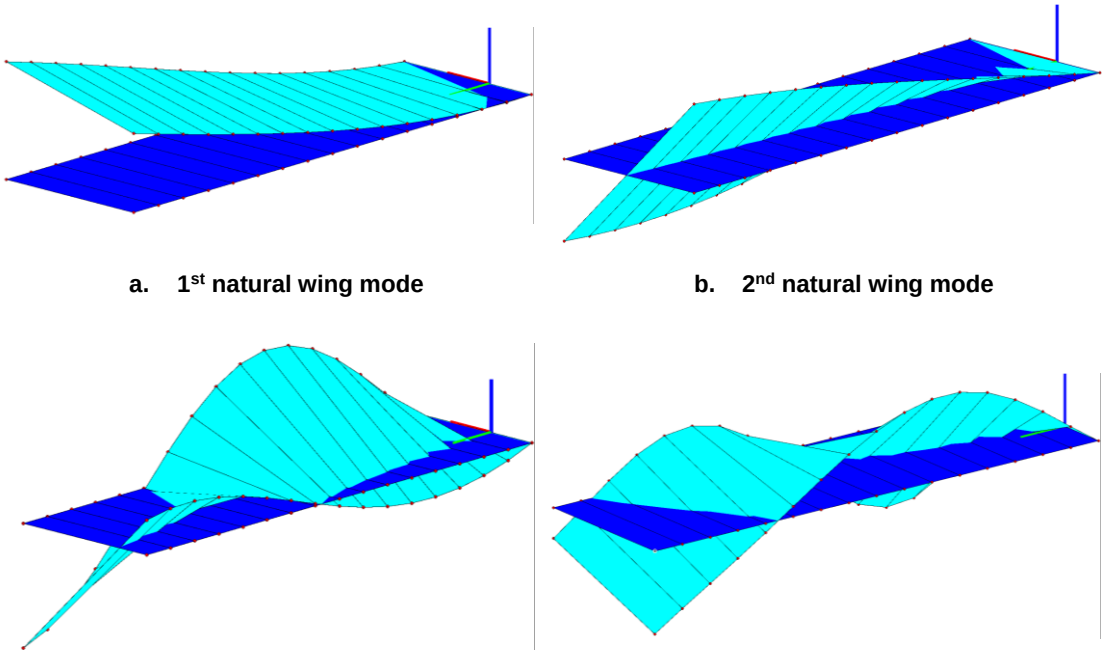

a. 1st natural wing mode **b. 2nd natural wing mode**

c. 3rd natural wing mode **d. 4th natural wing mode**

Figure 4-7: *Goland Wing* – Visualization of first 4 natural modes

From Figure 4-7, it could be observed that:

1. The 1st wing mode shape is bending dominated, with a large out-of-plane bending displacement and a small out-of-plane torsional displacement.

2. The 2nd wing mode shape is torsional dominated, with a large out-of-plane torsional displacement and a small out-of-plane bending displacement.
3. The 3rd and 4th wing mode shapes are both bending and torsional dominated, with moderate out-of-plane bending and torsional displacements.

These results agreed with the results obtained by Dimitriadis and Vio [41]. Next, FMI simulations were performed on the *Goland Wing* model for all 4 mode shapes. The sampling frequencies (f_{samp}) were chosen such that each mode shape oscillated with a desired reduced frequency (k). In each simulation, the scaling factor for the eigenvectors (amp_{Max}) was 0.1 (as the eigenvectors calculated were normalised). While the oscillating amplitude and frequency highly depend upon the freestream conditions, the main goal of performing these simulations was to analyse the aerodynamic behaviour of the system, which is:

a) normalised w.r.t the freestream conditions by studying the force coefficients (C_L, C_M) and
b) is independent of the oscillating amplitude's magnitude at small oscillating amplitudes (validated in chapter 4.1.1).

The complete simulation parameters are detailed in Table 4-7.

Table 4-7: *Goland Wing* (Standalone Wing) – Simulation settings: Motion solver validation study

Parameter (Fixed)	**Value**
Freestream velocity (u_∞, ms^{-1})	50.0
Freestream density (ρ_∞, kgm^{-3})	1.225
Scaling factor ($amp_{Max}, -$)	0.1
Parameter (Varying)	**Range**
Mode Shapes	1, 2, 3, 4
Reduced frequency ($k, -$)	0.05, …., 0.1

The amplitude ($C_{L_{Max}}$, $C_{M_{Max}}$) and phase shifts (ψ_L, ψ_M) of the resulting lift and moment forces are shown in Figure 4-8, with each line representing a fixed mode shape and varying k.

The $C_{L_{Max}}$ and $C_{M_{Max}}$ vs k plots should display similar trends as seen in Figure 4-3 and Figure 4-4. All 4 modes showed an increase in $C_{L_{Max}}$ and $C_{M_{Max}}$ for an increase in k, which can be observed in both the pitching wing case (Figure 4-3) and plunging wing case (Figure 4-4) for the *Veldhuis Wing*. The 1st and 2nd mode shapes showed a larger variation in $C_{L_{Max}}$ and $C_{M_{Max}}$ for a change in k, as they are dominated by a single motion (bending/torsion), i.e. either one of the average spanwise torsional or bending displacements is large. The 3rd and 4th mode shapes are characterised by a combination of both bending and torsional modes with the average spanwise torsional and bending displacements being small.

Hence, the magnitudes of $C_{L_{Max}}$ and $C_{M_{Max}}$ as well as the variations in $C_{L_{Max}}$ and $C_{M_{Max}}$ for a change in k were smaller.

For the same amp_{Max}, the bending component of the motion is not as dominant as the torsional component of the motion, as $amp_{Max} = 0.1m$ indicates a 0.1m maximum vertical displacement ($h = 0.0547$) which is considered to be low, while $amp_{Max} = 0.1rad$ indicates a 5.73° maximum angle of attack ($\alpha_{W_{Max}} = 5.73°$) which is considered to be moderate. Hence, the 1st torsional dominated mode (wing mode shape 2) had the largest magnitudes of $C_{L_{Max}}$ and $C_{M_{Max}}$.

The 2nd and 4th mode shapes are characterised by a larger average spanwise torsional displacement and a relatively smaller average spanwise bending displacement. Hence, the ψ_L and ψ_M vs k plots for these modes had similar trends (phase lead; ψ_L increased with k; ψ_M decreased with k) as seen in the pitching motion case for the *Veldhuis Wing* model (Figure 4-3). The 1st and 3rd mode shapes are characterised by a larger average spanwise bending displacement and a relatively smaller average spanwise bending displacement. Hence, the ψ_L and ψ_M vs k plots for these modes had similar trends (phase lag; ψ_L increased with k; ψ_M decreased with k, minimum ψ_M value observed) as seen in the plunging motion case for the *Veldhuis Wing* model (Figure 4-4).

These results showed that the motion solver coupled with DUST can be used to perform simulations of wing mode shapes with high accuracy. These results were used to analyse results for a wing-propeller model undergoing wing mode shapes in chapter 7.

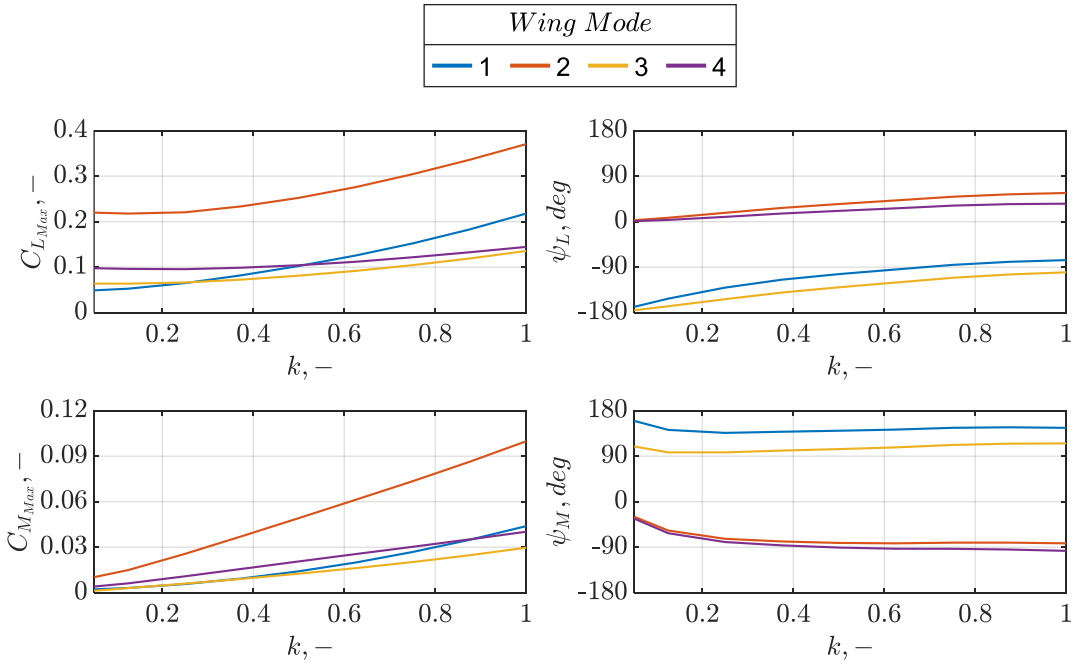

Figure 4-8: *Goland Wing* (Standalone Wing) – *k* variation

5 Validation Studies for Propeller-Wing Interaction: Stationary Wing and Propeller

5.1.1 Model Descriptions and Simulation Settings

To run the simulations required in this thesis, the models used must first be validated. In addition to the model, it is necessary to validate whether the motion solver coupled with DUST could adequately capture the interaction between the propeller and the wing. To verify existing propeller-wing interaction studies, Veldhuis' doctoral thesis was used as the framework [4]. The model and simulation settings chosen were nearly identical to the those used by Veldhuis in his doctoral thesis. The wing and propeller chosen with their parameters are given below.

5.1.1.1 Model Description

The wing used a NACA 64_2-a015 airfoil with no twist ($\theta_W = 0°$), no sweep ($\lambda_W = 0°$), no dihedral ($\gamma_W = 0°$) and constant chord. It had a chord length (c_W) of 0.24m and a span (b_W) of 0.64m. Since the focus of this thesis was on propeller-wing interaction, the fuselage was neglected and the wing model was mirrored in the opposite direction, making the total span of the wing, $b_W = 1.28m$. Table 5-1 provides the complete information regarding the wing model parameters.

Table 5-1: *Veldhuis Wing* – Model description: Wing-propeller interaction validation studies

Parameter	Value
Airfoil	NACA 64_2-a015
Planform	Rectangular
Wingspan (b_W, m)	1.28
Wing chord (c_W, m)	0.24
Wing sweep (θ_W, deg)	0
Wing twist (λ_W, deg)	0
Wing dihedral (γ_W, deg)	0

The propeller was mounted on just one side of this double wing model (propeller mounted on the left wing) and hence the discretization of the surface panels for this wing was nearly double that of the other wing to sufficiently capture the propeller-wing interaction. No nacelle was modelled, as the position and inclination of the propeller was varied for each simulation. While the nacelle does have an influence on the propeller-wing interaction, the overall effects of the propeller on the wing are not impacted by the presence of the nacelle, which was the main goal of this thesis. Figure 5-1 shows the complete wing-propeller model with the discretization of the surface panels created by DUST.

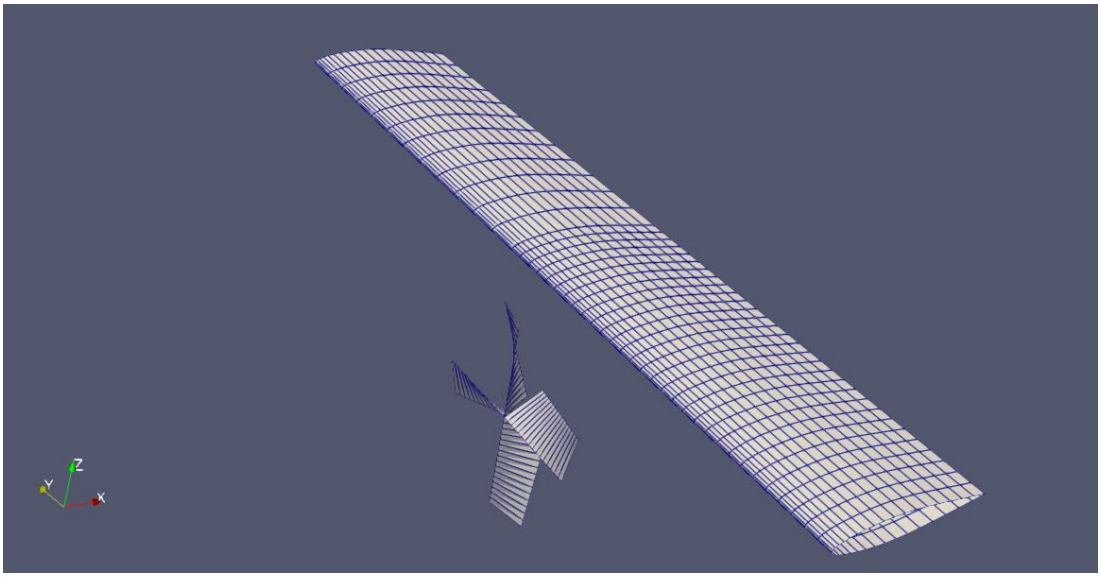

Figure 5-1: *Veldhuis Wing* (NACA 64_2-a015) + *Propeller 1* model created in DUST

The C_L and inviscid drag ($C_{D_{inv}}$) for the standalone wing were calculated at $u_\infty = 50\ ms^{-1}$ and sea-level conditions and the C_L and $C_{D_{inv}}$ vs α_W curves were plotted and shown in Figure 5-2. It could be observed that the lift curve was linear, and the drag curve was parabolic, which was to be expected. At $\alpha_W = 0°$, C_L and $C_{D_{inv}}$ must be 0 which could be observed here.

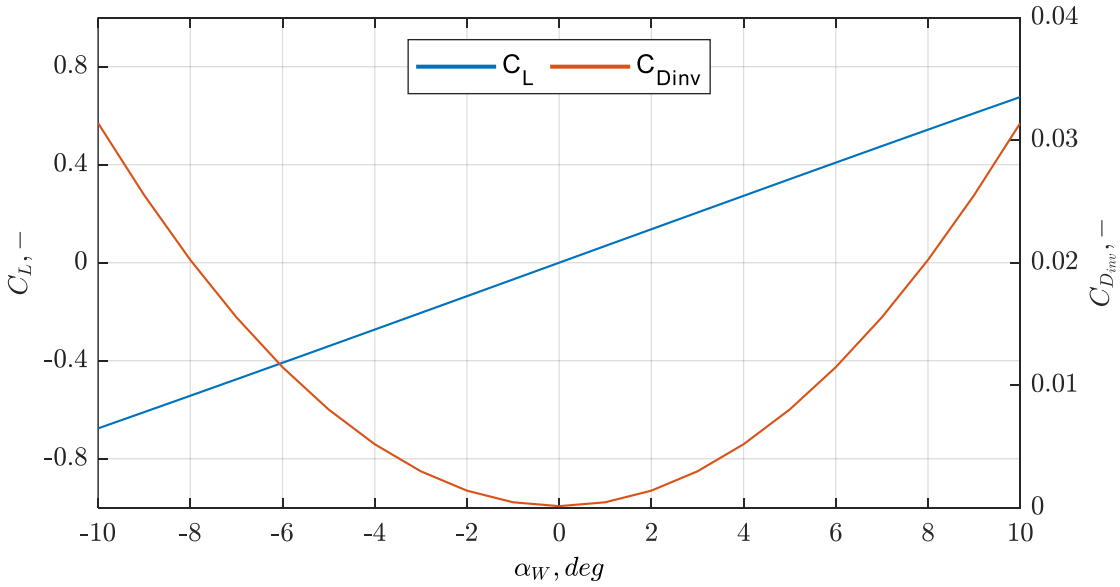

Figure 5-2: *Veldhuis Wing* (Standalone Wing, NACA 64_2-a015) – C_L and C_{Dinv} vs α_W

The exact data for the propeller was not provided by Veldhuis and hence a simple propeller was modelled to obtain similar thrust coefficients as in his thesis. The propeller was designed with a linearly distributed blade twist (θ_P) = 48° and blade pitch ($\beta_{0.75}$) = 25°. The airfoil used for the blade was NACA 0012 and each blade

had no sweep and a constant chord length (c_P) of 0.053m. The radius of the blade (R) was 0.118m. The exact specifications of the propeller are given in Table 5-2.

Table 5-2: *Propeller 1* – Model description: Wing-propeller interaction validation studies

Parameter	Value
Airfoil	NACA 0012
Number of blades	4
Propeller radius (R, m)	0.118
Propeller chord (c_P, m)	0.053
Propeller twist (θ_P, deg)	48
Twist distribution	Linear
Propeller sweep (λ_P, deg)	0
Propeller blade pitch angle ($\beta_{0.75}, deg$)	25

The thrust coefficient (C_T) vs advance ratio (J) for the propeller is depicted in Figure 5-3, which showed that as J increased (ω decreased), the propeller's C_T decreased, which is typically observed in a propeller's performance curve. The curve began at a minimum J value as for any advance ratio below this, the wingtip Mach number exceeded 1.0 and could not be processed by DUST.

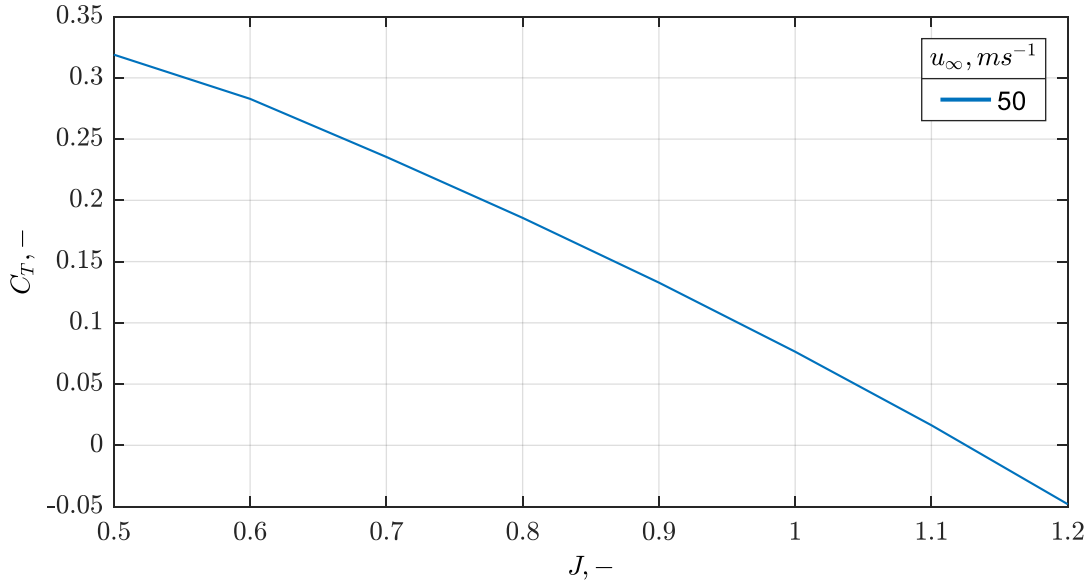

Figure 5-3: *Propeller 1* – C_T vs J

5.1.1.2 Simulation Settings

To validate existing propeller-wing interaction studies [3–6], the focus of this chapter was on the major parameters that influenced the propeller's influence on the wing. The major parameters included the propeller operational conditions (J, rotational direction) as well as the propeller spanwise position and orientation

($y_P/b_W/2$, $\alpha_{P\to W}$). The range of these parameters as well as the fixed simulation parameters are given in Table 5-3.

Table 5-3: *Veldhuis Wing* (+ *Propeller 1*, NACA 64_2-a015) – Simulation settings: Wing-propeller interaction validation studies

Parameter (Fixed)	Value
Freestream density (ρ_∞, kgm^{-3})	1.2
Freestream velocity (u_∞, ms^{-1})	50
(Propeller) Normalised X-position ($x_P/c_W, -$)	-0.841
(Propeller) Normalised Z-position ($z_P/R, -$)	0.0
Parameter (Varied)	**Range**
Wing angle of attack (α_W, deg)	0, ……, 10
Blade pitch angle ($\beta_{0.75}, deg$)*	20, 25, 30
Rotation direction	IU, OU
Advance ratio ($J, -$)	0.81, ……, 1.1
(Propeller) Normalised Y-position ($y_P/b_W/2, -$)	0.3, ……, 1.0
Propeller relative inclination ($\alpha_{P\to W}, deg$)	-28, ……, 10

5.1.2 Results and Discussion

5.1.2.1 Propeller Thrust

For this set of FMI simulations, only the propeller model was simulated, and two different thrust conditions were considered:

a) Low thrust (LT) case ($J = 0.9$, $C_T = 0.133$) and

b) High thrust (HT) case ($J = 0.7$, $C_T = 0.235$).

The radial thrust distributions for both thrust cases have been plotted in Figure 5-4. It was seen that in both thrust cases, the maximum thrust was produced approximately between non-dimensional propeller radial locations, $r/R = 0.7$ and $r/R = 0.9$, which agreed with the current research (depicted in Figure 2-12).

Next, FMI simulations were performed for the *Veldhuis Wing* + *Propeller 1* model at a small angle of attack ($\alpha_W = 1°$). The pressure coefficient gradient in the Y-Z plane of the flowfield for the LT case just behind the propeller and at the wing leading edge (LE) are shown in Figure 5-5 and Figure 5-6 respectively. It was observed that the pressure coefficient (C_P) behind each blade was much lower due to the increased velocity induced by the blade rotation, hence decreasing the dynamic pressure component. Once the propeller wake settled, the increased pressure distribution region became a single band as seen in Figure 5-6. This

* The propeller-wing interaction validation studies for blade pitch angle ($\beta_{0.75}$) variation were additional studies performed to validate the propeller-wing model. For all other validation studies, $\beta_{0.75}$ was fixed at 25°. The blade pitch angle studies can be found in Appendix C.

confirmed the “donut” wake formation of the propeller depicted in Figure 2-11 and Figure 2-12.

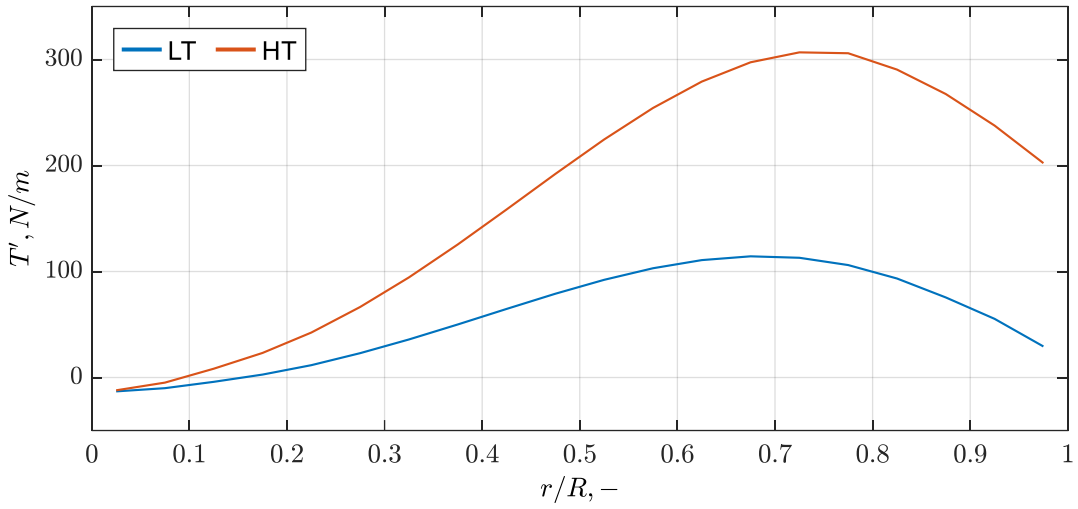

Figure 5-4: *Propeller 1* – Radial thrust distribution

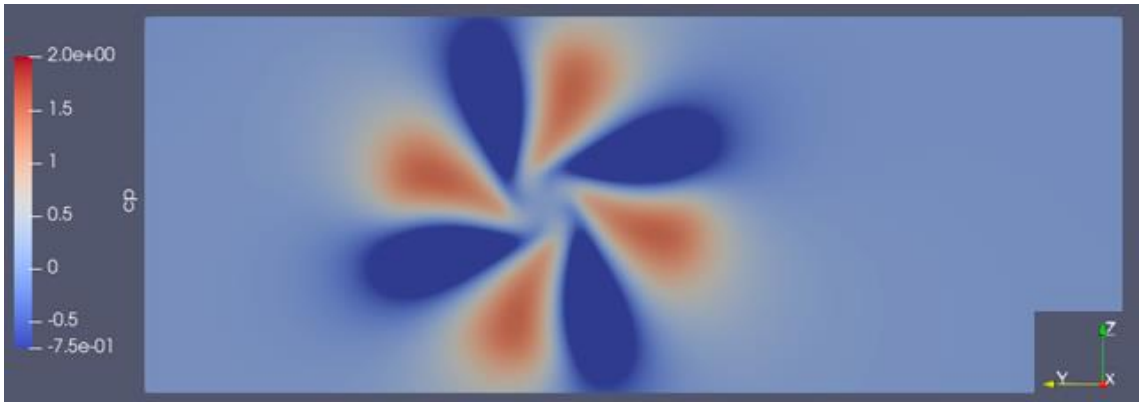

Figure 5-5: *Veldhuis Wing* (+ *Propeller 1*, NACA 64_2-a015) – C_P gradient immediately downstream of the propeller

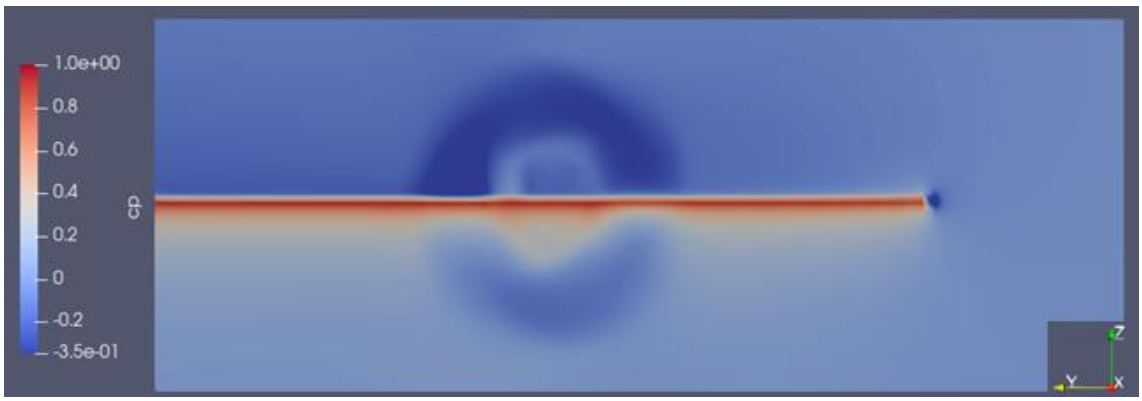

Figure 5-6: *Veldhuis Wing* (+ *Propeller 1*, NACA 64_2-a015) – C_P gradient at wing LE

5.1.2.2 Rotation Direction

According to existing research, Inboard Up (IU) rotating propellers are typically preferred over Outboard Up (OU) rotating propellers. To validate this, FMI simulations were performed for both directions of propeller rotation at different wing angle of attacks (α_W). The simulation parameters are provided in Table 5-4.

Table 5-4: *Veldhuis Wing* (+ *Propeller 1*, NACA 64_2-a015) – Model parameters and simulation settings: Rotation direction validation study*

Parameter	Value
Wing angle of attack (α_W, deg)	0, 2, 4, 6, 8, 10
Rotation direction	IU, OU
Advance ratio $(J, -)$	0.85
Normalised Y-position $(y_P/b_W/2, -)$	0.469
Propeller relative inclination $(\alpha_{P\to W}, deg)$	0.0

The C_L vs α_W for both rotation directions and the standalone wing have been depicted in Figure 5-7. The spanwise C_L distribution for a) $\alpha_W = 0°$ and b) $\alpha_W = 4°$ have been plotted and compared to the results obtained by Veldhuis [4] in Figure 5-8. The spanwise blade tip and blade centre locations have been depicted using red and green dashed lines, respectively.

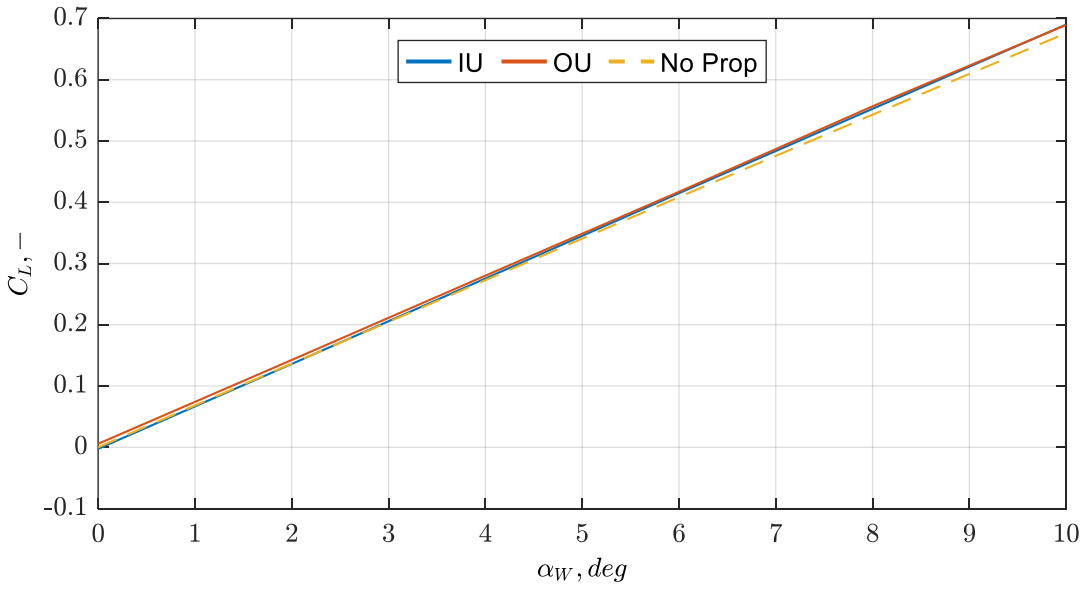

Figure 5-7: *Veldhuis Wing* (+ *Propeller 1*, NACA 64_2-a015) – C_L vs α_W: Rotation direction variation

* To change the direction of rotation of the propeller from Inboard Up (IU) to Outboard Up (OU), the propeller model was mirrored in the X-Z plane in DUST and the rotation axis (positive X-axis) was inverted (negative X-axis) in the MATLAB Motion Solver.

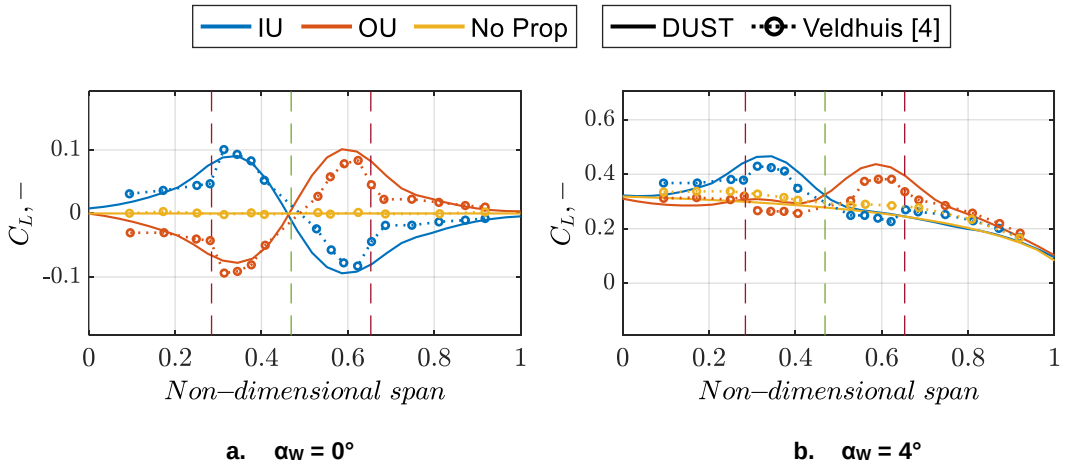

Figure 5-8: *Veldhuis Wing* (+ *Propeller 1*, NACA 64_2-a015) – Spanwise C_L distribution: Rotation direction variation, Comparison with Veldhuis results [4]

From the C_L vs α_W graph (Figure 5-7), it was observed that in both IU and OU rotation cases, there was a slight increase in C_L compared to the standalone wing case. Another observation that could be made was that the C_L vs α_W slope for IU rotation and OU rotation cases were higher compared to the standalone wing case with the slope for the IU rotation case being higher than the slope of the OU rotation case. The increase in C_L and C_L slope for the IU case could simply be explained by the increase in local C_L due to blade rotation direction augmented by the increase in dynamic pressure above the wing due to the propeller centre moving above the mean wing chord line for increasing α_W values. This can be seen in Figure 5-8 (This can also be seen in the blade pitch angle validation studies (0)). In Figure 5-8, it could be seen that the results obtained from the FMI simulations were similar to the experimental results performed by Veldhuis. This highlighted the accuracy of DUST in capturing the interaction between the wing and the propeller.

A unique observation in Figure 5-7 and Figure 5-8 that can be made is that the C_L for OU rotation at $\alpha_W = 0°$ is higher than both C_L for IU rotation and for the standalone wing, which is a minor deviation from previous research. Apparently, the local increase in C_L behind the propeller on the UBS side caused a large increase in C_L for the rest of the wing on the UBS side (propeller centre to wing tip). This was due to the asymmetrical spanwise positioning of the propeller with respect to the wing (also seen in the blade pitch angle validation studies (0)). The longer region of the wing between the propeller and the wing tip had a substantial increase in C_L whereas the shorter region between the propeller and the wing root had a smaller decrease in C_L. Hence, the net C_L of the wing was greater than 0 (C_L of standalone wing at $\alpha_W = 0°$).

The spanwise C_L distribution at various α_W for the IU, OU and standalone wing cases have been depicted at different wing angles of attack in Appendix D.

5.1.2.3 Advance Ratio (J)

For this set of FMI simulations, the operating conditions of the propellers were fixed except for the advance ratio (J) of the propeller. The model and simulation settings are provided in Table 5-5.

Table 5-5: *Veldhuis Wing* (+ *Propeller 1*, NACA 64_2-a015) – Model parameters and simulation settings: Advance ratio validation study

Parameter	Value
Wing angle of attack (α_W, deg)	0, 2, 4, 6, 8, 10
Rotation direction	IU
Advance ratio $(J, -)$	0.81, 0.95,1.11
Normalised Y-position $(y_P/b_W/2\,, -)$	0.469
Propeller relative inclination $(\alpha_{P\to W}, deg)$	0.0

The C_L vs α_W for different J and the standalone wing has been depicted in Figure 5-9. The spanwise C_L distributions at different angles of attack have been provided in Appendix E.

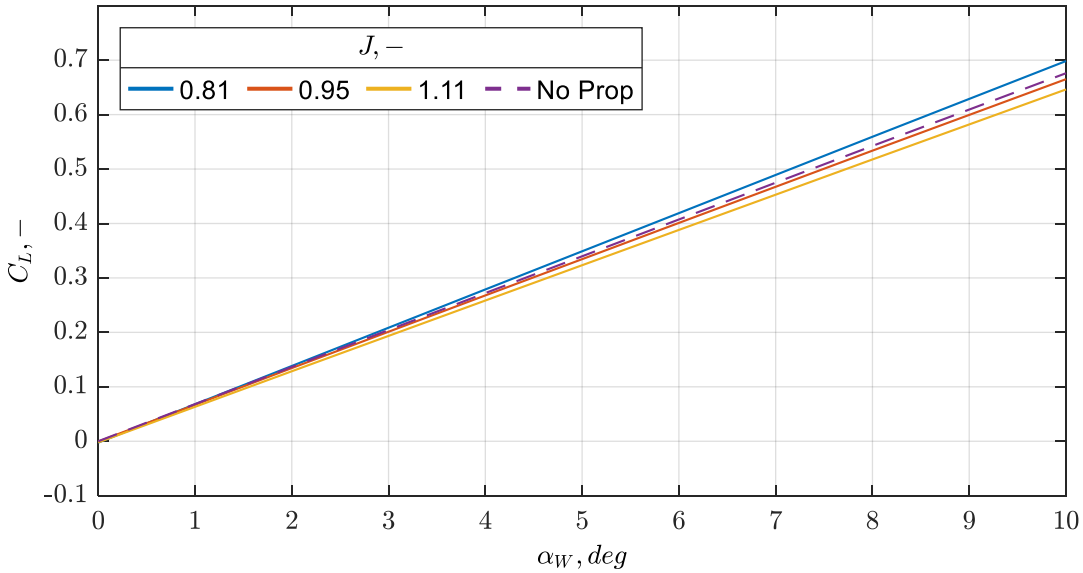

Figure 5-9: *Veldhuis Wing* (+ *Propeller 1*, NACA 64_2-a015) – C_L vs α_W: J variation

There clearly existed a decrease in C_L when J increases. This was because for increasing advance ratios, rotational speed decreases and hence the dynamic pressure due to the propeller wake and subsequently above the wing decreases. This could also be seen in Appendix E where the region behind the propeller on the wing had a larger increase in C_L for smaller J values. For increasing α_W, the propeller centre moves further above the mean wing chord line. Hence, the region above the wing washed by the propeller wake increases, therefore augmenting the effects of the propeller on the wing C_L. This could be seen by the increase in the C_L vs α_W slope for decreasing J.

5.1.2.4 Spanwise Propeller Position ($y_P/b_W/2$)

According to the results from various papers [3–5], the aerodynamic performance of an IU rotating tip-mounted propeller-wing model in a conventional tractor configuration is superior compared to conventional inboard mounted propeller-wing models. To validate this, FMI simulations were performed in which the position of the propeller in the spanwise direction is varied. To focus only on the effects of spanwise position variation, other parameters were set to have minimal influence on the results, i.e. the thrust setting of the propeller was kept low ($C_T = 0.035$), propeller was set in a tractor configuration in-line with the wing ($x_P/c_W = -0.841$, $z_P/R = 0$) and the wing was set at a low angle of attack ($\alpha_W = 4.2°$). The complete set of model and simulation parameters are given in Table 5-6.

Table 5-6: *Veldhuis Wing* (+ *Propeller 1*, NACA 64$_2$-a015) – Model parameters and simulation settings: Spanwise position validation study

Parameter	Value
Wing angle of attack (α_W, deg)	4.2
Rotation direction	IU
Advance ratio ($J, -$)	1.07
Normalised Y-position ($y_P/b_W/2\,, -$)	0.3, …., 1.0
Propeller relative inclination ($\alpha_{P\to W}, deg$)	0.0

The lift-drag (inviscid) ratio, $C_L/C_{D_{inv}}$ (Figure 5-10) and C_L, $C_{D_{inv}}$ (Figure 5-11) curves for a variation in the propeller's spanwise position ($y_P/b_W/2$) have been plotted in (C_{D_i} is the induced drag coefficient, $C_{D_{inv}} = C_{D_i}$ + propeller thrust contribution).

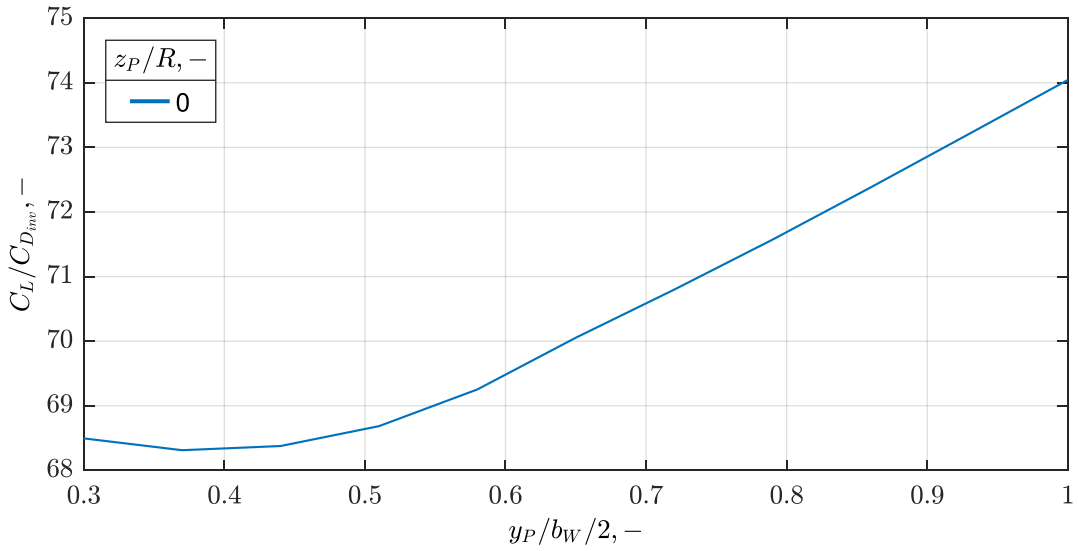

Figure 5-10: *Veldhuis Wing* (+ *Propeller 1*, NACA 64$_2$-a015) – C_L/C_{Dinv} vs $y_P/b_W/2$; C_T = 0.035, α_W = 4.2°

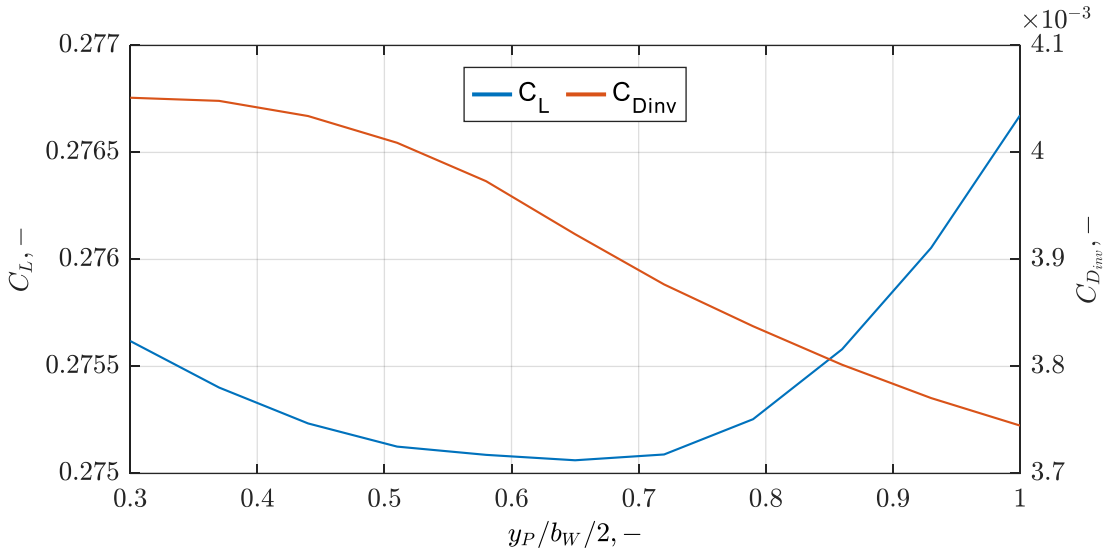

Figure 5-11: *Veldhuis Wing* (+ *Propeller 1*, NACA 64_2-a015) – C_L and C_{Dinv} vs $y_P/b_W/2$; C_T = 0.035, α_W = 4.2°

The lift-drag (inviscid) ratio was much higher for the propeller positioned near the wingtip compared to conventional inboard positions, as seen in Figure 5-10. This could be attributed to a small increase in C_L and a large decrease in $C_{D_{inv}}$ for increasing $y_P/b_W/2$ values, which could be seen in Figure 5-11. The reason for these variations in C_L and $C_{D_{inv}}$ values closer to the wing tip is simply a decrease in the induced drag (C_{D_i}) due to the propeller rotating contrary to the wingtip vortex direction, therefore increasing the effective aspect ratio of the wing. On the other hand, for conventional inboard positions ($0.3 \leq y_P/b_W/2 \leq 0.5$), a very negligible difference in C_L, $C_{D_{inv}}$ and $C_L/C_{D_{inv}}$ was observed. These results were in complete agreement with the previous research summarised in Table 2-1.

5.1.2.5 Propeller Inclination (α_P)

In these set of FMI simulations, propeller inclination with respect to the wing inclination ($\alpha_{P\to W}$) was varied for two wing angle of attacks: a) $\alpha_W = 4.2°$ and b) $\alpha_W = 8.4°$. The propeller inclination varied between $\alpha_P = -24°$ and $\alpha_P = 14°$. The complete list of model parameters and simulation settings are given in Table 5-7.

Table 5-7: *Veldhuis Wing* (+ *Propeller 1*, NACA 64_2-a015) – Model parameters and simulation settings: Propeller inclination validation study

Parameter	Value
Wing angle of attack (α_W, deg)	4.2, 8.4
Rotation direction	0.92
Advance ratio $(J, -)$	IU
Normalised Y-position $(y_P/b_W/2\,, -)$	0.469
Propeller absolute inclination (α_P, deg)	-24, …., 14

C_L and $C_{D_{inv}}$ for both wing angle of attacks have been plotted against the propeller's relative inclination ($\alpha_{P\to W}$) in Figure 5-12. For an increase in $\alpha_{P\to W}$, C_L decreased and $C_{D_{inv}}$ increased. This could be attributed to a decrease in the vertical and horizontal loading vectors on the wing for increasing $\alpha_{P\to W}$ values. Therefore, it could be concluded that lower values of $\alpha_{P\to W}$ lead to better aerodynamic performance of the wing. This observation was in complete agreement with the existing research summarised in Table 2-1.

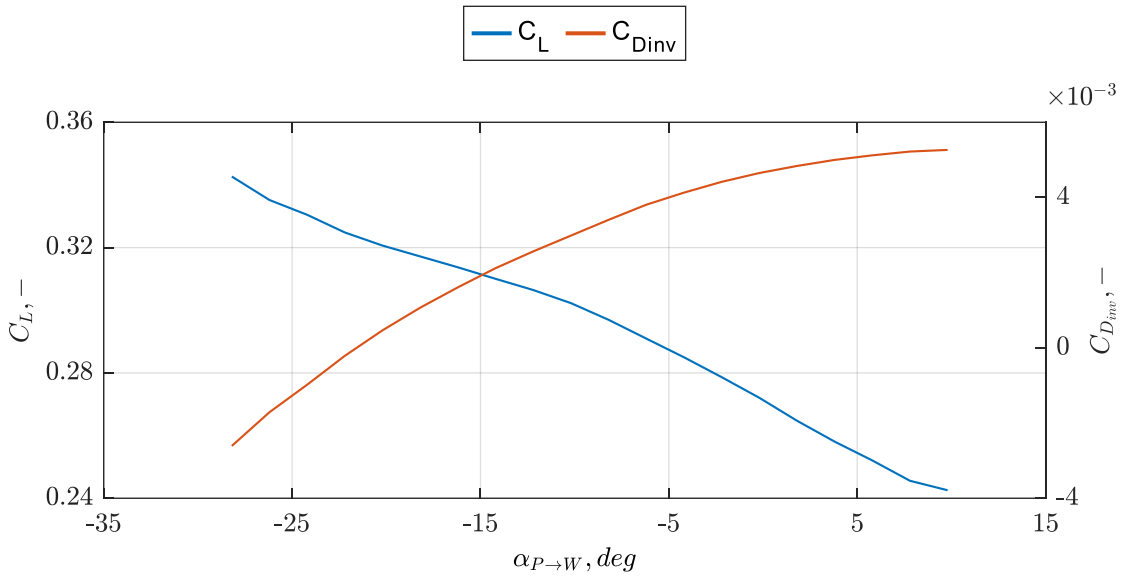

a. α_W = 4.2°

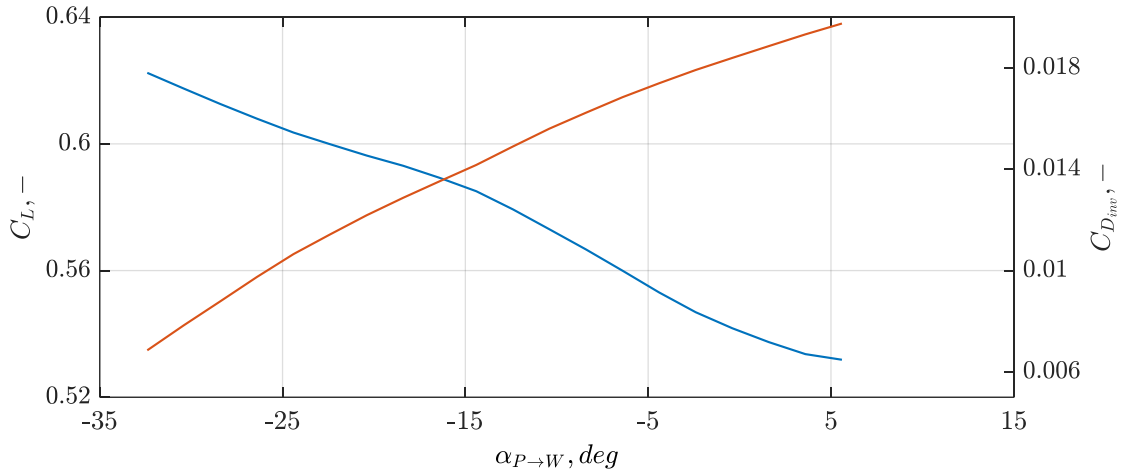

b. α_W = 8.4°

Figure 5-12: *Veldhuis Wing* (+ *Propeller 1*, NACA 64$_2$-a015) – C_L and C_{Dinv} vs $\alpha_{P\to W}$

6 Aerodynamic Investigation of Propeller-Wing Interaction: Simple Wing Motions

There have been numerous studies done to investigate the effect of a propeller on wing stationary with respect to the air flow direction. There are very few complexities involved as the observations mainly deal with steady aerodynamics with the only unsteady components being the propeller blades' motion and the propeller wake. Although the propeller blades have a constantly changing orientation and position, the propeller wake settles after a certain distance downstream of the propeller and acts as a continuous disc of nearly steady flow (validated in chapter 3.4.3). This is an effective way to study the fundamental effects of a propeller on a wing (and vice-versa) but is incomplete as there are numerous unsteady parameters influencing the wing and propeller motion in real-time. More specifically, the motion of the entire wing-propeller system with respect to the air flow, relative motion between a propeller and a wing or even a gust of wind can alter the effects of the propeller on the wing. There has been little to no research done on this topic as added complexities make it difficult to analyse the results. Hence, this chapter will focus on propeller-wing interaction for a wing-propeller system undergoing simple motions such as pure pitching and pure plunging oscillatory motions. Although these types of simple oscillatory motions are not realistic, the results from these simulations act as a solid framework for future studies with more complex motions.

For all the FMI simulations performed in this chapter, the model used in chapter 3.4.3 for the propeller-stationary wing interaction validation studies was re-used (*Veldhuis Wing* + *Propeller 1*). The model descriptions for the wing and propeller are provided in Table 5-1 and Table 5-2 respectively. A conventional in-line tractor configuration was maintained for all simulations to ensure the primary agents impacting the results to be the motions of the wing and propeller. The fixed model and simulation parameters are given in Table 6-1.

Table 6-1: *Veldhuis Wing* (+ *Propeller 1*) – Fixed model parameters and simulation settings: Dynamic wing-propeller interaction studies

Parameter	Value
Airfoil	NACA 64_2-a015
Freestream density (ρ_∞, kgm^{-3})	1.2
Freestream velocity (u_∞, ms^{-1})	50
Normalised Y-position ($y_P/b_W/2\,, -$)	0.5
Normalised Z-position ($z_P/R\,, -$)	0.0
Normalised X-position ($x_P/c_W\,, -$)	-0.841

An example of the output obtained from the 'Integral Loads' post-processing function of DUST for a sinusoidal motion input is provided in Figure 6-1. For the standalone wing, a smooth sinusoidal output (see Figure 2-6) can be observed as there are no rapid motions involved, ensuring linear behaviour. When a propeller is added to the wing, the output maintains its sinusoidal shape (wing motion is the dominant factor), but with irregular variations. These non-linearities are caused by the propeller blades inducing fluctuations in the wake and the flow around the wing. Choosing the right time step becomes critical to ensure that these non-linearities are captured efficiently. While these variations in the output due to the blade rotations may be small, in certain cases, the oscillation in the forces induced by the wing motion might be small and comparable to these variations induced by the blades. The relatively large variations due to the blades can affect the 'FFT' function output and skew the results. This was observed in certain simulations performed during this thesis and can be considered a limitation of the 'FFT' function in MATLAB.

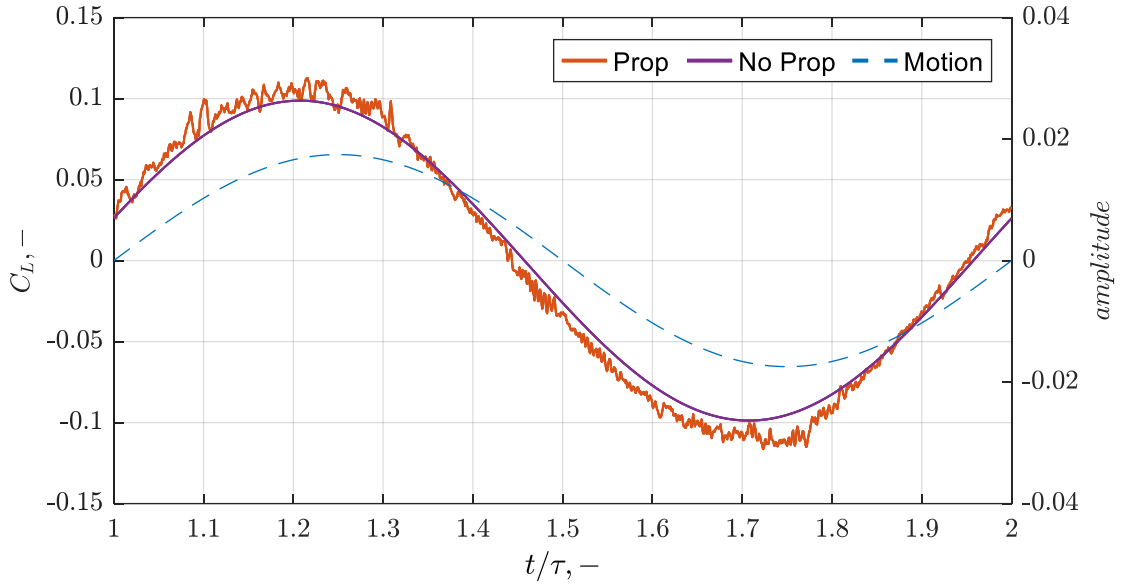

Figure 6-1: Example of DUST output for wing-propeller and standalone wing models for a sinusoidal input

6.1 Wing with Rigidly Attached Propeller

For the FMI simulations performed in this chapter, it was ensured that the propeller was rigidly attached to the wing. Since there is no nacelle or pylon included in the model, rigidity was maintained by ensuring there was no relative motion between the wing and the propeller, i.e. the propeller will have a fixed position and orientation in the wing's reference frame. Two sets of FMI simulations for both the pure-pitching and pure-plunging cases: a) varying wing motion parameters (k and amp_{Max}, see chapter 6.1.1) and b) varying propeller settings (J, see chapter 6.1.2) have been performed. The effects of the rigidly

attached propeller on the aerodynamic performance of pitching and plunging wings were studied and compared to the standalone wing.

6.1.1 Wing Motion Variation

For the first set of FMI simulations, the influence of the wing motion on the propeller-wing interaction was studied. Hence, k and amp_{Max} were varied while keeping all other parameters of the wing (as well as the propeller settings and position) fixed. The simulation parameters are given in Table 6-2.

Table 6-2: *Veldhuis Wing* (+ *Propeller 1*, NACA 64_2-a015) – Simulation settings: Rigid propeller-wing attachment study, *k* and amp_{Max} variation

Parameter (Fixed)	Value
Advance ratio ($J, -$)	0.9
Wing initial angle of attack (α_{W_0}, deg)	0
Wing phase offset (φ_W, deg)	0
Parameter (Varying)	**Range**
Wing pitch amplitude ($\alpha_{W_{Max}}$, deg)	1, 2, 4
Normalised plunge amplitude ($h, -$)	0.025, 0.05, 1.0
Reduced frequency ($k, -$)	0.101, …., 1.005

As seen in chapter 2.2.2, representation of the lift and moment forces using their respective transfer functions was beneficial to observe the behaviour of the wing system at different values of k and amp_{Max} ($L(k, amp_{Max}) \rightarrow H_L(k, amp_{Max})$, $M(k, amp_{Max}) \rightarrow H_M(k, amp_{Max})$).

In Figure 6-2 and Figure 6-3, the lift and moment transfer functions of the wing-propeller model (*Veldhuis Wing* + *Propeller 1*) and the standalone wing (*Veldhuis Wing*) are plotted in the complex plane, for pitching and plunging motions respectively. Each line represents a fixed amp_{Max} and varying k, with the dashed line representing the standalone wing (see Figure 4-1 and Figure 4-2) and solid line representing the wing-propeller model. Each marker represents the transfer function at a certain k, and each colour represents a different amp_{Max}. Additionally, the dotted lines are used to join these curves with the stationary wing transfer functions, i.e. $k = 0$ $(H_L(0), H_M(0))$. These points indicate the lift and moment transfer functions of the wing at its peak pitching/plunging amplitude ($\alpha_W = \alpha_{W_{Max}}, h_W = h_{W_{Max}}$) with no motion of the wing (hence a different line style was used to connect these points).

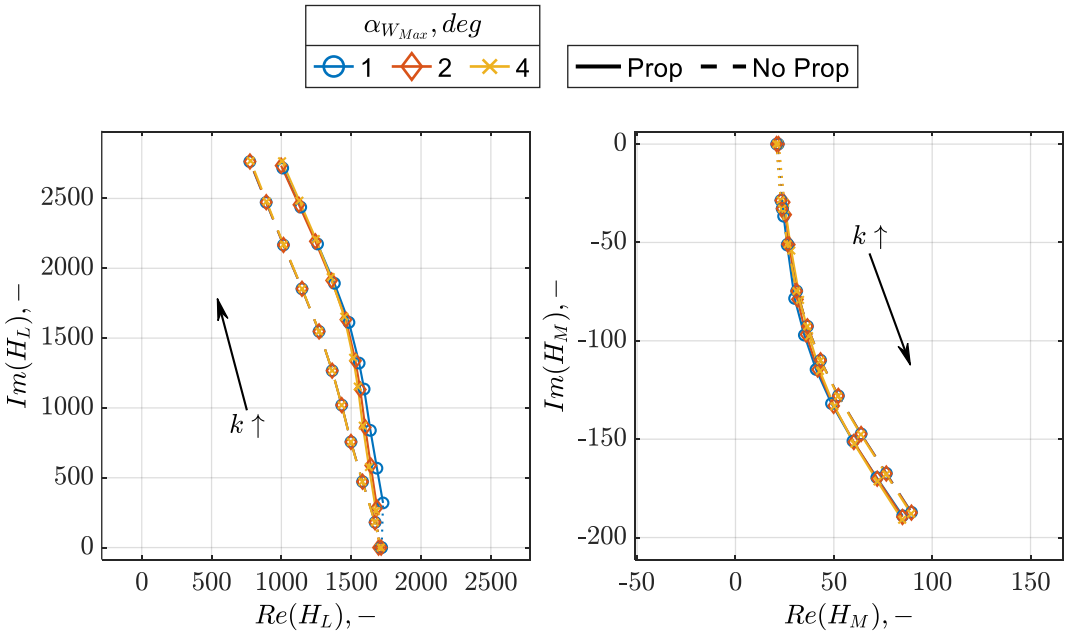

Figure 6-2: *Veldhuis Wing* (+ *Propeller 1*, NACA 64_2-a015, Pitching motion) – Rigid propeller-wing attachment vs Standalone wing: Wing motion variation, Complex plane representation

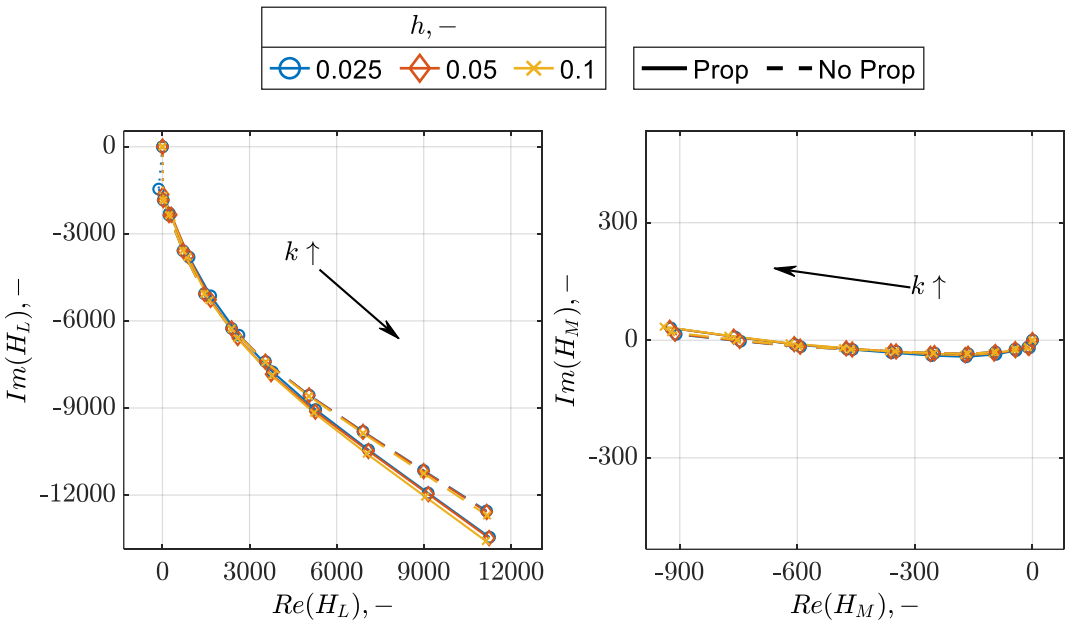

Figure 6-3: *Veldhuis Wing* (+ *Propeller 1*, NACA 64_2-a015, Plunging motion) – Rigid propeller-wing attachment vs Standalone wing: Wing motion variation, Complex plane representation

From the complex plan representations (Figure 6-2 and Figure 6-3), nearly identical trends in H_L and H_M were observed for the wing-propeller models compared to the standalone wing (these trends were also similar to the trends observed in the validation studies in chapter 4.1.1. The magnitudes of H_L and H_M for the wing-propeller model (in the chosen range of k) were larger than that of the standalone wing model. This was to be expected as the propeller is producing a net positive thrust and hence has a positive influence on the wing performance,

which can be observed in Figure 5-9. A small difference that could be observed was that unlike the H_L and H_M curves for the standalone wing model which overlapped, the H_L and H_M curves for the wing-propeller model showed a slight deviation, most likely due to the unsteady effects of the blade rotation. These unsteady effects skewed the 'FFT' function results, but this needs to be validated. It can also be observed that there is a small phase shift between the wing-propeller and standalone wing configurations. While studying the influence of the propeller on the phase shift is necessary to fully understand the complex propeller-wing interaction space, the phase shift differences observed for the chosen model parameters and simulation settings were considered negligible and hence, warranted no further investigation.

In the pitching motion case, a non-zero angle of attack introduces a certain amount of lift and moment force on the stationary wing, indicated by the positive magnitude transfer functions ($|H_L(0)|, |H_M(0)| > 0$), while in the plunging motion case, a non-zero plunge amplitude does not introduce any lift or moment force on the stationary wing (symmetric wing, $\varphi_W = 0°$), indicated by the zero magnitude transfer functions ($|H_L(0)|, |H_M(0)| = 0$).

Comparing the transfer functions between the wing-propeller and standalone wing configurations, a small positive variation could be observed in the pitching motion case. Although the difference was negligible, this was primarily due to the low thrust setting of the propeller and would most likely be larger and no longer negligible for larger thrust cases.

To further validate these observations, the difference in $C_{L_{Max}}$ and $C_{M_{Max}}$ (ΔC_L and ΔC_M respectively) between the wing-propeller model and the standalone wing model were plotted against k in Figure 6-4. Each line colour represents a different pitching/plunging amplitude.

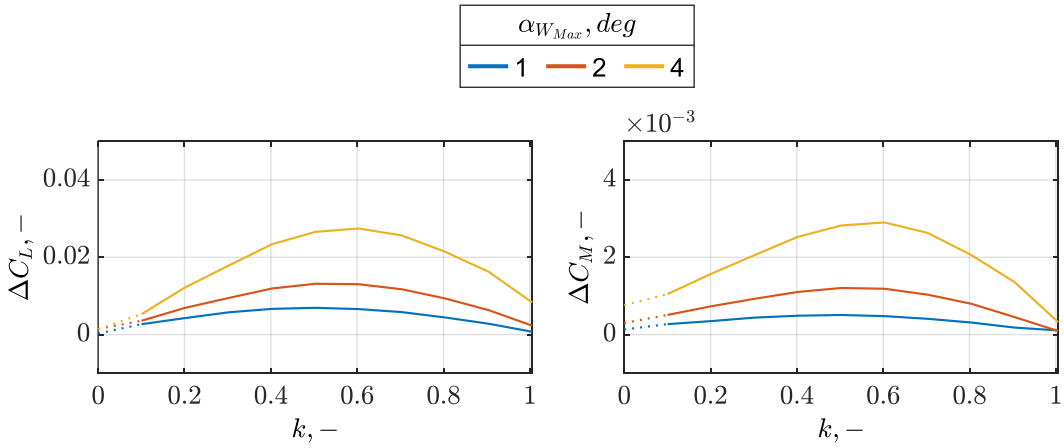

a. Pitching motion

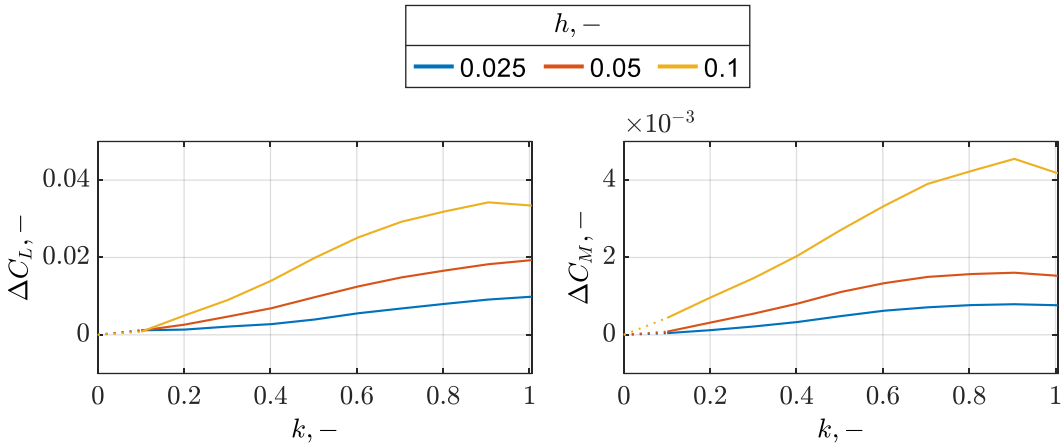

b. Plunging motion

Figure 6-4: *Veldhuis Wing* (+ *Propeller 1*, NACA 64_2-a015) – Rigid propeller-wing attachment vs Standalone wing: C_{LMax}, C_{MMax} comparison, *k* variation

It could be observed that ΔC_L and ΔC_M were larger for larger values of amp_{Max}, as larger pitching/plunging amplitudes amplify the unsteady aerodynamic effects. ΔC_L and ΔC_M increased, reached a maximum value, and decreased for a further increase in k. In comparison to the ΔC_L and ΔC_M values in the pitching case, the ΔC_L and ΔC_M values in the plunging case were more pronounced implying that the propeller's influence is more substantial when the wing undergoes larger vertical displacements.

The presence of a peak in ΔC_L and ΔC_M indicated a resonance-like behaviour where the aerodynamic response is maximised. At certain frequencies, the unsteady aerodynamic forces caused by the wing's pitching motion are in phase with the additional velocity field induced by the propeller wake. This phasing can cause constructive interference, leading to a significant increase in the aerodynamic forces and moments. It must be noted that while ΔC_L and ΔC_M are exceedingly small for the chosen propeller advance ratio and thrust settings, this may not be the case for different propeller advance ratios and thrust settings and requires further investigation.

As seen from the transfer functions, a stationary wing with a thrusting propeller has a slight increase in the lift and moment forces compared to the standalone wing in the pitching motion case and no change in the plunging motion case. This could be observed at $k = 0$, with a) $\Delta C_L, \Delta C_M > 0$ in the pitching motion case and b) $\Delta C_L, \Delta C_M = 0$ in the plunging motion case. The ΔC_L and ΔC_M values at $k = 0$ are the influence of the propeller thrust setting on the wing. As k increases, the influence of the propeller motion also came into play and had a positive influence on the wing. The combination of the propeller wake and the propeller motion had an overall positive influence on the wing (thrusting propeller), with its maximum

influence occurring at the resonant reduced frequencies ($k_{Resonant-Pitching} \approx 0.6$, $k_{Resonant-Plunging} \approx 0.9$).

It must be noted that the initial angle of attack of the wing (α_{W_0}) for all the simulations was fixed at 0°. The possible influence of α_{W_0} on the lift and moment forces and phase shifts is not within the scope of this thesis.

6.1.2 Propeller Settings Variation

For the next set of FMI simulations, the influence of the propeller settings on the propeller-wing interaction was studied. The propeller thrust was varied by varying the advance ratio (J). Hence, for each subset of these simulations, J was varied while keeping the propeller position (as well as the wing k and amp_{Max} in each simulation) fixed. The model settings and simulation parameters are given in Table 6-3.

Table 6-3: *Veldhuis Wing* (+ *Propeller 1*, NACA 64_2-a015) – Simulation settings: Rigid propeller-wing attachment study, advance ratio (*J*) variation

Parameter (Fixed)	Value
Wing initial angle of attack (α_{W_0}, deg)	0
Wing phase offset (φ_W, deg)	0
Parameter (Varying)	**Range**
Advance ratio ($J, -$)	0.5, …., 1.4
Wing pitch amplitude ($\alpha_{W_{Max}}, deg$)	4
Normalised plunge amplitude ($h, -$)	0.05
Reduced frequency ($k, -$)	0.201, 0.302, 0.402, 0.503

For the results obtained from these simulations, the variations in the transfer functions (i.e. the variations in the lift and moment forces and phase shifts) were exceedingly small and hence, would be difficult to observe in the complex plane. Instead, in Figure 6-5 and Figure 6-6, the difference in $C_{L_{Max}}$, $C_{M_{Max}}$, ψ_L and ψ_M between the wing-propeller model and the standalone wing (ΔC_L, ΔC_M, $\Delta\psi_L$ and $\Delta\psi_M$ respectively) were plotted against J. Each line in Figure 6-5 and Figure 6-6 represents a fixed amp_{Max} and a different k. In Figure 6-5, $\alpha_{W_{Max}} = 4.0°$ and in Figure 6-6, $h = 0.05$.

For all combinations of amp_{Max} and k, ΔC_L, ΔC_M, $\Delta\psi_L$ and $\Delta\psi_M$ were positive for positive propeller thrust settings (lower J values) and decreased for an increase in J, with deviations in these trends observed at certain operating conditions. The propeller slipstream has a stronger effect at lower J (higher propeller thrust for a fixed u_∞). As J increased (while amp_{Max} and k are fixed), the relative impact of the propeller wake on the flow around the wing decreased, leading to smaller

differences in ΔC_L, ΔC_M, $\Delta\psi_L$ and $\Delta\psi_M$. Apparently, the advance ratio at which the force and phase differences become 0 was around the advance ratio at which the propeller stopped producing thrust (windmilling condition). For the current propeller model, i.e. *Propeller 1*, the windmilling advance ratio was around 1.12 (as seen in Figure 5-3), and nearly all curves intersect at this advance ratio. As seen in chapter 6.1.1, ΔC_L and ΔC_M were larger for larger amp_{Max} and maximum at the resonant k. But this was observed to be true only when the propeller is thrusting ($C_T > 0$).

The deviations in this trend were most likely due to the oscillations in the forces by the blades, which resulted in deviations in the FFT calculations. These deviations were more prominent at lower amp_{Max} and k, and were more prominent in the plunging wing cases as the propeller's influence is more substantial when the wing undergoes larger vertical displacements (as seen in chapter 6.1.1).

At lower J values, a positive $\Delta\psi_L$ and $\Delta\psi_M$ was observed. One likely reason for this could be that the propeller slipstream increased the effective angle of attack (α_{eff}). As J increased, the propeller's influence decreased, causing a decrease in $\Delta\psi_L$ and $\Delta\psi_M$ to almost 0°. At lower propeller thrust conditions, $\Delta\psi_L$ and $\Delta\psi_M$ were small and nearly negligible, but at higher propeller thrust conditions, the phase shift changes induced by the propeller are no longer negligible.

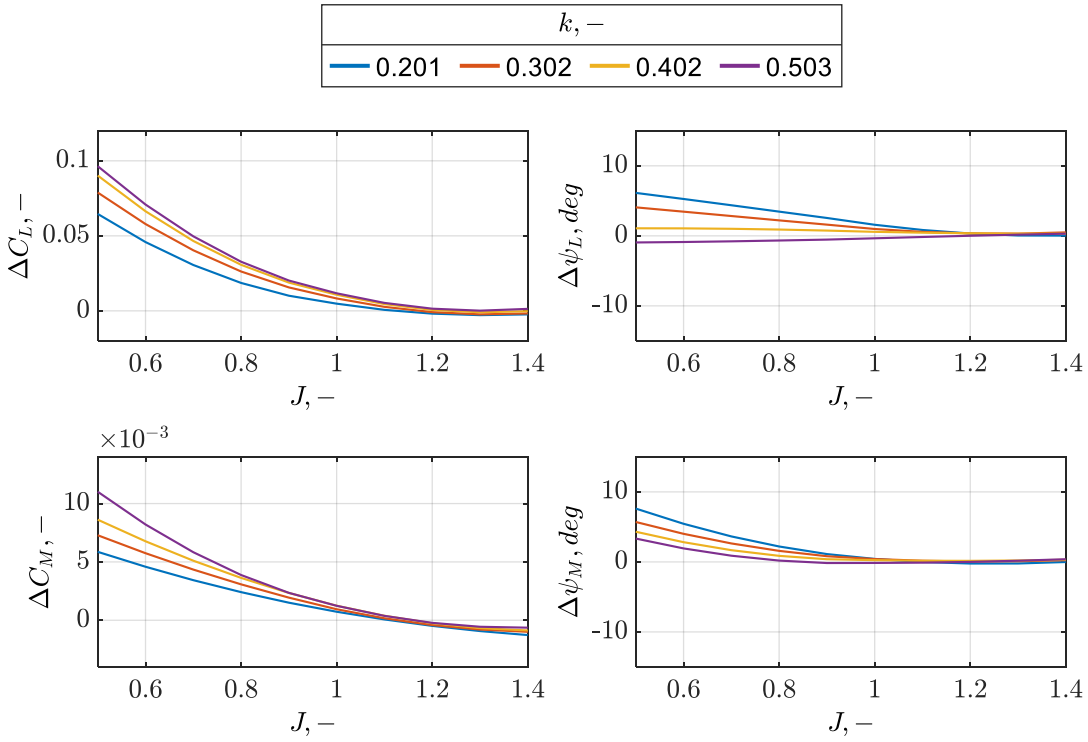

Figure 6-5: *Veldhuis Wing* (+ *Propeller 1*, NACA 64_2-a015, Pitching motion) – Rigid propeller-wing attachment vs Standalone wing: *k* comparison, *J* variation; α_{WMax} = 4°

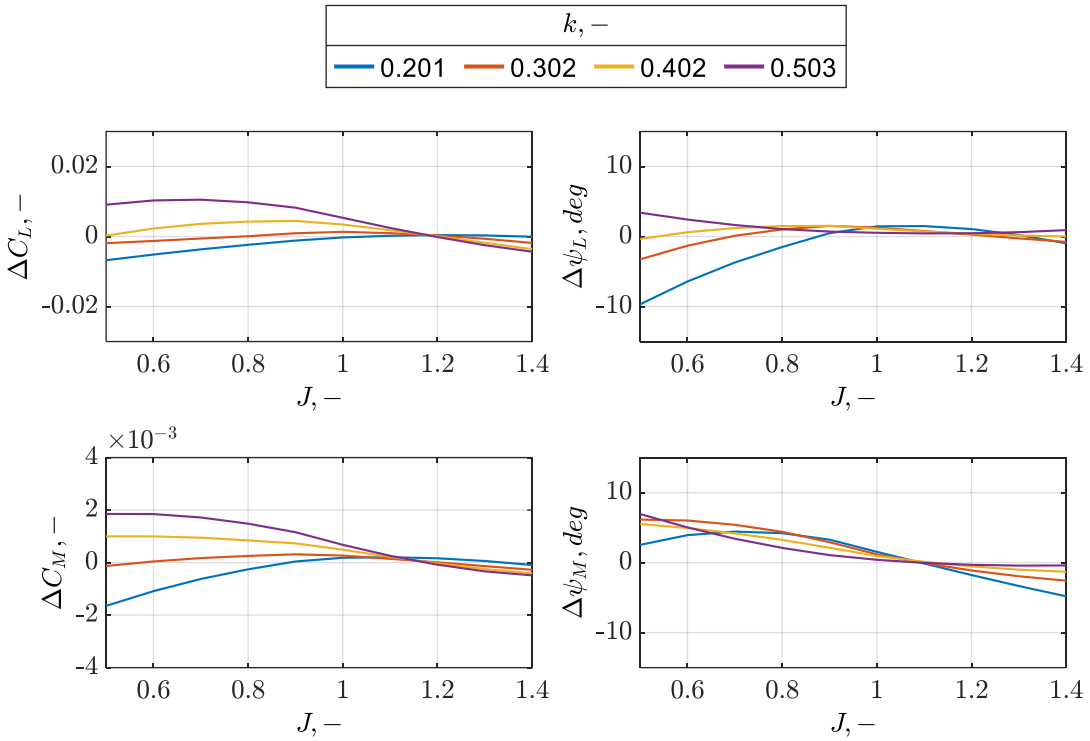

Figure 6-6: *Veldhuis Wing* (+ *Propeller 1*, NACA 64_2-a015, Plunging motion) – Rigid propeller-wing attachment vs Standalone wing: *k* comparison, *J* variation; *h* = 0.05

6.2 Wing with Flexibly Attached Propeller

In chapter 6.2, the effects of a rigidly attached propeller on a pure-pitching and pure-plunging wing were studied. In this chapter, the effects of flexibility in the propeller-wing attachment to the aerodynamic performance of a pure-pitching and pure-plunging wing were studied. The *Veldhuis Wing* and *Propeller 1* models were re-used for the simulations and the fixed model and simulation settings are provided in Table 6-1. To introduce flexibility to the wing-propeller attachment, a phase shift (φ_P) between the motions of the wing and propeller and a pitching amplitude ($\alpha_{P_{Max}}$) relative to the wing was added. To avoid complexities, the pitching frequency of the propeller was kept the same as the pitching/plunging frequency of the wing (ω). The equation of propeller motion in the wing's reference frame ($\alpha_{P\to W}$) is given in 6.1.

$$\alpha_{P\to W}(t) = \alpha_{P\to W_0} + \alpha_{P_{Max}} \sin(\omega t + \varphi_P) \qquad 6.1$$

For all the simulations, α_{MaxP} was kept small to remain in the linear aerodynamics region, i.e. $1° \leq \alpha_{P_{Max}} \leq 4°$ and was also compared to the rigid propeller case ($\alpha_{P_{Max}} = 0°$). φ_P was varied from -180° to 180° where $\varphi_P < 0°$ indicates a phase lag of the propeller motion with respect to the wing motion while $\varphi_P > 0°$ indicates a phase lead of the propeller motion with respect to the wing motion. It is also ensured that the initial angle of attack of the propeller with respect to the wing in

the wing reference frame ($\alpha_{P\rightarrow W_0}$) is always 0°. The pitching wing's motion w.r.t the wing's motion is shown in Figure 6-7.

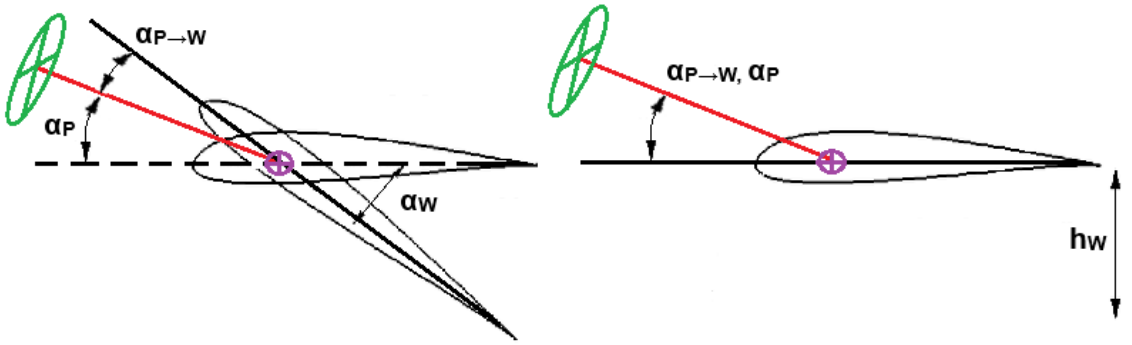

Figure 6-7: Propeller pitching motion relative to the pitching wing (Left) and plunging wing (Right)

It must be noted that while introducing a phase shift and amplitude modulation between the wing and propeller can simulate some aspects of a flexible attachment, such as delayed response and reduced motion, it is not sufficient to fully mimic the aerodynamic response of a truly flexible propeller-wing attachment. This approach is useful for capturing basic trends and linear effects, but it will not account for the more complex, non-linear, and frequency-dependent interactions that characterise a flexible system.

FMI simulations were performed on the *Veldhuis Wing + Propeller 1* model used in the aerodynamic interaction study of a rigidly attached propeller's influence (see chapter 6.1). The fixed model and simulation parameters are provided in Table 6-1. The results of these simulations were compared to the results obtained from the rigidly attached propeller study.

For the pitching wing case, three combinations of $\alpha_{W_{Max}}$ and k were chosen:

a. $\alpha_{W_{Max}} = 2°; k = 0.302$,
b. $\alpha_{W_{Max}} = 4°; k = 0.302$ and
c. $\alpha_{W_{Max}} = 4°; k = 0.402$.

For the plunging wing case, three combinations of h and k were chosen:

d. $h = 0.05; k = 0.302$,
e. $h = 0.05; k = 0.402$ and
f. $h = 0.1; k = 0.302$.

These sets of cases were selected to study the influence of both pitching/plunging amplitude (amp_{Max}) and reduced frequency (k) by keeping one of them constant between two sets of simulations (k fixed, amp_{Max} varying between sets (a, b) and (d, f); amp_{Max} fixed, k varying between sets (b, c) and (d, e)). The phase difference between the wing and the propeller was varied for all possible values ($-180° \leq \varphi_P \leq 180°$) to study the influence of the propeller's orientation w.r.t the wing. To study the influence of the pitching amplitude of the propeller, the amplitude ratio of the propeller w.r.t the wing ($\alpha_{P_{Max}}/amp_{Max}$) was varied.

$\alpha_{P_{Max}}/amp_{Max} = 0$ represented a rigidly attached propeller, while $\alpha_{P_{Max}}/amp_{Max} > 0$ represented a flexibly attached propeller. The complete simulation parameters are provided in Table 6-4.

Table 6-4: *Veldhuis Wing* (+ *Propeller 1*, NACA 64_2-a015) – Simulation settings: Flexible wing-propeller attachment study, propeller phase (φ_P) variation

Parameter (Fixed)	Value
Advance ratio $(J, -)$	0.9
Parameter (Varying)	**Range**
Wing pitch amplitude $(\alpha_{W_{Max}}, deg)$	2, 4
Normalised plunge amplitude $(h, -)$	0.05, 0.1
Reduced frequency $(k, -)$	0.302, 0.402
Propeller pitch amplitude $(\alpha_{P_{Max}}, deg)$	0, 1, 2, 4
Propeller phase offset (φ_P, deg)	-180, -150, …., 150, 180

The lift and moment transfer functions with $\alpha_{P_{Max}}/\alpha_{W_{Max}} = 0{,}0.5{,}1.0$ have been plotted in Figure 6-8 for the pitching wing case, while the lift and moment transfer functions with $\alpha_{P_{Max}}/h = 0{,}20{,}40$ have been plotted in Figure 6-9 for the plunging wing case. In both figures, each contour formed represents a fixed wing operating condition, i.e. a fixed amp_{Max} and k, and varying φ_P. Four different φ_P values were chosen and represented with different markers to provide more information regarding the shape and orientation of the formed contours.

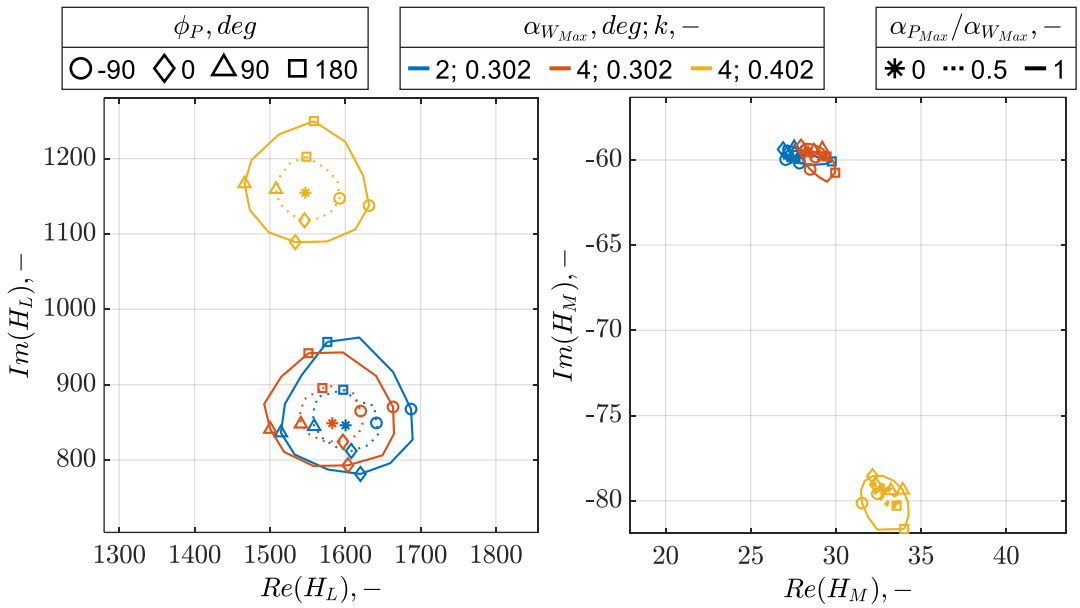

Figure 6-8: *Veldhuis Wing* (+ *Propeller 1*, NACA 64_2-a015, Pitching motion) – Flexible propeller-wing attachment vs Rigid propeller-wing attachment: α_{PMax} and φ_P variation, Complex plane representation

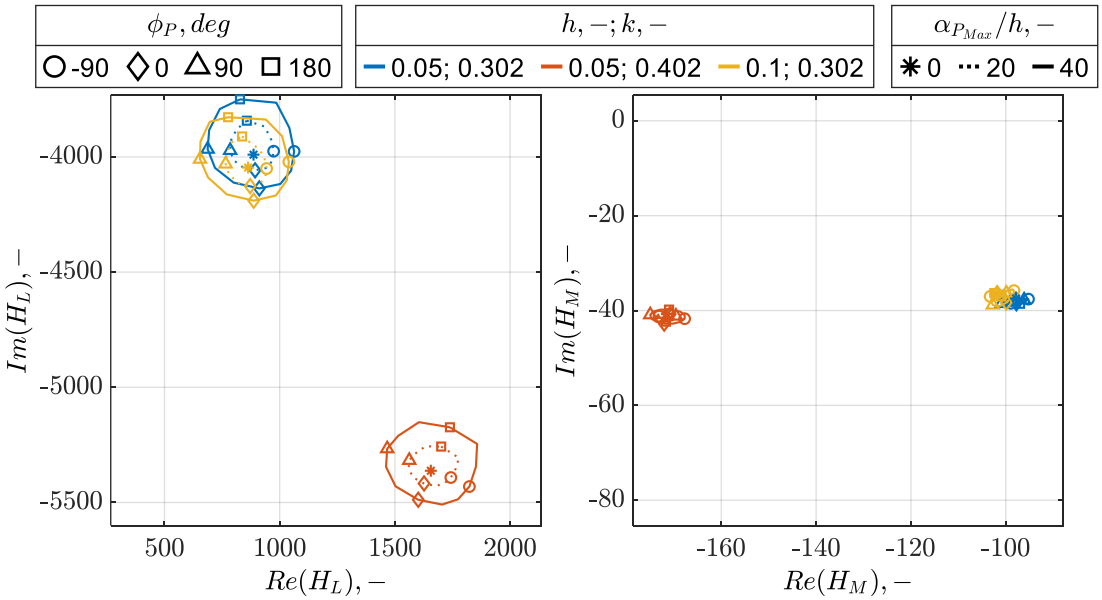

Figure 6-9: *Veldhuis Wing* (+ *Propeller 1*, NACA 64$_2$-a015, Plunging motion) – Flexible propeller-wing attachment vs Rigid propeller-wing attachment: α_{PMax} and φ_P variation, Complex plane representation

From Figure 6-8 and Figure 6-9, it could be observed that introducing a pitching amplitude and phase shift between the propeller and the wing (at small values of amp_{Max} and k) gave rise to a small variation in H_L and H_M, i.e. a small change in the overall system behaviour. Different $\alpha_{P_{Max}}$ values alter the natural frequencies and damping ratios while different values of φ_P leads to constructive/destructive interference between the propeller-induced flow and the wing-induced flow, resulting in the observed contour shapes. The lift transfer function contours for the chosen values of amp_{Max} and k were nearly circular in shape whereas the moment transfer function contours were elliptical. All the contours were formed clockwise for an increase in φ_P but their orientations differed.

The size of the contours was nearly proportional to the amplitude ratio ($\alpha_{P_{Max}}/amp_{Max}$). The contours were also concentric, with the centre of these contours roughly being the transfer function of the rigidly attached propeller case. This means that at a given frequency, the variation in magnitude of the lift and moment transfer functions is proportional to the ratio of the pitching amplitude of the propeller to the pitching/plunging amplitude of the wing, i.e. the variation in magnitude of the lift and moment forces is proportional to the pitching amplitude of the propeller, indicating that the aerodynamic response of the system is linear. The deviations in the moment contour shapes were due to the oscillations in the moment forces by the blade rotations, causing a variation in the FFT output. This was also observed in the rigidly attached propeller study (chapter 6.1). At larger oscillating frequencies, these deviations may reduce or even vanish as the moment contours for the larger reduced frequency cases are less elliptical and less skewed compared to the moment contours at lower reduced frequencies.

For a variation in amp_{Max}, the contours were nearly equal in size with little to no change in their orientation. The negligible change in orientation indicated that at a given k, the propeller has the same influence on the transfer function for the same φ_P. For a variation in k, the lift transfer function contours appeared to be slightly larger for a higher k. The orientation of the contours also appeared to be rotated clockwise for a higher k. The slight increase in size could be explained by the fact that the unsteady aerodynamic effects due to the propeller are amplified for larger frequencies.

While a change in amp_{Max} did not produce significant changes in the H_L contours and the changes in the H_M contours are primarily due to the sensitivity of the FFT function to noise in the signal, a change in k warranted further investigation. For the next set of FMI simulations performed on the flexibly attached propeller model, the amplitude ratio was fixed while k was varied. 4 different values of φ_P were chosen ($\varphi_P = -90°, 0°, 90°, 180°$), while keeping the pitching/plunging amplitudes fixed for the wing ($\alpha_{W_{Max}} = 4°, h = 0.05$) and propeller ($\alpha_{P_{Max}} = 4°$). The complete simulation parameters have been provided in Table 6-5.

Table 6-5: *Veldhuis Wing* (+ *Propeller 1*, NACA 64_2-a015) – Simulation settings: Flexible wing-propeller attachment study, *k* variation

Parameter (Fixed)	**Value**
Advance ratio ($J, -$)	0.9
Wing pitch amplitude ($\alpha_{W_{Max}}, deg$)	4
Normalised plunge amplitude ($h, -$)	0.05
Propeller pitch amplitude ($\alpha_{P_{Max}}, deg$)	4
Parameter (Varying)	**Range**
Reduced frequency ($k, -$)	0.101, ….,1.005
Propeller phase offset (φ_P, deg)	-90, 0, 90, 180

In Figure 6-10 and Figure 6-11, the (lift and moment) transfer functions have been plotted for the pitching wing and plunging wing cases respectively. Additionally, the transfer functions for the rigidly attached propeller model ($\alpha_{P_{Max}}/amp_{Max} = 0$) were calculated and plotted for the same k range. The rigidly attached propeller transfer functions are represented by purple stars. Each marker represents the transfer function calculated for a unique k and φ_P. Each colour represents a different φ_P, while each solid line represents the variation in the transfer function between the rigid case and the flexible case for a given k and φ_P.

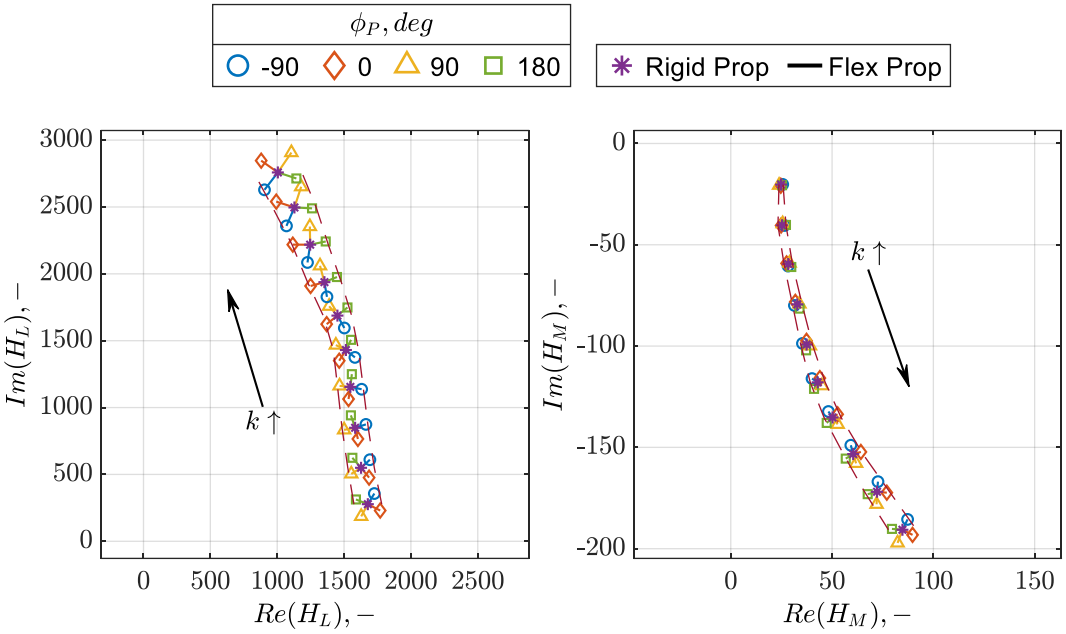

Figure 6-10: *Veldhuis Wing* (+ *Propeller 1*, NACA 64_2-a015, Pitching motion) – Flexible propeller-wing attachment vs Rigid propeller-wing attachment: *k* variation, Complex plane representation

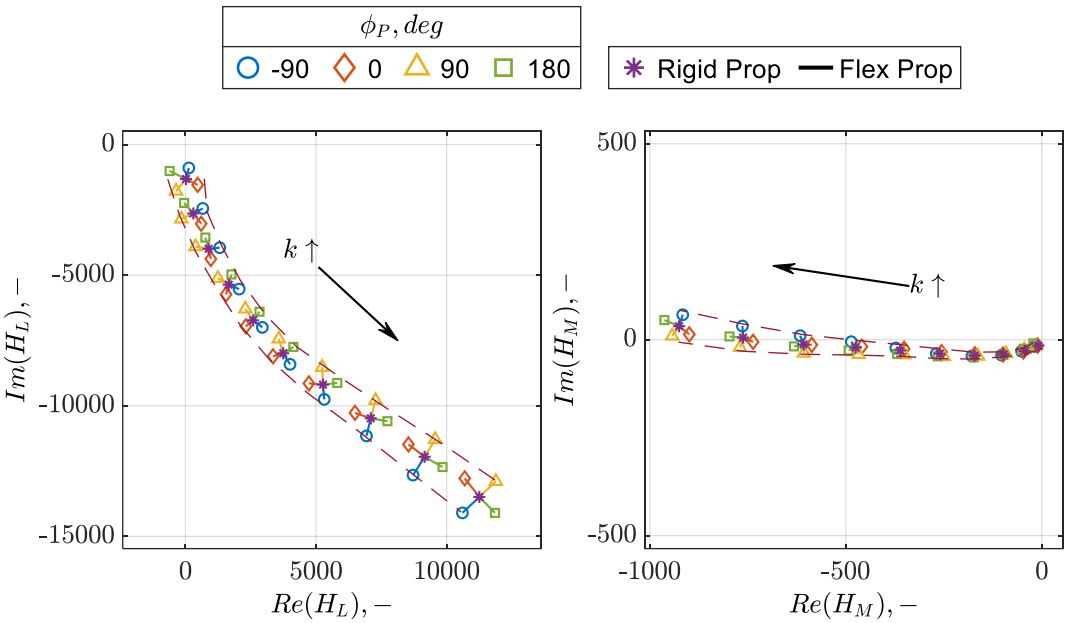

Figure 6-11: *Veldhuis Wing* (+ *Propeller 1*, NACA 64_2-a015, Plunging motion) – Flexible propeller-wing attachment vs Rigid propeller-wing attachment: *k* variation, Complex plane representation

It was observed that for a given k, the lines between the rigidly attached propeller transfer functions and the flexibly attached propeller transfer functions were nearly equal in length, indicating that the magnitude of the variations in the lift and moment transfer functions are independent of φ_P. For a given k, the -90°, 0°, 90° and 180° lines are separated in the clockwise direction by an angle nearly equal to φ_P itself. This indicates that for a given k, the variations in the real and imaginary components of the transfer functions oscillate w.r.t φ_P, i.e. the

aerodynamic system has a constant total energy response, where the sum of damping and stiffness effects is independent of φ_P.

The lines became longer and rotated clockwise for an increase in k. The increase in the length of the lines was because higher pitching and plunging frequencies of the wing amplify the effects of the propeller on the wing to a greater extent. This could also be visualised clearly in the increase in the width of the bands drawn for both H_L and H_M. These bands (represented by dashed lines in Figure 6-10 and Figure 6-11) indicated the maximum variations in the real component of the transfer functions. Since the lines at a given k were equal in length irrespective of φ_P, the bands also indicated the maximum variation in the imaginary component of the transfer functions. This implies that for a fixed amplitude ratio ($\alpha_{P_{Max}}/amp_{Max}$), as k increases, the system has a larger aerodynamic response.

The clockwise rotations of the lines for an increase in k indicated that the imaginary component of the transfer functions leads the real component. In terms of the aerodynamic response of the system, the clockwise rotation suggests that the aerodynamic response of the system leads the motion of the system. The real and imaginary components (of the lift and moment transfer functions) correspond to aerodynamic stiffness and the aerodynamic damping characteristics of the system respectively, which means that the influence of damping becomes more pronounced compared to the aerodynamic stiffness.

The width of the H_M band increased at a faster rate as compared to the H_L band width, indicating that the moment forces are more sensitive to the pitching/plunging frequency of the wing.

6.3 Summary

The influence of a rigidly attached propeller to a wing in a tractor, in-line configuration can be summarised by:

1. Positive thrust coefficients of the propeller have a positive influence on the lift and moment forces and phase shifts, with an increase in the advance ratio (J) of the propeller diminishing the influence of the propeller and causing a decrease in the lift and moment forces and phase shifts. At near windmilling conditions, the propeller has no influence on the wing's aerodynamic performance.
2. Larger pitching/plunging amplitudes amplify the unsteady aerodynamic effects, causing a larger variation in the lift and moment forces (ΔC_L and ΔC_M). ΔC_L and ΔC_M are nearly proportional to the pitching/plunging amplitude (amp_{Max}). For an increase in k, a peak value can be observed in the ΔC_L and ΔC_M values. The presence of a peak indicates a resonance-like behaviour where the aerodynamic response is maximised. At certain frequencies, the

unsteady aerodynamic forces caused by the wing's pitching motion are in phase with the additional velocity field induced by the propeller wake. This phasing can cause constructive interference, leading to a significant increase in the aerodynamic forces and moments.

3. In comparison to the ΔC_L and ΔC_M values in the pitching case, the ΔC_L and ΔC_M values are more pronounced in the plunging case, implying that the propeller's influence is more substantial when the wing undergoes larger vertical displacements.
4. For a given k, the variations in the lift and moment phase shifts ($\Delta\psi_L$ and $\Delta\psi_M$) are nearly equal for small pitching/plunging amplitudes (amp_{Max}). At lower propeller thrust conditions, $\Delta\psi_L$ and $\Delta\psi_M$ are small and nearly negligible, but at higher propeller thrust conditions, the phase shift changes induced by the propeller are no longer negligible.

The addition of a phase shift and a pitching amplitude between the propeller and the wing can be summarised by:

1. For a given k, the aerodynamic response of the system is proportional to the amplitude ratio of the propeller w.r.t the wing ($\alpha_{P_{Max}}/amp_{Max}$), i.e. the response of the system is linear.
2. For a given k, the aerodynamic response of the system to the phase difference between the wing and the propeller (φ_P) is linear, meaning that the aerodynamic system has a constant total energy response, where the sum of damping and stiffness effects is independent of φ_P.
3. For a given $\alpha_{P_{Max}}/amp_{Max}$, as k increases, the aerodynamic response of the system increases as larger oscillating frequencies of the wing amplify the effects of the propeller to a greater extent.
4. As k increases, the system's aerodynamic response begins to exhibit a phase lead w.r.t the system’s motion, meaning that the aerodynamic forces and moments start to respond earlier relative to the input motion. This phase lead suggests that the influence of aerodynamic damping becomes more significant compared to aerodynamic stiffness.
5. The more substantial increase in the moment force compared to the lift force indicates that the aerodynamic moment is more sensitive to the wing oscillation frequency compared to the aerodynamic lift.

7 Aerodynamic Investigation of Propeller-Wing Interaction: Complex Wing Modes

In the previous chapter, the effects of the propeller on a pure-pitching and pure-plunging wing were studied. The natural mode shapes of a wing are a combination of these two motions. While the propeller is expected to influence aeroelastic components as well as introduce gyroscopic effects, the focus of this chapter was simply on the aerodynamic influence of the propeller on the wing.

7.1 Model Description

The wing model used for these studies was the *Goland Wing* with the model details provided in Table 4-5. The model settings of the propeller model (*Propeller 2*) chosen for these studies are given in Table 7-1. The performance curve of the propeller has been depicted in Figure 7-1 at $u_\infty = 50ms^{-1}$, while the radial thrust distribution of the propeller at $J = 1.2$ and $u_\infty = 50ms^{-1}$ has been depicted in Figure 7-2.

Table 7-1: *Propeller 2* – Model description: Wing-propeller interaction validation study

Parameter	Value
Airfoil	NACA 0012
Number of Blades	4
Propeller radius (R, m)	0.762
Propeller chord (c_P, m)	0.1863
Propeller twist (θ_P, deg)	32.71
Propeller blade pitch angle $(\beta_{0.75}, deg)$	34

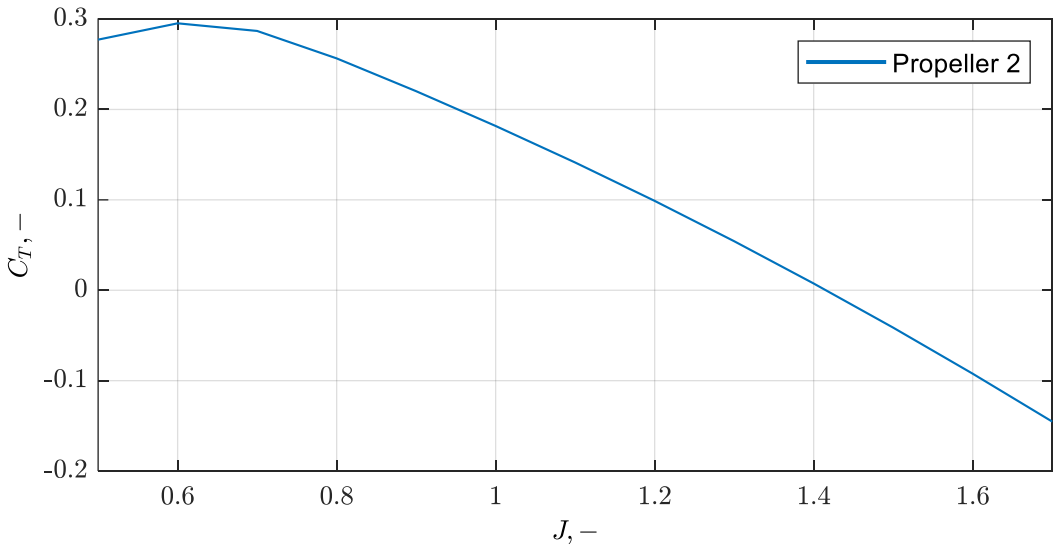

Figure 7-1: *Propeller 2* – C_T vs J, u_∞ = 50ms^{-1}

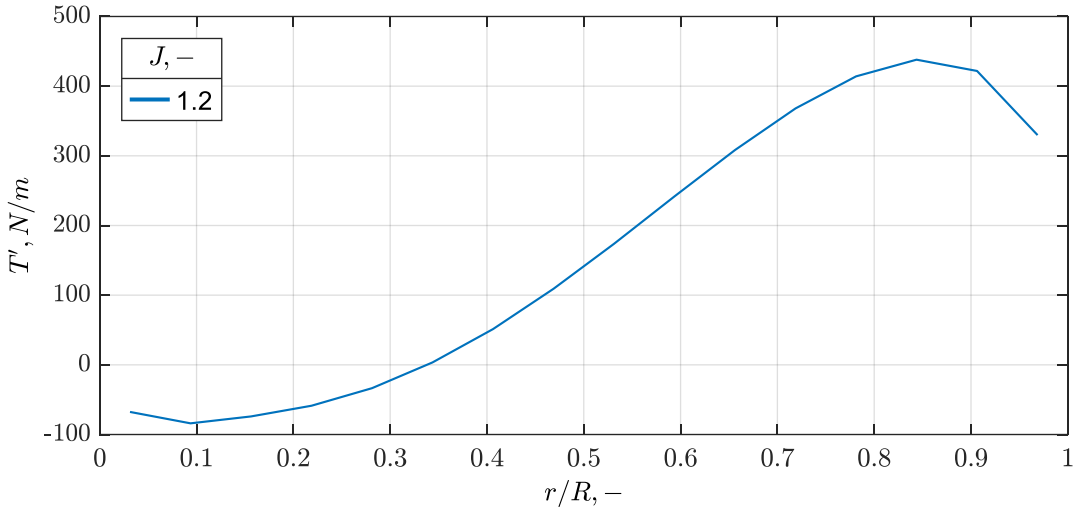

Figure 7-2: *Propeller 2* – Radial thrust distribution, J = 1.2, u_∞ = 50ms^{-1}

7.2 Simulation Settings

In this chapter, FMI simulations were performed on the *Goland Wing* for the 1st bending and 1st torsional modes. The scaling factor ($amp_{Max} = 0.1$) and thrust coefficient ($C_T = 0.1$) chosen helped in capturing the significant dynamic interactions without introducing non-linear effects that were more challenging to analyse. u_∞ was also kept low to create a realistic scenario for low speed aeroelastic analysis. The influence of k on a mid-wing ($y_P/b_W/2 = 0.5$), outboard ($y_P/b_W/2 = 0.75$) and wingtip ($y_P/b_W/2 = 1.0$) propeller was studied and compared. The complete simulation settings are provided in Table 7-2.

Table 7-2: *Goland Wing* (+ *Propeller 2*) – Simulation settings: Wing-propeller interaction validation study

Parameter (Fixed)	Value
Freestream velocity (u_∞, ms^{-1})	1.225
Freestream density (ρ_∞, kgm^{-3})	50.0
Scaling factor ($amp_{Max}, -$)	0.1
Rotation direction	IU
Advance ratio ($J, -$)	1.2
Propeller thrust coefficient ($C_T, -$)	0.1
Normalised Z-position ($z_P/R\,, -$)	0.0
Normalised X-position ($x_P/c_W\,, -$)	-0.5
Parameters (Varying)	**Range**
Wing Modes	1st Bending, 1st Torsion
Reduced frequency ($k, -$)	0.05, …., 1.0
Normalised Y-position ($y_P/b_W/2\,, -$)	0.5, 0.75, 1.0

7.3 Results and Discussion

From the time histories of the lift and moment forces obtained from the FMI simulations, the differences in the maximum lift and moment coefficients ($\Delta C_L, \Delta C_M$) and phase shifts ($\Delta\psi_L, \Delta\psi_M$) between the wing-propeller system and the standalone wing were compared at different k. The lift and moment coefficients and phase shifts for the first 4 bending modes were already calculated and presented in Figure 4-8. Three different spanwise locations of the propeller were chosen:

a) mid-wing ($y_P/b_W/2 = 0.5$),
b) outboard ($y_P/b_W/2 = 0.75$) and
c) wingtip ($y_P/b_W/2 = 1.0$).

While the aerodynamic interaction study of a wing undergoing simple motions was done for a fixed mid-wing spanwise location, and a spanwise parameter study was not conducted, the results from this chapter were simply meant to be presented without going into too much detail, but aerodynamic performance variations were to be expected, especially for the tip-mounted propeller configuration.

The lift and moment coefficient variations ($\Delta C_L, \Delta C_M$) and phase shifts variations (($\Delta\psi_L, \Delta\psi_M$) to the standalone wing were done for the 1st bending mode in Figure 7-3, and for the 1st torsional mode in Figure 7-4:

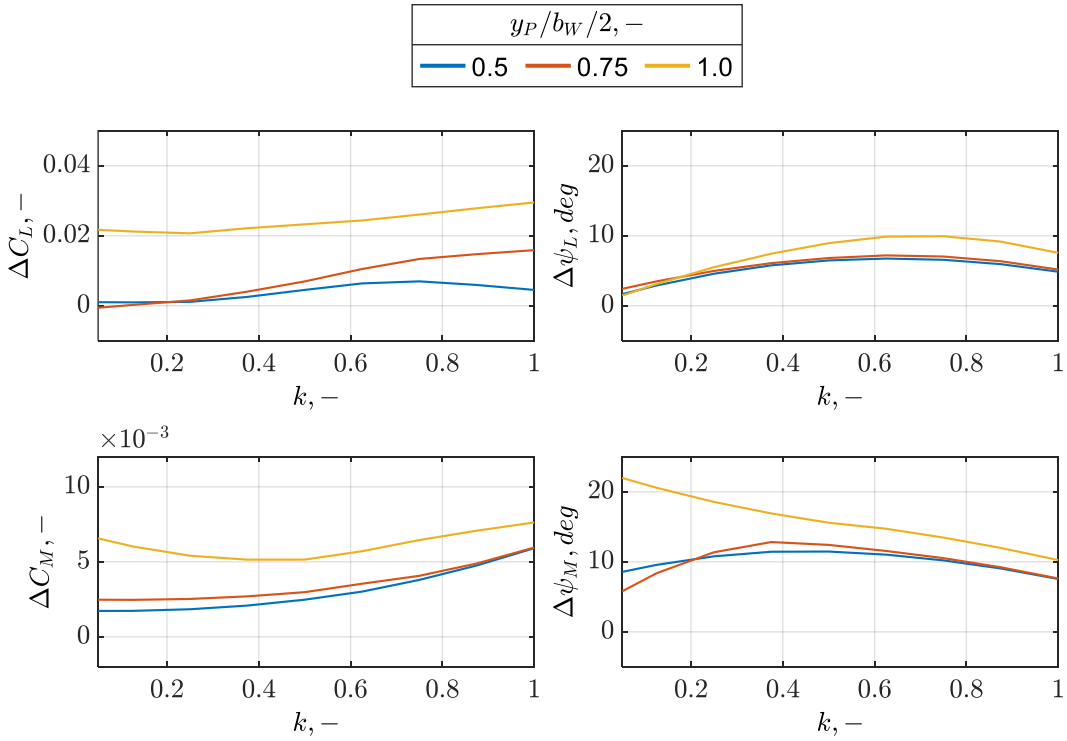

Figure 7-3: *Goland Wing* (+ *Propeller 2*, 1st bending mode) – Rigid propeller-wing attachment vs Standalone wing: $y_P/b_W/2$ comparison, k variation

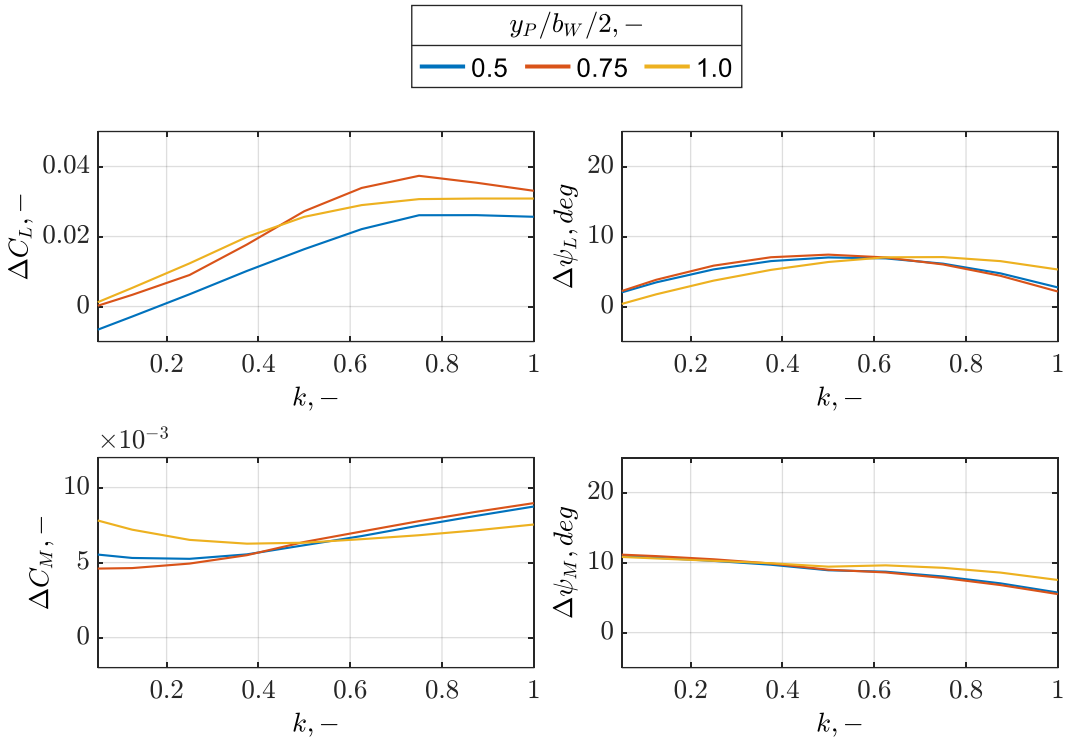

Figure 7-4: *Goland Wing* (+ *Propeller 2*, 1st torsion mode) – Rigid propeller-wing attachment vs Standalone wing: $y_P/b_W/2$ comparison, *k* variation

In all cases, the propeller had a positive influence on the wing's lift and moment forces, which was expected for a thrusting propeller (chapter 6.1), with similar trends in the lift and moment coefficients and phase shifts, as seen in Figure 6-4. All cases indicated an increase in the lift and moment phase shifts.

At inboard positions of the propeller ($y_P/b_W/2 = 0.5,0.75$), there were little to no deviations in the trends observed whereas there were larger deviations in the trends observed for the wingtip mounted propeller configuration ($y_P/b_W/2 = 1.0$). The deviations in the torsional wing mode were small while the deviations in the bending wing mode were larger and could not be neglected:

a) In the bending wing mode case, the wingtip mounted propeller increased the lift and moment forces to a greater extent compared to the propeller at inboard positions. While this observation agreed with the spanwise propeller position validation studies performed in chapter 5.1.2 (Figure 5-11), this was surprisingly not observed in the torsional wing mode case.

b) A very large deviation in the $\Delta\psi_M$ trend could be seen for the wingtip mounted propeller position in the bending wing mode case: At lower k values, $\Delta\psi_M$ was very large, but $\Delta\psi_M$ decreased for an increase in k and the deviation vanished at higher k values.

8 Conclusions and Outlook

In this thesis, the aerodynamic interactions between a propeller and a wing were investigated under various configurations and motion scenarios. The main contributions and findings of the research are as follows:

Fluid-Motion Interaction (FMI) simulations consist of prescribed motions assigned to a model and obtaining a response to these motions from an aerodynamic solver, in contrast to Fluid-Structure Interaction (FSI) simulations which are used to observe the structural response of a system. FMI simulations allow for motion response studies while avoiding the need to solve MDoF motion equations. The in-house motion solver allows for performing FMI simulations while enabling the creation of reference frames and prescribed motions for desired and pre-existing models. The maximum time spent by the solver (+adapter) between reading and writing data for a single time step was 0.2s and the maximum time for calculating the prescribed motions for one simulation was 1min, which displayed its efficacy.

The performance and properties of the propeller wake were first validated. The results obtained agreed with existing research. The propeller wake acted as a continuous band of maximum dynamic pressure downstream of the propeller, with the band located between 70% and 90% of the radius of the propeller. As the propeller rotational speed decreased, the thrust produced by the propeller also decreased. Using Veldhuis' thesis as a benchmark, the interaction between a stationary wing and a propeller was validated. The results corroborate existing research, demonstrating accurate predictions of lift and (inviscid) drag coefficients. The propeller rotation direction had an influence on the lift force and lift distribution on the wing, with inboard-up (IU) rotating propellers typically having a more positive influence compared outboard-up (OU) rotating propellers. An increase in the advance ratio of the propeller led to a decrease in the lift force of the wing. While positive thrust coefficients of the propeller typically have a positive influence on the lift force of the wing, there were certain advance ratios at which the propeller was thrusting, yet the wing lift was lower than that of the standalone wing, indicating that the wing also influences the propeller aerodynamics. An increase in the spanwise position of the (IU rotating) propeller led to a minor increase in the lift and a large decrease in the inviscid drag. This could be attributed to the propeller rotating in the opposite direction of the wingtip vortices, resulting in an increase in the effective aspect ratio of the wing and hence, a decrease in the induced drag. A propeller at higher inclinations w.r.t the wing led to a decrease in lift and an increase in drag, which could be attributed to a decrease in the vertical and horizontal loading vectors on the wing.

Validation studies were performed between wing models with varying airfoil sections across the different models, with a comparison to results obtained from Theodorsen’s Unsteady Thin Airfoil Theory, demonstrating accuracy in simulating

pitching and plunging motions of wings. At small pitching and plunging amplitudes ($\alpha_{W_{Max}} \leq 4°$; $h \leq 0.1$) and low to moderate reduced frequencies ($0.1 \leq k \leq 1.0$), flow behaviour around the wing was independent of the magnitude of pitching/plunging amplitude but was highly dependent on the reduced frequency. A deviation was observed in the flow behaviour of the wing models when compared to the theoretical values, with the deviations growing larger for an increase in airfoil thickness. Differences primarily arose due to 3-dimensional effects and deviation of the airfoil shape from a flat plate shape.

The first four natural frequencies of the Goland wing were calculated to be 7.65 Hz, 15.21 Hz, 38.63 Hz, and 54.89 Hz, which were within 4% of existing research values. Simulations of these modes provided insight into the dynamic lift and moment coefficients, highlighting the wing's dynamic behaviour under these conditions. The 1st and 2nd natural modes of the Goland wing were bending dominated and torsional dominated respectively and observed large variations in the lift and moment forces for a change in the wing's oscillating frequency. The 3rd and 4th natural modes of the Goland wing were both bending and torsional dominated and observed smaller variations in the lift and moment forces compared to the bending dominated and torsional dominated cases.

Positive thrust coefficients of the propeller had a positive influence on the lift and moment forces and phase shifts, with an increase in the advance ratio (J) of the propeller diminishing the influence of the propeller and causing a decrease in the lift and moment forces and phase shifts. At near windmilling conditions, the propeller has no influence on the wing's aerodynamic performance. Larger pitching/plunging amplitudes amplified the unsteady aerodynamic effects, causing a larger variation in the lift and moment forces (ΔC_L and ΔC_M). ΔC_L and ΔC_M were nearly proportional to the pitching/plunging amplitude (amp_{Max}). For an increase in k, a peak value could be observed in the ΔC_L and ΔC_M values. The presence of a peak indicated a resonance-like behaviour where the aerodynamic response was maximised. At certain frequencies, the unsteady aerodynamic forces caused by the wing's pitching motion are in phase with the additional velocity field induced by the propeller wake. This phasing can cause constructive interference, leading to a significant increase in the aerodynamic forces and moments. In comparison to the ΔC_L and ΔC_M values in the pitching case, the ΔC_L and ΔC_M values were more pronounced in the plunging case, implying that the propeller's influence was more substantial when the wing undergoes larger vertical displacements. For a given k, the variations in the lift and moment phase shifts ($\Delta\psi_L$ and $\Delta\psi_M$) were nearly equal for small pitching/plunging amplitudes (amp_{Max}). At lower propeller thrust conditions, $\Delta\psi_L$ and $\Delta\psi_M$ were small and nearly negligible, but at higher propeller thrust conditions, the phase shift changes induced by the propeller were no longer negligible.

For a given k, the aerodynamic response of the system was proportional to the amplitude ratio of the propeller w.r.t the wing ($\alpha_{P_{Max}}/amp_{Max}$), i.e. the response of the system was linear. For a given k, the aerodynamic system's response to the phase difference between the wing and the propeller (φ_P) was linear, meaning that the aerodynamic system had a constant total energy response, where the sum of damping and stiffness effects was independent of φ_P. For a given $\alpha_{P_{Max}}/amp_{Max}$, as k increased, the aerodynamic response of the system increased as larger oscillating frequencies of the wing amplified the effects of the propeller to a greater extent. As k increased, the system's aerodynamic response began to exhibit a phase lead w.r.t the system's motion, meaning that the aerodynamic forces and moments started to respond earlier relative to the input motion. This phase lead suggests that the influence of aerodynamic damping became more significant compared to aerodynamic stiffness. The more substantial increase in the moment force compared to the lift force indicated that the aerodynamic moment was more sensitive to the wing oscillation frequency compared to the aerodynamic lift.

In all the simulations performed on the flexible wing model undergoing its natural mode shapes, attached with a thrusting propeller, the propeller had a positive influence on the wing's lift and moment forces. At inboard positions of the propeller ($y_P/b_W/2 = 0.5,0.75$), there were little to no deviations in the trends observed whereas there were larger deviations in the trends observed for a wingtip mounted propeller ($y_P/b_W/2 = 1.0$). The deviations in the torsional wing mode were small while the deviations in the bending wing mode are larger and could not be neglected. In the bending wing mode case, the wingtip mounted propeller increased the lift and moment forces to a greater extent compared to the propeller at inboard positions. While this observation agrees with the spanwise propeller position validation studies, this was surprisingly not observed in the torsional wing mode case. A very large deviation in the $\Delta\psi_M$ trend could be seen for the wingtip mounted propeller position in the bending wing mode case: At lower k values $\Delta\psi_M$ was very large, but $\Delta\psi_M$ decreased for an increase in k and the deviation vanished at higher k values.

The research conducted in this thesis has provided valuable insights into the complex aerodynamic interactions between a propeller and a wing, especially under various configurations and dynamic motion scenarios. However, this study also opens several avenues for future research that could further enhance our understanding and practical application of these interactions.

While this thesis focused primarily on conventional propeller-wing arrangements, future studies could explore more advanced configurations, such as distributed propulsion systems or unconventional propeller placements (e.g., along the wingspan and chord). These studies could provide critical data on how such

configurations might optimise aerodynamic efficiency, reduce drag, or enhance lift under different flight conditions.

While this study focused on the first bending and torsion modes of a flexible wing, future research could extend to higher-order modes and more complex deformation patterns. Investigating how these additional modes interact with the propeller's wake could provide deeper insights into the aeroelastic behaviour of advanced wing designs.

Building on the insights gained from introducing phase shifts and amplitude differences between the propeller and wing, future research could further investigate the potential of phase and amplitude modulation as a simplified method for mimicking the behaviour of flexible propeller-wing attachments. By systematically varying these parameters and comparing the results with more comprehensive aeroelastic models, researchers could determine the extent to which these simplified techniques can replicate complex aerodynamic interactions. This approach could serve as a valuable tool for preliminary design studies, allowing for quicker assessments of flexible system behaviours before engaging in more resource-intensive simulations or experiments.

While the computational models developed in this thesis were validated against existing theoretical and research data, further experimental validation through wind tunnel testing or flight trials would be instrumental in confirming the accuracy of the simulations. Such validation could also help refine the models to better predict real-world aerodynamic behaviour.

The current study utilised a partitioned FMI simulation technique to model the interactions between the propeller and wing. Future work could incorporate more advanced computational techniques, such as including structural variables and even introduce gyroscopic effects to combine FSI and FMI simulations, to capture the full range of dynamic effects. This approach could lead to a more accurate prediction of aeroelastic phenomena like flutter and divergence under various operating conditions.

9 References

[1] R. de Vries and R. Vos, "Aerodynamic Performance Benefits of Over-the-Wing Distributed Propulsion for Hybrid-Electric Transport Aircraft," *Journal of Aircraft*, vol. 60, no. 4, pp. 1201–1218, 2023, doi: 10.2514/1.C036909.

[2] P. Della Vecchia, D. Malgieri, F. Nicolosi, and A. de Marco, "Numerical analysis of propeller effects on wing aerodynamic: tip mounted and distributed propulsion," *Transportation Research Procedia*, vol. 29, pp. 106–115, 2018, doi: 10.1016/j.trpro.2018.02.010.

[3] T. Sinnige, N. van Arnhem, T. C. A. Stokkermans, G. Eitelberg, and L. L. M. Veldhuis, "Wingtip-Mounted Propellers: Aerodynamic Analysis of Interaction Effects and Comparison with Conventional Layout," *Journal of Aircraft*, vol. 56, no. 1, pp. 295–312, 2019, doi: 10.2514/1.C034978.

[4] L. L. M. Veldhuis, *Propeller wing aerodynamic interference*. [S.l.]: [s.n.], 2005.

[5] E. A. Marcus, R. de Vries, A. Raju Kulkarni, and L. L. Veldhuis, "Aerodynamic Investigation of an Over-the-Wing Propeller for Distributed Propulsion," in *2018 AIAA Aerospace Sciences Meeting*, Kissimmee, Florida, 2018.

[6] J. A. Cole, T. Krebs, D. Barcelos, and G. Bramesfeld, "Influence of Propeller Location, Diameter, and Rotation Direction on Aerodynamic Efficiency," *Journal of Aircraft*, vol. 58, no. 1, pp. 63–71, 2021, doi: 10.2514/1.C035917.

[7] H.Gopalan, "Numerical modeling of aerodynamics of airfoils of micro air vehicles in gusty environment," Ph.D. Dissertation, University of Akron, Akron, OH. [Online]. Available: https://www.researchgate.net/publication/253419505_Numerical_modeling_of_aerodynamics_of_airfoils_of_micro_air_vehicles_in_gusty_environment

[8] D. H. Hodges and G. A. Pierce, *Introduction to Structural Dynamics and Aeroelasticity*: Cambridge University Press, 2012.

[9] J. R. Wright and J. E. Cooper, *Introduction to Aircraft Aeroelasticity and Loads*: Wiley, 2014.

[10] T.Theodorsen, "General Theory of Aerodynamic Instability and the Mechanism of Flutter," *Journal of the Aeronautical Sciences*, vol. 2, no. 3, pp. 233–245, 1935. [Online]. Available: https://ntrs.nasa.gov/citations/19930090935

[11] O. D'Ubaldo, C. M. Rizzo, D. Dessi, and F. Passacantilli, "Low mass ratio hydrofoil flutter experimental model design procedure," *MARINE2021*, vol. 1, no. 1, 2022, doi: 10.2218/marine2021.6859.

[12] Robyn L. Harmon, "Aerodynamic modeling of a flapping membrane wing using motion tracking experiments," 2008. [Online]. Available: https://api.semanticscholar.org/CorpusID:107324804

[13] M. R. Amiralaei, H. Alighanbari, and S. M. Hashemi, "An investigation into the effects of unsteady parameters on the aerodynamics of a low Reynolds number pitching airfoil," *Journal of Fluids and Structures*, vol. 26, no. 6, pp. 979–993, 2010, doi: 10.1016/j.jfluidstructs.2010.06.004.

[14] P. Z. Csurcsia, M. F. Siddiqui, M. C. Runacres, and T. de Troyer, "Unsteady Aerodynamic Lift Force on a Pitching Wing: Experimental Measurement and Data Processing," *Vibration*, vol. 6, no. 1, pp. 29–44, 2023, doi: 10.3390/vibration6010003.

[15] M. A. Ashraf, J. Young, and J. C. S. Lai, "Oscillation Frequency and Amplitude Effects on Plunging Airfoil Propulsion and Flow Periodicity," *AIAA Journal*, vol. 50, no. 11, pp. 2308–2324, 2012, doi: 10.2514/1.J051374.

[16] J. Hu, H. Xuan, Y. Yu, and J. Zhang, "Effects of continuously increasing pitching and plunging amplitudes on the aerodynamic forces of flapping airfoils," *AIP Advances*, vol. 9, no. 8, 2019, doi: 10.1063/1.5111808.

[17] MIT: Department of Mechanical Engineering, *2.14 Analysis and Design of Feedback Control Systems: Understanding Poles and Zeros.* [Online]. Available: https://web.mit.edu/2.14/www/Handouts/PoleZero.pdf (accessed: Oct. 24 2022).

[18] [Online]. Available: https://blog.mbedded.ninja/electronics/circuit-design/what-are-transfer-functions-poles-and-zeroes/ (accessed: Aug. 19 2024).

[19] M. Frigo and S. G. Johnson, "FFTW: an adaptive software architecture for the FFT," in *Proceedings of the 1998 IEEE International Conference on Acoustics, Speech and Signal Processing, ICASSP '98 (Cat. No.98CH36181)*, Seattle, WA, USA, 1998, pp. 1381–1384.

[20] H. Wang, W. Gan, and D. Li, "An investigation of the aerodynamic performance for a propeller-aided lift-enhancing double wing configuration," *Aerospace Science and Technology*, vol. 105, p. 105991, 2020, doi: 10.1016/j.ast.2020.105991.

[21] J. D. Anderson, *Introduction to flight,* 7th ed. New York: McGraw-Hill, 2012.

[22] D. P. Raymer, *Aircraft design: A conceptual approach*. Reston: American Institute of Aeronautics and Astronautics, 2021.

[23] *Elements of Propulsion,* 2nd ed. Reston: American Institute of Aeronautics & Astronautics, 2016.

[24] J. Roskam, *Airplane flight dynamics and automatic flight controls. Pt. 2*. Lawrence: DARcorporation, 2009 (1995).

[25] C. Yang, X. Zheng, Q.-W. Ma, and Z.-Y. Yu, Eds., *Fluid-Structure Interaction for Flapping Flexible Plate with Two Plates in a Line*, 2019.

[26] B. Uekermann, "Partitioned Fluid-Structure Interaction on Massively Parallel Systems," 2016.
[27] G. Chourdakis *et al.,* "preCICE Distribution Version v2211.0," 2023.
[28] G. Chourdakis *et al.,* "preCICE v2: A sustainable and user-friendly coupling library," *Open research Europe*, vol. 2, p. 51, 2022, doi: 10.12688/openreseurope.14445.2.
[29] H.-J. Bungartz *et al.,* "preCICE – A fully parallel library for multi-physics surface coupling," *Computers & Fluids*, vol. 141, pp. 250–258, 2016, doi: 10.1016/j.compfluid.2016.04.003.
[30] A. Savino, A. Cocco, A. Zanotti, M. Tugnoli, P. Masarati, and V. Muscarello, "Coupling Mid-Fidelity Aerodynamics and Multibody Dynamics for the Aeroelastic Analysis of Rotary-Wing Vehicles," *Energies*, vol. 14, no. 21, p. 6979, 2021, doi: 10.3390/en14216979.
[31] B. Uekermann, H.-J. Bungartz, L. Cheung Yau, G. Chourdakis, and A. Rusch, "Official preCICE Adapters for Standard Open-Source Solvers," in *Proceedings of the 7th GACM Colloquium on Computational Mechanics for Young Scientists from Academia*, 2017.
[32] B. Schrefler, Ed., *Coupled problems 2015: Proceedings of the VI International Conference on Coupled Problems in Science and Engineering, San Servolo, Venice, Italy, May 18-20 2015,* 1st ed. Barcelona: International Center for Numerical Methods in Engineering (CIMNE), 2015.
[33] M. Tugnoli, D. Montagnani, M. Syal, G. Droandi, and A. Zanotti, "Mid-fidelity approach to aerodynamic simulations of unconventional VTOL aircraft configurations," *Aerospace Science and Technology*, vol. 115, p. 106804, 2021, doi: 10.1016/j.ast.2021.106804.
[34] [Online]. Available: https://pytornado.readthedocs.io/en/latest/theory/coordinate_systems.html (accessed: Aug. 20 2024).
[35] [Online]. Available: https://www.cpacs.de/documentation/CPACS_Exact/html/89b6a288-0944-bd56-a1ef-8d3c8e48ad95.htm (accessed: Aug. 20 2024).
[36] R. Yin, J. Huang, and Z.-Y. He, "Effects of Pitching Motion Elements on Aerodynamic Characteristics of Airfoil," *J. Phys.: Conf. Ser.*, vol. 2076, no. 1, p. 12078, 2021, doi: 10.1088/1742-6596/2076/1/012078.
[37] Y. S. Baik, J. Rausch, L. Bernal, and M. Ol, "Experimental Investigation of Pitching and Plunging Airfoils at Reynolds Number between 1x10^4 and 6x10^4," in *39th AIAA Fluid Dynamics Conference*, San Antonio, Texas, 2009.
[38] M. Goland, "The Flutter of a Uniform Cantilever Wing," *Journal of Applied Mechanics*, vol. 12, no. 4, A197-A208, 1945, doi: 10.1115/1.4009489.

[39] M Sc Thesis and Damla Durmuş, "AEROELASTIC ANALYSIS OF VARIABLE-SPAN MORPHING WINGS," Unpublished, 2020.

[40] I. Bennamia, A. Badereddine, and T. Zebbiche, "Measurement of vibrations of composite wings using high-order finite element beam," *J. meas. eng.*, vol. 6, no. 3, pp. 143–154, 2018, doi: 10.21595/jme.2018.20046.

[41] G. Dimitriadis, G. A. Vio, and D. Shi, "An Expert System for the Identification of Nonlinear Dynamical Systems," in *Lecture Notes in Computer Science, Intelligent Computing*, D. Hutchison et al., Eds., Berlin, Heidelberg: Springer Berlin Heidelberg, 2006, pp. 1263–1268.

[42] P. Aref, M. Ghoreyshi, A. Jirasek, M. Satchell, and K. Bergeron, "Computational Study of Propeller–Wing Aerodynamic Interaction," *Aerospace*, vol. 5, no. 3, p. 79, 2018, doi: 10.3390/aerospace5030079.

Appendix

Appendix A

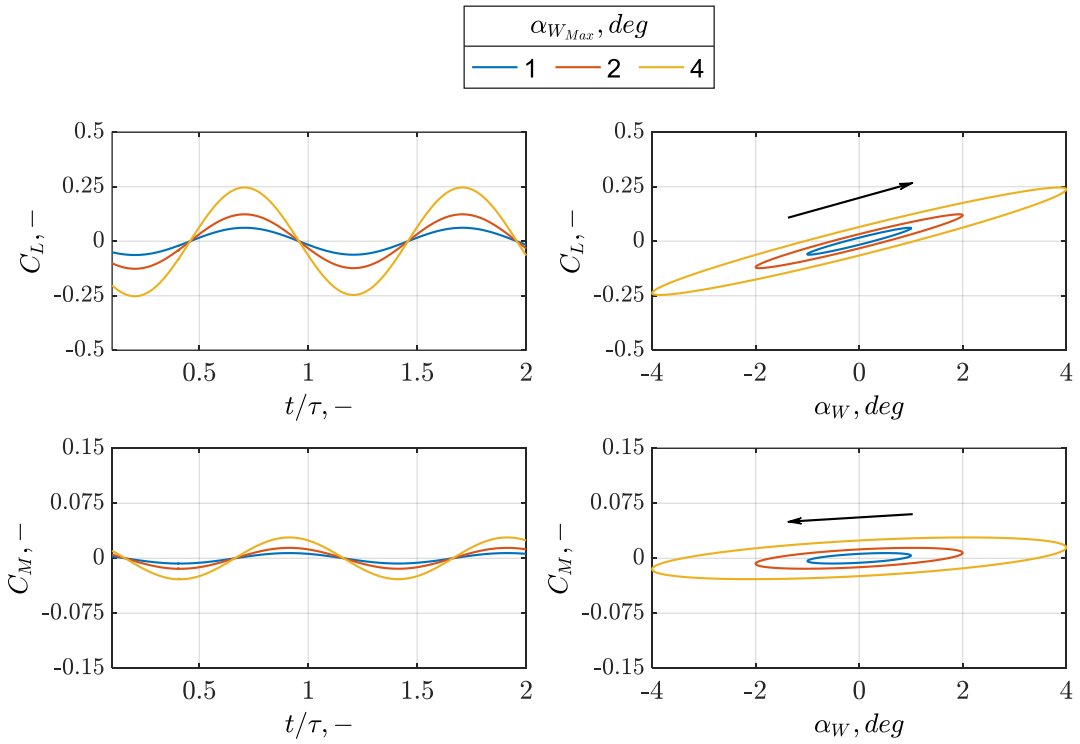

a. ***k* = 0.201**

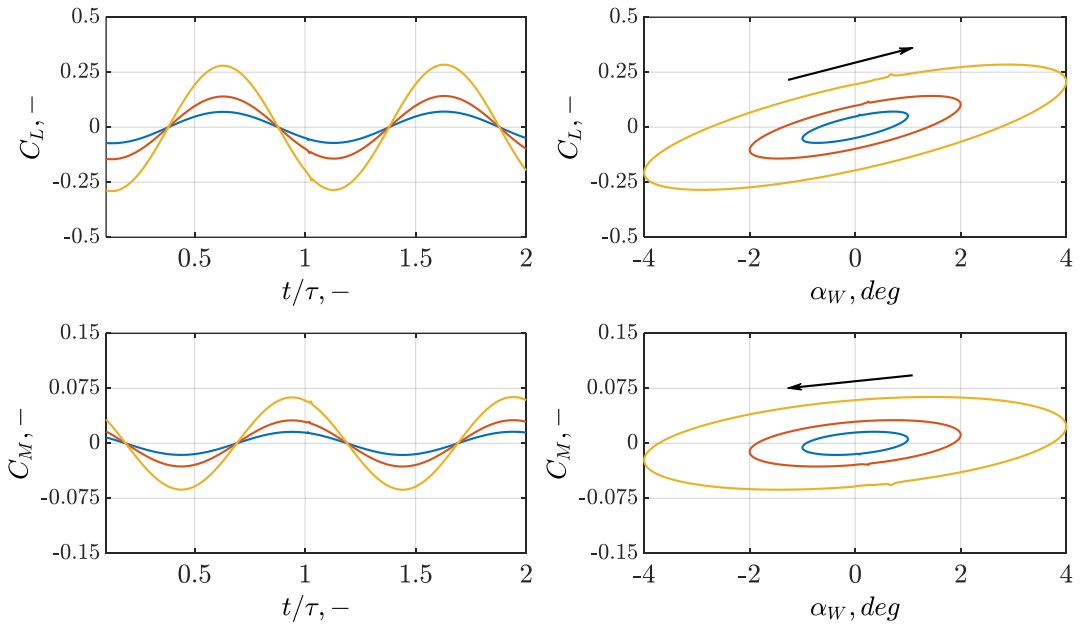

b. ***k* = 0.503**

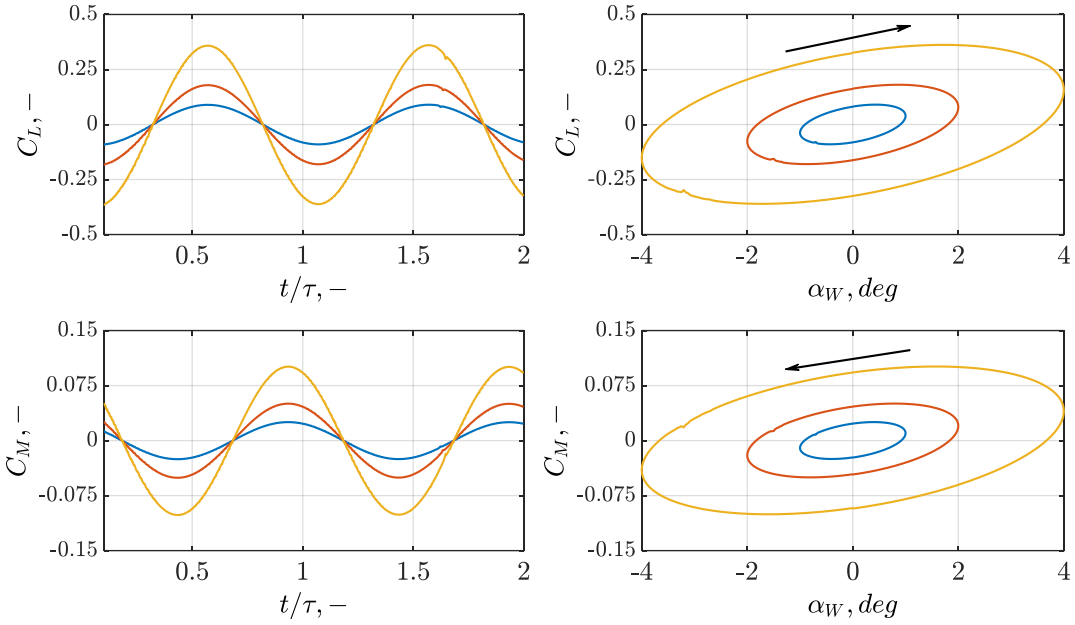

c. k = 0.804

Figure Appendix A-1: *Veldhuis Wing* (Standalone Wing, NACA 64_2-a015, Pitching motion) – α_{WMax} variation

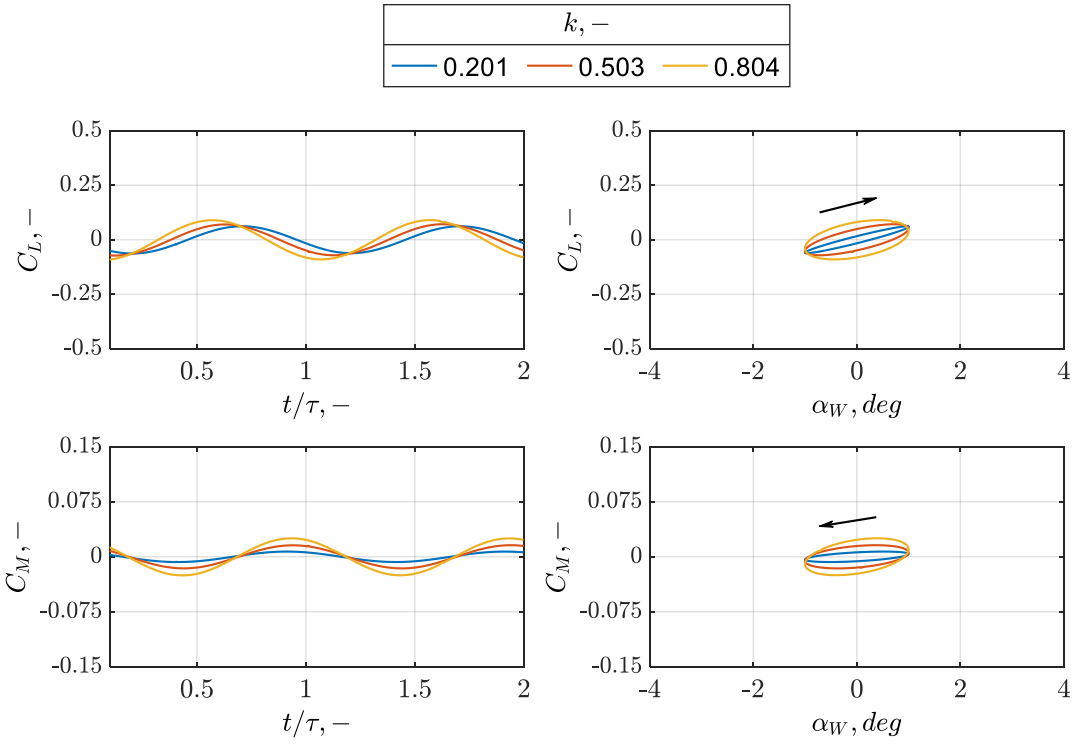

a. α_{WMax} = 1°

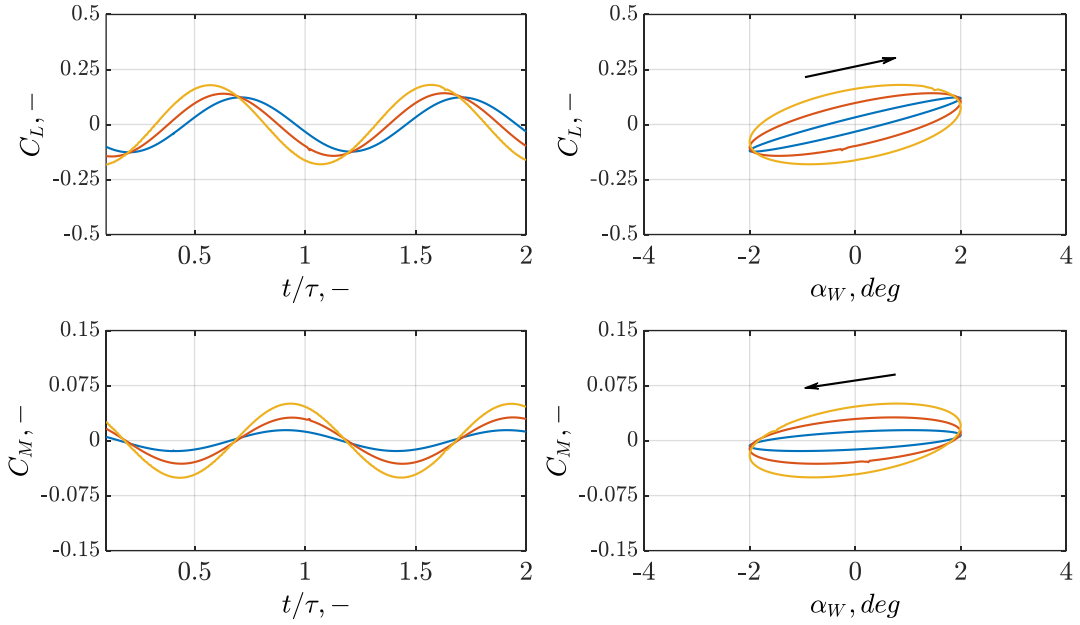

b. α_{WMax} **= 2°**

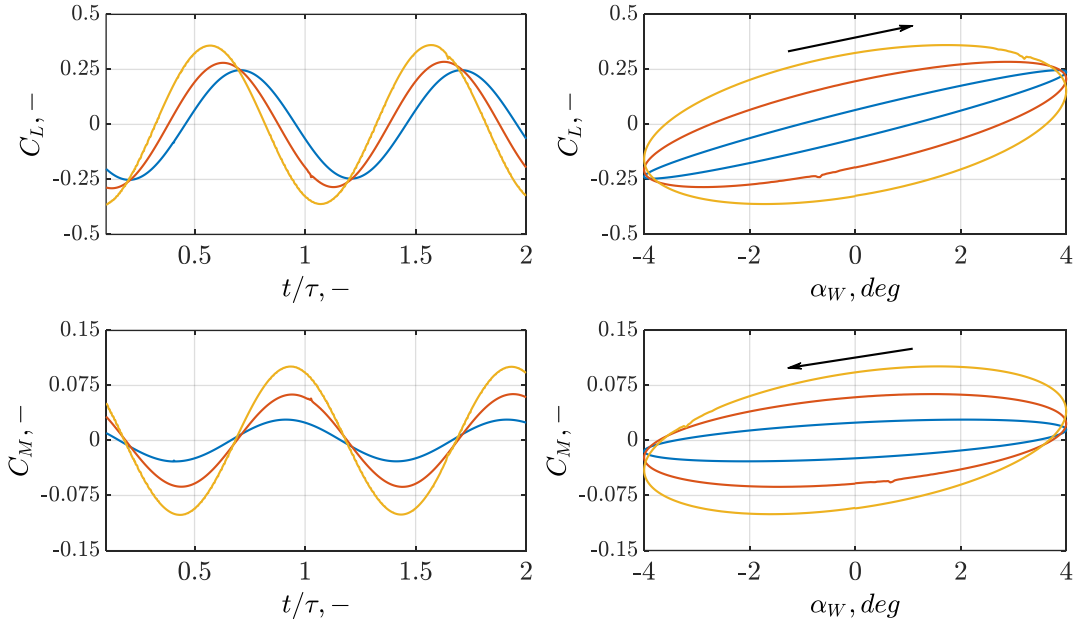

c. α_{WMax} **= 4°**

Figure Appendix A-2: *Veldhuis Wing* (Standalone Wing, NACA 64_2-a015, Pitching motion) – *k* variation

Appendix B

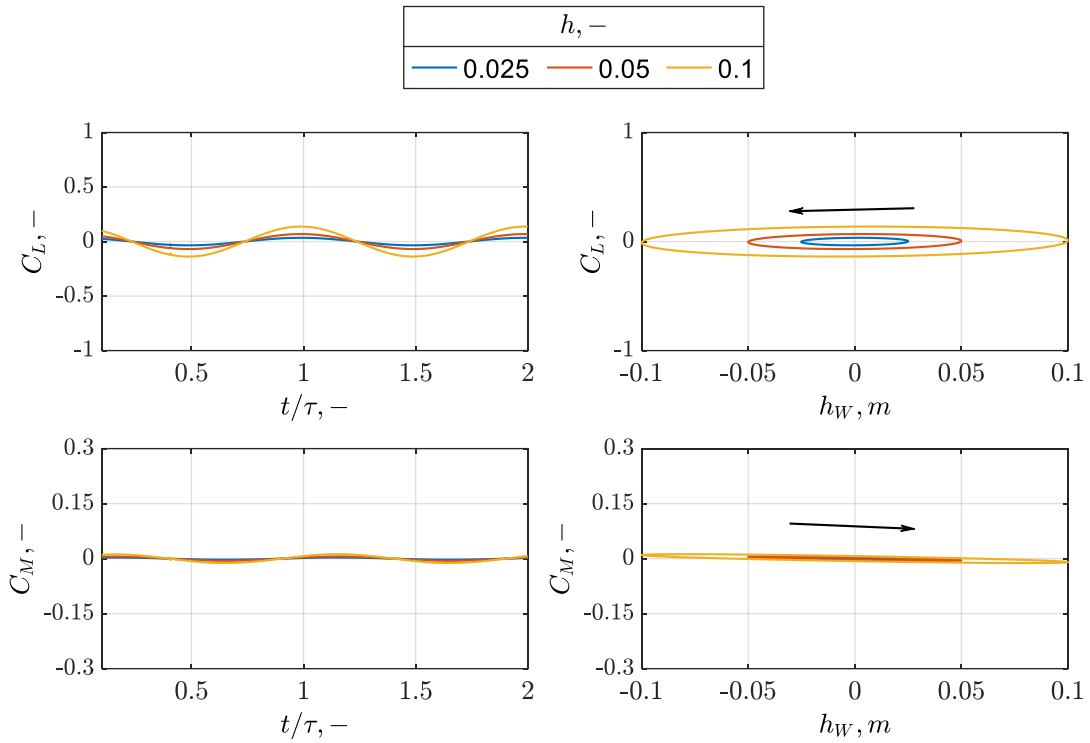

a. *k* = 0.201

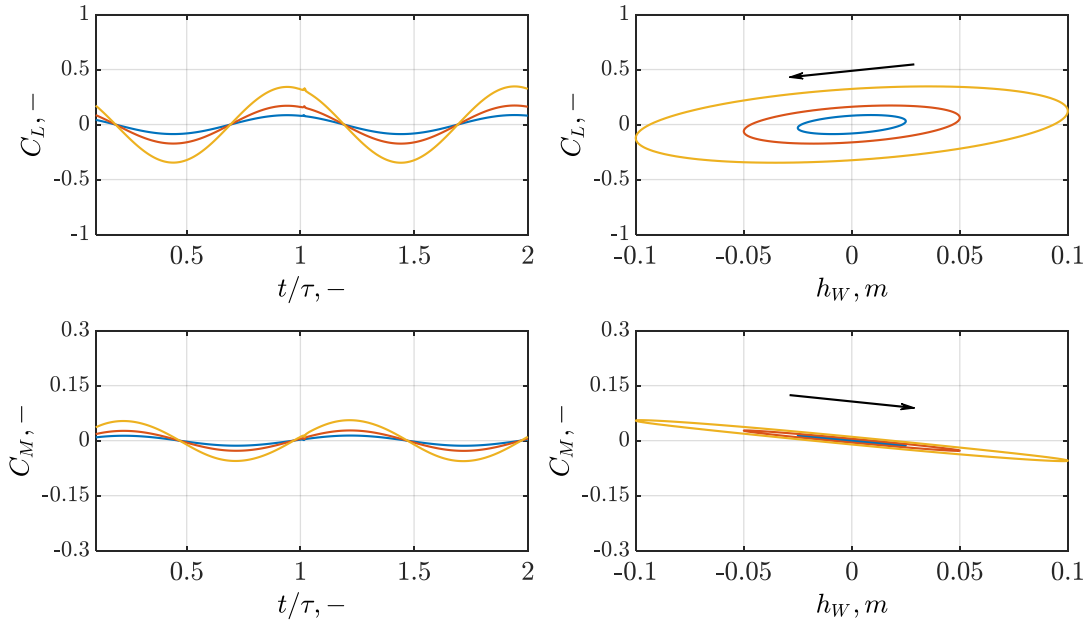

b. *k* = 0.503

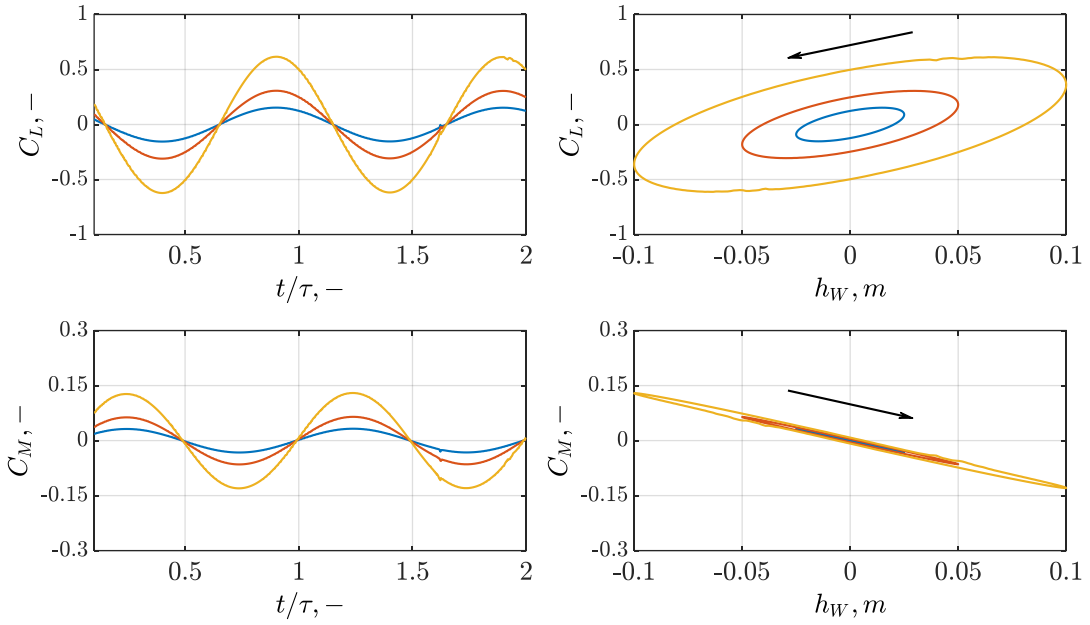

c. *k* = 0.804

Figure Appendix B-1: *Veldhuis Wing* (Standalone Wing, NACA 64_2-a015, Plunging motion) – *h* variation

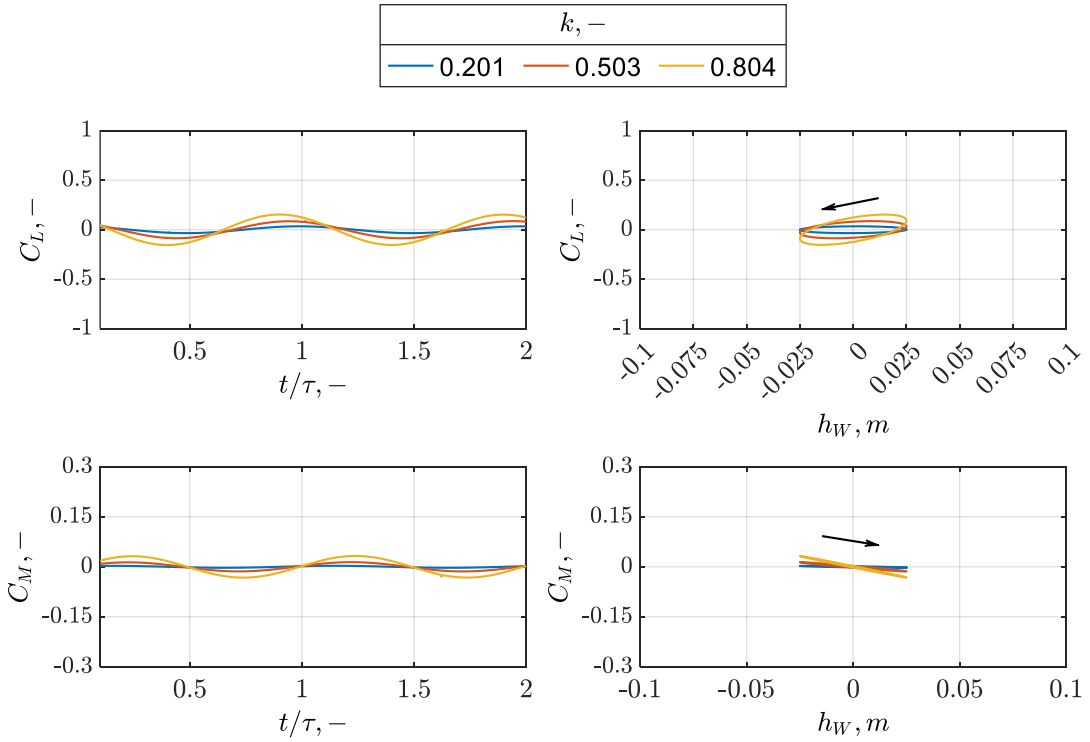

a. *h* = 0.025

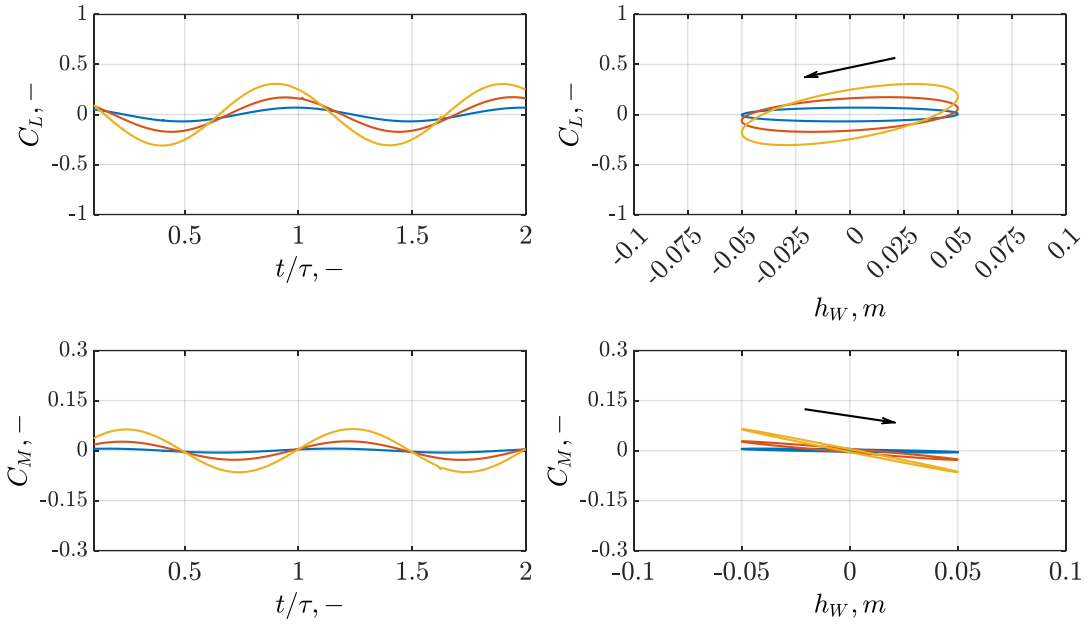

b. *h* = 0.05

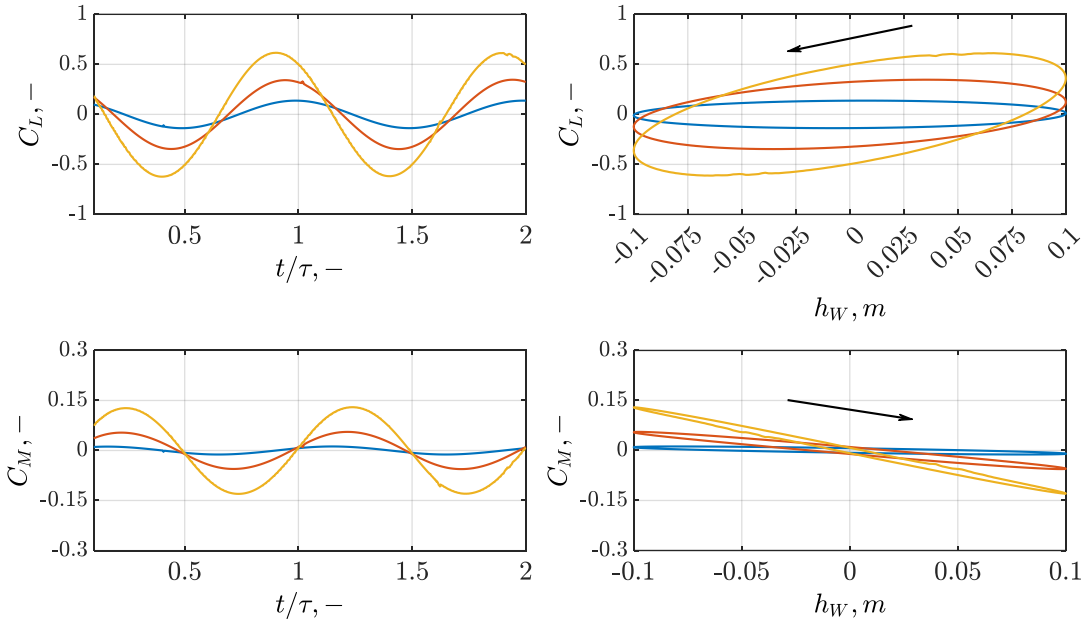

c. *h* = 0.1

Figure Appendix B-2: *Veldhuis Wing* (Standalone Wing, NACA 64_2-a015, Plunging motion) – *k* variation

Appendix C

According to Aref and Ghoreyshi [42], an increase in the propeller blade pitch angle increases the dynamic pressure behind the propeller and therefore increases the wing lift behind it. To validate this, FMI simulations were performed on the *Veldhuis Wing + Propeller 1* model. The model descriptions for *Veldhuis Wing* and *Propeller 1* are provided in Table 5-1 and Table 5-2 respectively. All model parameters and simulation settings were kept fixed (see Table 5-3) except for the blade pitch angle ($\beta_{0.75}$) and wing angle of attack (α_W). The simulation and model parameter descriptions are given in Table Appendix C-1.

Table Appendix C-1: *Veldhuis Wing* (+ *Propeller 1*, NACA 64_2-a015) – Model parameters and simulation settings: Blade pitch angle ($\beta_{0.75}$) variation study

Parameter (Fixed)	Value
Rotation direction	IU
Advance ratio $(J, -)$	0.85
Normalised Y-position $(y_P/b_W/2, -)$	0.469
Propeller relative inclination $(\alpha_{P\to W}, deg)$	0.0
Parameter (Varying)	**Range**
Wing angle of attack (α_W, deg)	0, 2, 4, 6, 8, 10
Blade pitch angle $(\beta_{0.75}, deg)$	20, 25, 30

The spanwise C_L distribution of the wing-propeller model at different wing angles of attack were plotted in Figure Appendix C-1. Each solid line represents the spanwise C_L distribution for a different blade pitch and the purple dashed line represents the spanwise C_L distribution of the standalone wing. The red and green dashed lines represent the blade tip and blade centre spanwise locations, respectively.

It was observed that the spanwise C_L distribution varied when a propeller was added to the wing. The wing region where the blades move upward (0.182m – 0.3m) saw an increase in local angle of attack which caused a local increase in C_L whereas the wing region where the blades move downward (0.3m – 0.418m) saw a decrease in local angle of attack and hence a local decrease in C_L.

Additionally, the magnitude of local C_L increase was seen to vary with a change in the blade pitch angle, i.e. larger the blade pitch angle, greater the increase in local C_L. This was attributed to a larger contraction of the propeller slipstream and hence a larger increase in dynamic pressure in the propeller wake and an increase in propeller swirl. The increase in propeller swirl and larger spanwise C_L gradient increased the crossflow above and below the wing. This amplified the C_L in the neighboring regions, i.e. the regions near the wing tip and wing root which could be observed at all α_W.

At $\alpha_W = 0°$, the increases in dynamic pressure above and below the wing were found to be unequal. While the wing comprised of a symmetric airfoil and the propeller was in line with the wing mean chord line, the asymmetrical spanwise location of the propeller caused an asymmetrical spanwise lift distribution. The magnitude of local $C_{L_{Min}}$ was observed to be slightly higher than the magnitude of local $C_{L_{Max}}$. Apparently, the C_L gradient was higher in the region near the wing tip due to the asymmetrical spanwise location of the propeller with respect to the wing ($y_P/b_W/2$ is 0.469 and not 0.5). The region between the maximum dynamic pressure region at the downgoing blade side (DBS) and the wing tip ($0.625 \leq y_P/b_W/2 \leq 1.0$) was longer compared to the shorter region between the maximum dynamic pressure region at the upgoing blade side (UBS) of the propeller centre and the wing root ($0.0 \leq y_P/b_W/2 \leq 0.281$). This longer region unaffected by the propeller slipstream observed a larger C_L gradient hence increased the crossflow which in turn amplified the local C_L in the DBS region.

As α_W was increased, an increase in C_L could be observed across the wing. This increase in C_L due to increase in α_W in addition to the local C_L change due to the propeller made the spanwise C_L distribution no longer symmetric about the propeller centre location. Additionally, the change in C_L in the DBS region was observed to decrease for an increase in α_W. For much higher wing angles of attack ($\alpha_W \geq 6°$), the C_L distribution for the wing-propeller model was greater than the standalone wing across the entire wingspan, the reason for this being that the increase in C_L due to increase in α_W far exceeded the decrease in local C_L due to the downgoing blade, hence the overall change in C_L in the DBS region was positive.

The asymmetrical spanwise C_L distribution for $\alpha_W > 0°$ was due to the propeller no longer being in line with the wing mean chord line. For $\alpha_W > 0°$ (and propellers in a tractor configuration), the propeller centre is located above the wing mean chord line and hence the dynamic pressure above the wing is much higher than the dynamic pressure below the wing. The increase in dynamic pressure above the wing increases the local C_L behind the propeller. This augments the C_L increase on the UBS side and attenuates the C_L on the DBS side. The higher the α_W, larger the augmentation and attenuation of C_L behind the wing.

The results obtained agree with the results obtained by Veldhuis [4] and by Aref and Ghoreyshi [42].

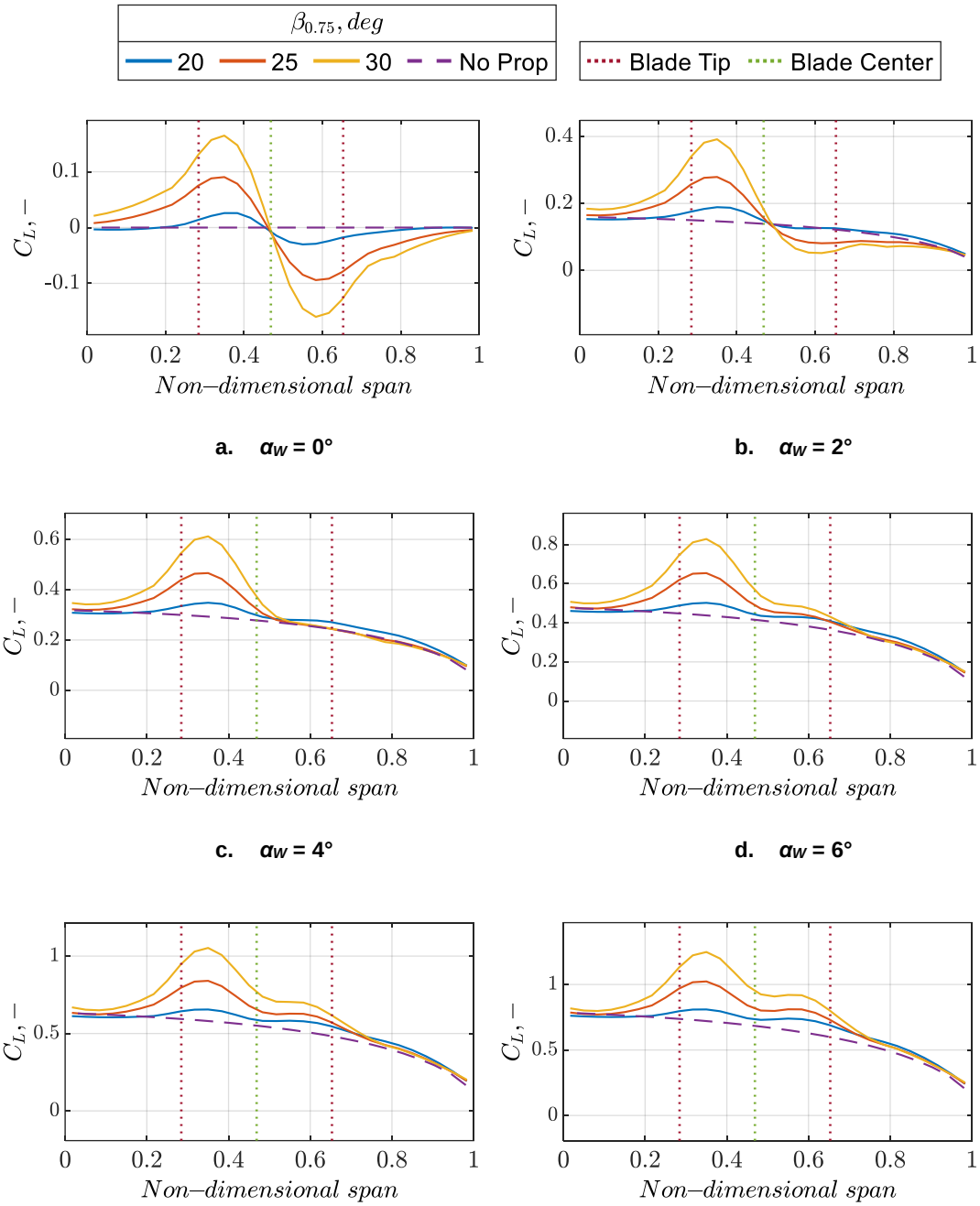

a. $\alpha_W = 0°$ **b.** $\alpha_W = 2°$

c. $\alpha_W = 4°$ **d.** $\alpha_W = 6°$

e. $\alpha_W = 8°$ **f.** $\alpha_W = 10°$

Figure Appendix C-1: *Veldhuis Wing* (+ *Propeller 1*, NACA 64_2-a015) – Spanwise C_L distribution: $\beta_{0.75}$ comparison

Appendix D

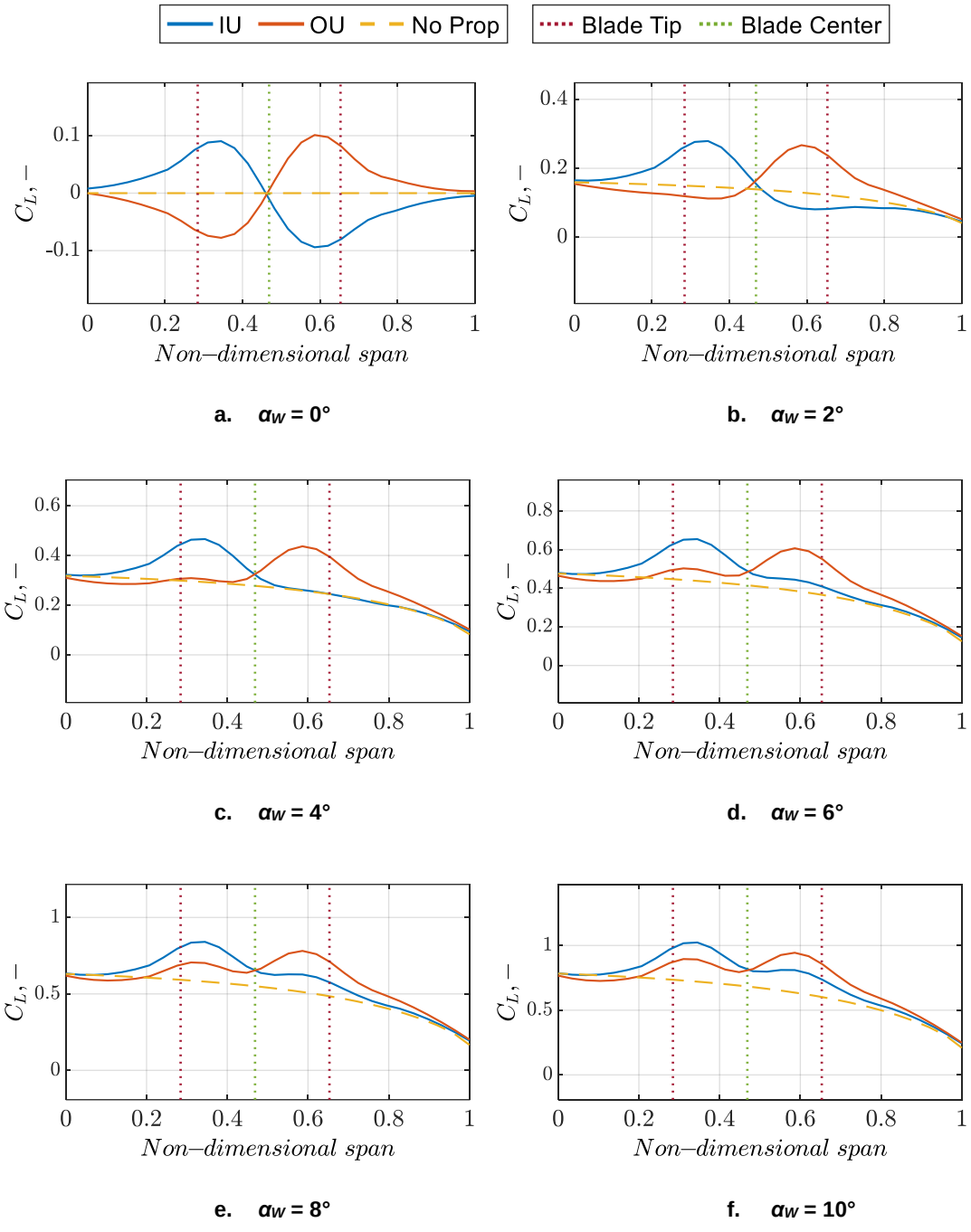

a. α_W = 0°

b. α_W = 2°

c. α_W = 4°

d. α_W = 6°

e. α_W = 8°

f. α_W = 10°

Figure Appendix D-1: *Veldhuis Wing* (+ *Propeller 1*, NACA 64_2-a015) – Spanwise C_L distribution: Rotation direction comparison

Appendix E

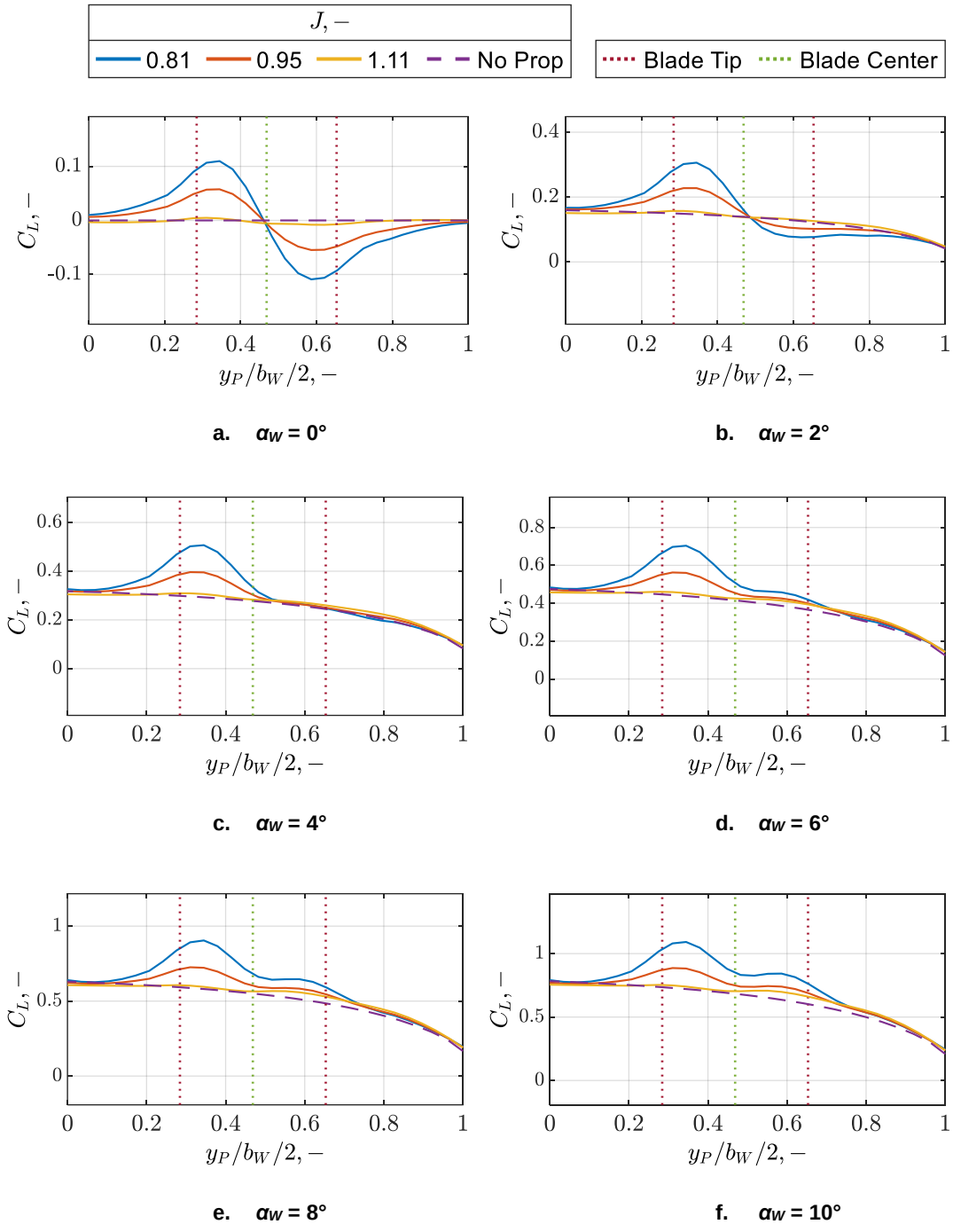

a. α_W **= 0°** **b.** α_W **= 2°**

c. α_W **= 4°** **d.** α_W **= 6°**

e. α_W **= 8°** **f.** α_W **= 10°**

Figure Appendix E-1: *Veldhuis Wing* (+ *Propeller 1*, NACA 64_2-a015) – Spanwise C_L distribution: *J* comparison